DDC
RECEIVED
DEC 19 1977
RECEIVED
D

NORTHROP
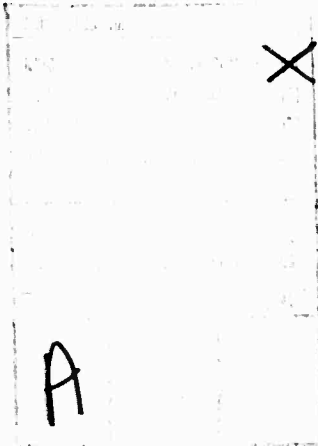
Research and Technology Center

High Power Short Wavelength

Laser Development

November 1977

D. B. Cohn and W. B. Lacina

Contract N00014-76-C-1100

Sponsored By

ADVANCED RESEARCH PROJECTS AGENCY

ARPA Order No. 3125

Monitored By

OFFICE OF NAVAL RESEARCH

NORTHROP CORPORATION
Northrop Research and Technology Center
3401 West Broadway
Hawthorne, California 90250
Telephone: (213) 970-5163

REPORT DOCUMENTATION PAGE

READ INSTRUCTIONS BEFORE COMPLETING FORM

1. REPORT NUMBER	2. GOVT ACCESSION NO.	3. RECIPIENT'S CATALOG NUMBER
NRTC-77-43R		

4. TITLE (and Subtitle)

HIGH POWER SHORT WAVELENGTH LASER DEVELOPMENT.

5. TYPE OF REPORT & PERIOD COVERED

Final Technical Report.
1 July 76 — 30 Sept 77.

6. PERFORMING ORG. REPORT NUMBER

NRTC-77-43R

7. AUTHOR(s)

D. B. Cohn W. B. Lacina

8. CONTRACT OR GRANT NUMBER(s)

N00014-76-C-1190,

9. PERFORMING ORGANIZATION NAME AND ADDRESS

Northrop Research and Technology Center
3401 West Broadway
Hawthorne, CA 90250

10. PROGRAM ELEMENT, PROJECT, TASK AREA & WORK UNIT NUMBERS

ARPA Order 3125

11. CONTROLLING OFFICE NAME AND ADDRESS

Advanced Research Projects Agency
1400 Wilson Blvd.
Arlington, Virginia 22209

12. REPORT DATE

Nov 77

13. NUMBER OF PAGES

173 p.

14. MONITORING AGENCY NAME & ADDRESS(if different from Controlling Office)

Office of Naval Research
Department of the Navy
Arlington, Virginia 22217

15. SECURITY CLASS. (of this report)

Unclassified

15a. DECLASSIFICATION DOWNGRADING SCHEDULE

16. DISTRIBUTION STATEMENT (of this Report)

Distribution of this document is unlimited

17. DISTRIBUTION STATEMENT (of the abstract entered in Block 20, if different from Report)

- - - - - - -

18. SUPPLEMENTARY NOTES

- - - - - - -

19. KEY WORDS (Continue on reverse side if necessary and identify by block number)

Excimer Laser, KrF Laser, Electrical Excitation, High Power

approx. 1 microsec.

20. ABSTRACT (Continue on reverse side if necessary and identify by block number)

Results of a comprehensive experimental and theoretical investigation of a large volume, electron beam and discharge excited KrF laser are reported. For pulse lengths $\simeq 1 \mu s$, maximum specific energy extraction was 22 J/liter at 10% efficiency and maximum total energy was 90J for a 10 liter gain volume. Discharge enhancement of output energy was limited by discharge instability as a result of beam deposition nonuniformity. Excellent agreement in terms of absolute values and waveforms was obtained with an extensive computer code.

DD FORM 1473 1 JAN 73 EDITION OF 1 NOV 65 IS OBSOLETE

UNCLASSIFIED

i

SECURITY CLASSIFICATION OF THIS PAGE (When Data Entered)

407696

HIGH POWER SHORT WAVELENGTH LASER DEVELOPMENT

ARPA Order Number:	3125
Program Code Number:	TE20
Contract Number:	N00014-76-C-1100
Principal Investigators and Telephone Number:	Dr. D. B. Cohn (213) 970-5163 Dr. W. B. Lacina (213) 970-4881
Program Manager:	Dr. G. Hasserjian (213) 970-4861
Name of Contractor:	Northrop Corporation Northrop Research and Technology Center 3401 W. Broadway Hawthorne, CA 90250
Scientific Officer:	Physical Sciences Division Physics Program Office of Naval Research 800 N. Quincy Street Arlington, VA 22217
Effective Date of Contract:	01 July 76-30 September 77
Amount of Contract:	$1,165,310.00
Sponsored By:	Advanced Research Projects Agency ARPA Order 3125

TABLE OF CONTENTS

1. INTRODUCTION & SUMMARY

The possibility of attaining high optical extraction efficiencies from lasers operating on the bound-free transitions of rare gas halide excimers formed in high pressure electrically excited mixtures is currently attracting much interest[1]-[22]. So far, the most successful exploitation of this scheme has been the development of the KrF laser[5]-[22], and extensive literature[20]-[29] on the kinetic processes and their rate constants is presently available. The present program has been directed toward experimental and theoretical investigation of the fundamental physical mechanisms of the KrF laser, with the objective of demonstrating high volumetric extraction (~ 50 J/liter) at high efficiency ($\sim 10\%$).

In order to demonstrate the potential of excimer laser systems for high optical extraction at high efficiencies, a large volume laser device was constructed. The operating characteristics of this device, which shall be described in detail in Section 2, were chosen in such a way as to provide maximum flexibility for investigating, in addition to the Kr F system, other promising molecules. It is shown how the basic geometry developed from various constraints imposed by the requirements of electron beam and discharge excitation of the low impedance medium. Under nominal conditions, the electron gun operated at a beam voltage of 320 KeV for current densities of 10-20 A/cm^2 and 1000-2000 cm^2 apertures. Pulse lengths, typically one microsecond, required the development of discharge circuits capable of driving significant energy through the inherent circuit inductance over these times. In this regard, both fast capacitive discharge and pulse charged discharges, designed to circumvent a portion of the circuit inductance, were developed. The resulting circuitry was highly successful providing for a repeatable and reliable source at full rated energy and charge voltages.

---

[1]-[30] These references appear at the end of Section 1. (pages 2-4).

In order to optimize the performance of the KrF laser and to understand its scaling to high power and high volume, it is necessary to understand the kinetic and pumping processes which are responsible for the formation and quenching of the excited species. In Section 3, the details of a comprehensive theoretical model[17]-[19], [30] will be described. This model, which consists of an extensive computer analysis of the coupled set of equations for molecular kinetics, electron kinetics, radiative extraction, and external driving circuit, was constructed from a more general computer code which automatically synthesizes the complete coupled analysis by translating symbolic reactions into computer-coded equations. The general synthesis code, which is applicable to a broad class of electrically excited laser systems, makes it possible to obtain a complete coupled analysis of the most complicated kinetic scheme containing an arbitrary number of reactions and interacting species with virtually no effort. The code synthesized for analysis of the KrF system, which involved a reaction scheme of ~ 80 kinetic processes has been successful in experimental comparisons over a wide range of operating parameters for the scale-up and other experimental devices. Under optimum conditions, the code predicts a specific optical output of ~ 25 J/liter with a $\sim 6.5\%$ extraction efficiency.

Section 4 contains the experimental results and a comparison with the theoretical analysis for a typical set of conditions. Due to nonuniform electron beam energy deposition in the direction of propagation, both total extracted energy and discharge enhancement were severely limited. As a result, experiments were conducted with 3 and 10 liter extraction volumes in order to optimize specific energy extraction and total output energy, respectively. Under optimum conditions, total energy output was 90 J for a 10 liter volume, and for the 3 liter volume, specific extraction was 22 J/liter for beam current densities on the order of 20 A/cm^2. Efficiency in both cases was about 10%.

---

[1] S. K. Searles and G. A. Hart, Appl. Phys. Lett. 27, 243 (1975); Appl. Phys. Lett. 25, 79 (1974).

(2) S. K. Searles, Appl. Phys. Lett. 25, 735 (1974).

(3) J. E. Velazco and D. W. Setzer, J. Chem. Phys. 62, 1990 (1975).

(4) E. R. Ault, R. S. Bradford, Jr., and M. L. Bhaumik, Appl. Phys. Lett. 27, 413 (1975).

(5) C. A. Brau and J. J. Ewing, Appl. Phys. Lett. 27, 435 (1975).

(6) J. A. Mangano, J. H. Jacob, and J. B. Dodge, Appl. Phys. Lett. 29, 426 (1976).

(7) M. Rokni, J. H. Jacob, J. A. Mangano, and R. Brochu, Appl. Phys. Lett. 30, 458 (1977).

(8) J. G. Eden and S. K. Searles, Appl. Phys. Lett. 29, 356 (1976).

(9) J. J. Ewing and C. A. Brau, Appl. Phys. Lett. 27, 350 (1975).

(10) R. Burnham, F. X. Powell, and N. Djeu, Appl. Phys. Lett. 29, 30 (1976).

(11) C. P. Wang. Appl. Phys. Lett. 29, 103 (1976).

(12) J. A. Mangano and J. H. Jacob, Appl. Phys. Lett. 27, 495 (1975).

(13) M. L. Bhaumik, R. S. Bradford, and E. R. Ault, Appl. Phys. Lett. 28, 23 (1976).

(14) J. H. Jacob and J. A. Mangano, Appl. Phys. Lett. 28, 724 (1976).

(15) J. D. Daugherty, J. A. Mangano, and J. H. Jacob, Appl. Phys. Lett. 28, 581 (1976).

(16) W. B. Lacina, R. S. Bradford, Jr., E. R. Ault, and M. L. Bhaumik, "Kinetic Studies of the Krypton Fluoride Laser", presented at Ninth International Quant. Elect. Conf., Amsterdam, Netherlands, June 1976.

(17) W. B. Lacina and R. S. Bradford, Jr., "Kinetic Modeling of Electrical Lasers: Results for KrF", presented at Twenty Ninth Gaseous Elect. Conf., Cleveland, Ohio, October 1976.

(18) W. B. Lacina, R. S. Bradford, Jr., D. B. Cohn, J. B. West, D. Richman, W. H. Long, and M. L. Bhaumik, "High Power Rare Gas Halide Laser Investigations", presented at Seventh Winter Colloquium on High Power Visible Lasers, Park City, Utah, February 1977.

3

(19) W. B. Lacina, R. S. Bradford, Jr., and M. L. Bhaumik, "Kinetic Studies of the KrF Laser", Northrop Rept. NRTC-77-29R, March 1977.

(20) W. B. Lacina and D. B. Cohn, to be published Appl. Phys. Lett., January 1978.

(21) H. H. Nakano, R. M. Hill, D. C. Lorents, D. L. Heustis, and M. V. McCusker, "New Electronic-Transition Laser Systems", SRI Report No. MP 76-99, December 1976.

(22) J. A. Mangano, J. H. Jacob, M. Rokni, and A. Hawryluk, Appl. Phys. Lett. 31, 26 (1977); M. Rokni, J. H. Jacob, J. A. Mangano, and R. Brochu, Appl. Phys. Lett. 31, 79 (1977).

(23) J. E. Velazco, J. Kolts, and D. W. Setser, J. Chem. Phys. 65, 3469 (1976).

(24) D. K. Bohme, N. G. Adams, M. Mosesman, D. B. Dunkin, and E. E. Ferguson, J. Chem. Phys. 52, 5094 (1970).

(25) F. J. Mehr and M. A. Biondi, Phys. Rev. 176, 322 (1976).

(26) A. Mandl, Phys. Rev. A3, 251 (1971).

(27) L. J. Kieffer, JILA Info. Center Rept. 13, September 1973.

(28) M. Schaper and H. Scheibner, Beitr. Aus der Plasma Phys. 9, 45 (1969).

(29) M. J. Berger and S. M. Seltzer, Studies in Penetration of Charged Particles in Matter, Nat'l Acad. Sci. Publ. No. 1133, Chapter 10 (1967). Due to multiple scattering effects, energy deposition in a high pressure gas is usually somewhat larger, and the effective excitation cross sections used in the analysis are taken to be a factor of 2.0 times the Berger and Seltzer values.

(30) The computer code was developed under an NRTC, IR&D program and was supported in part by the Advanced Research Projects Agency of the Department of Defense and monitored by the Office of Naval Research under contract N00014-76-C-1100.

2. DEVICE CHARACTERISTI S

Electron beam and discharge excitation of large volume, gaseous laser media can be accomplished only through a limited set of geometries. In the present case of high pressure, rare gas-halogen mixtures, it is advantageous to have the electron beam colinear with the discharge current in order to increase the beam range which would otherwise be severely limited. The additional requirement of a moderately long gain medium dictates that the optical axis be aligned at right angles to the electron beam direction. These constraints have led in the present instance to a device which utilizes a large aperture, 20 x 100 cm^2, e^--beam propagating across about 10 cm of gas to a discharge anode of similar cross sectional area. Various other system design parameters were chosen to accomodate the use of high pressure and corrosive gases and the need for a low inductance discharge circuit.

The total laser system is shown in a conceptual rendering in Figure 1. The high pressure laser plenum is in the form of a half-cylinder situated between two box like structures. The structure to the left of the plenum houses the electron beam power supply with a 50 kJ storage capacity, capable of sustaining 360 kV beams at current densities of 20 A/cm^2 over a 1000 cm^2 aperture for 0.5 μs. The structure to the right contains the discharge power supply capable of 100 kV pulses for 1 μs into the 0.25 ohm plasma discharge. Other peripheral equipment includes a gas handling system, seen at the lower edge of the drawing, and a shielded electronics diagnostics room at the upper edge. These components are described in detail in the following paragraphs.

2.1 <u>Electron Gun</u>. In order to generate the large area, relatively high electron beam current densities required of the KrF system, the cold-cathode, field emission technology was adopted. Such devices make use of the electrons produced in dense plasmas formed around sharp cathode edges under the action of intense electric fields. The electrons, accelerated in the generating

5
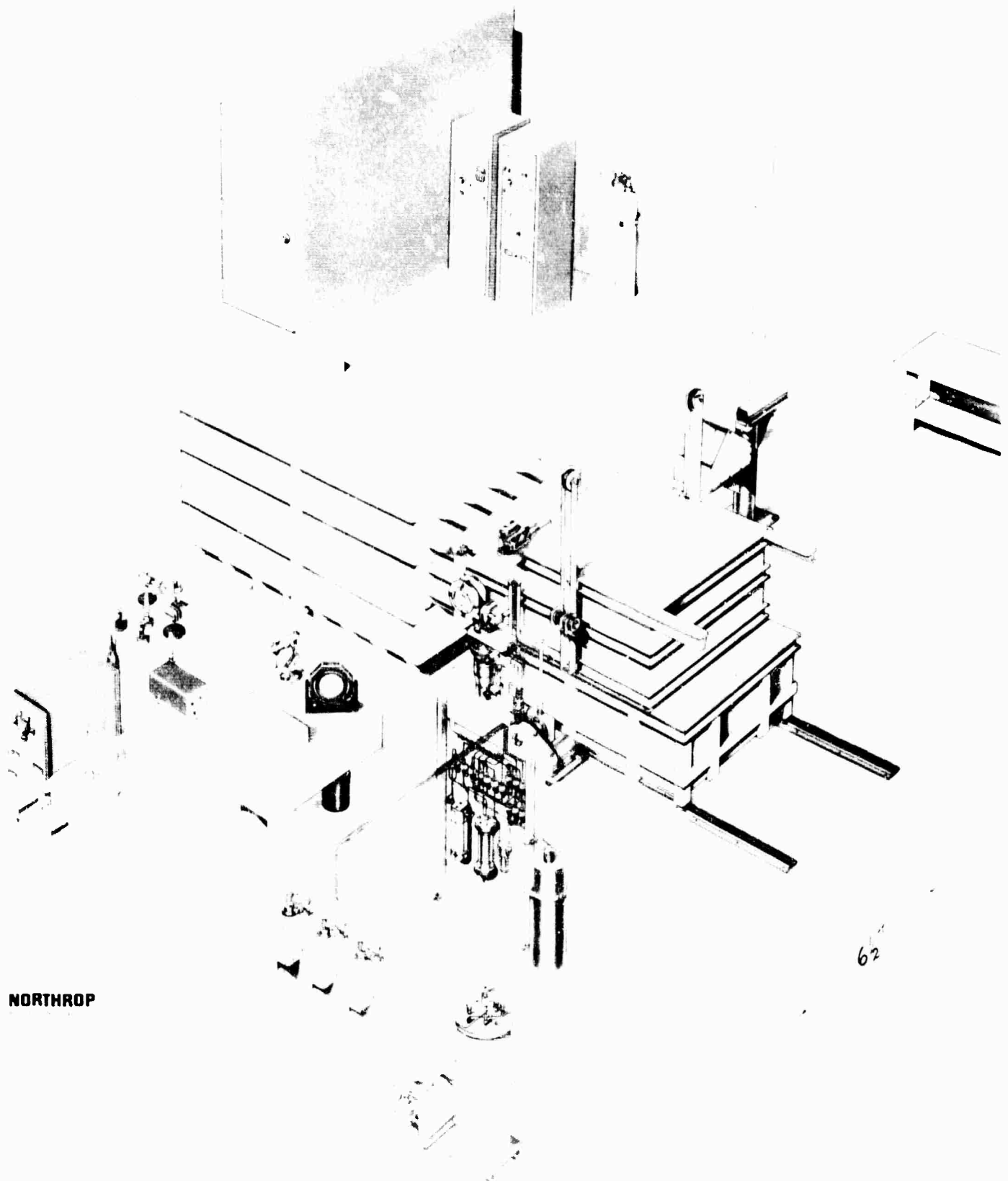
NORTHROP

62

Figure 1 - Experimental Arrangement

electric field, pass through a thin metal foil which serves as the anode plane. The parent plasma, expanding from its place of origin at the cathode, approaches the anode at velocities on the order of 5×10^6 cm/sec and upon contact terminates the pulse. Since the background pressure is on the order of 10^{-6} mm Hg, the residual gas plays no role in these processes. It has been shown that the diode behavior is space charge limited and therefore follows the Child-Langmuir law[31],

$$ J \sim \frac{V^{3/2}}{d^2(t)} $$

where J is current density, V is electrode voltage and d is the anode-cathode separation. The major tradeoff in cold cathode devices is therefore between current density and pulse duration. For the present device the parametric range for beam voltages up to 360 kV is

$$ J = 22 \ A/cm^2, \ 400 \ ns \ pulse \ length $$
$$ 12 \ A/cm^2, \ 800 \ ns \ pulse \ length $$
$$ 8 \ A/cm^2, \ 1.2 \ \mu s \ pulse \ length $$

The desired beam area was $20 \times 100 \ cm^2$, however, depending upon current density, magnetic pinching effects in the diode vacuum section greatly limited the attainable emission area. A 3-stage Marx generator was used for high voltage, high current power generation since flexibility was required in the choice of operating parameters. It was further required that the current rise time be on the order of 100 nsec and this was achieved with a capacitive peaking circuit in parallel with the Marx generator output.

The electron gun is therefore composed of three basic elements: (1) the high voltage power supply in the form of a dc charged, three stage Marx bank;

---

[31] R. H. Huddlestone and S. L. Leonard, "Plasma Diagnostic Techniques", Academic Press, 1965, page 119.

(2) the emitting cathode and its associated corona ring and; (3) the high pressure foil support. These items are indicated pictorially in Figure 2 and will be discussed below in detail followed by a presentation of typical performance characteristics[32].

Electrical Design. The electrical system consisted basically of the Marx bank and its attendant high voltage trigger generators and crowbar switch; the output peaking capacitors and series peaking switch; and the delay trigger generators and control circuitry located in a console external to the device. All of the high voltage components were immersed in insulating oil within a completely sealed metal enclosure to prevent excessive rf radiation. Energy was coupled from the Marx power supply to the gun cathode through three feedthroughs in order to minimize nonuniformities in the current supplied to the cathode surface. Of critical importance was the design of the current feedthroughs in vacuum, since high voltage breakdown was a major concern at the intended gun voltages. As a result, a comprehensive analysis of the geometry dependent electrical characteristics was undertaken[32]. Other elements of the electrical design were not as sens ve since insulating oil and simply excessive stand-off distance could be relied upon. Metallic walls surrounding the cathode corona ring, for example, were maintained at a distance at least twice that from the ring to the foil ground plane, and this arrangement was highly satisfactory.

The crucial elements of the feedthrough design are shown in Figure 3 where the contours indicate equipotential points obtained from a computer calculation of Laplace's equation. The areas of greatest concern are along the insulator surface and at the insul or-conductor-vacuum triple point. Calculation of the electric field along the insulator indicates a maximum field

_____

[32] The electron gun was provided by Systems, Science and Software of Hayward, California who performed the critical design study as well.
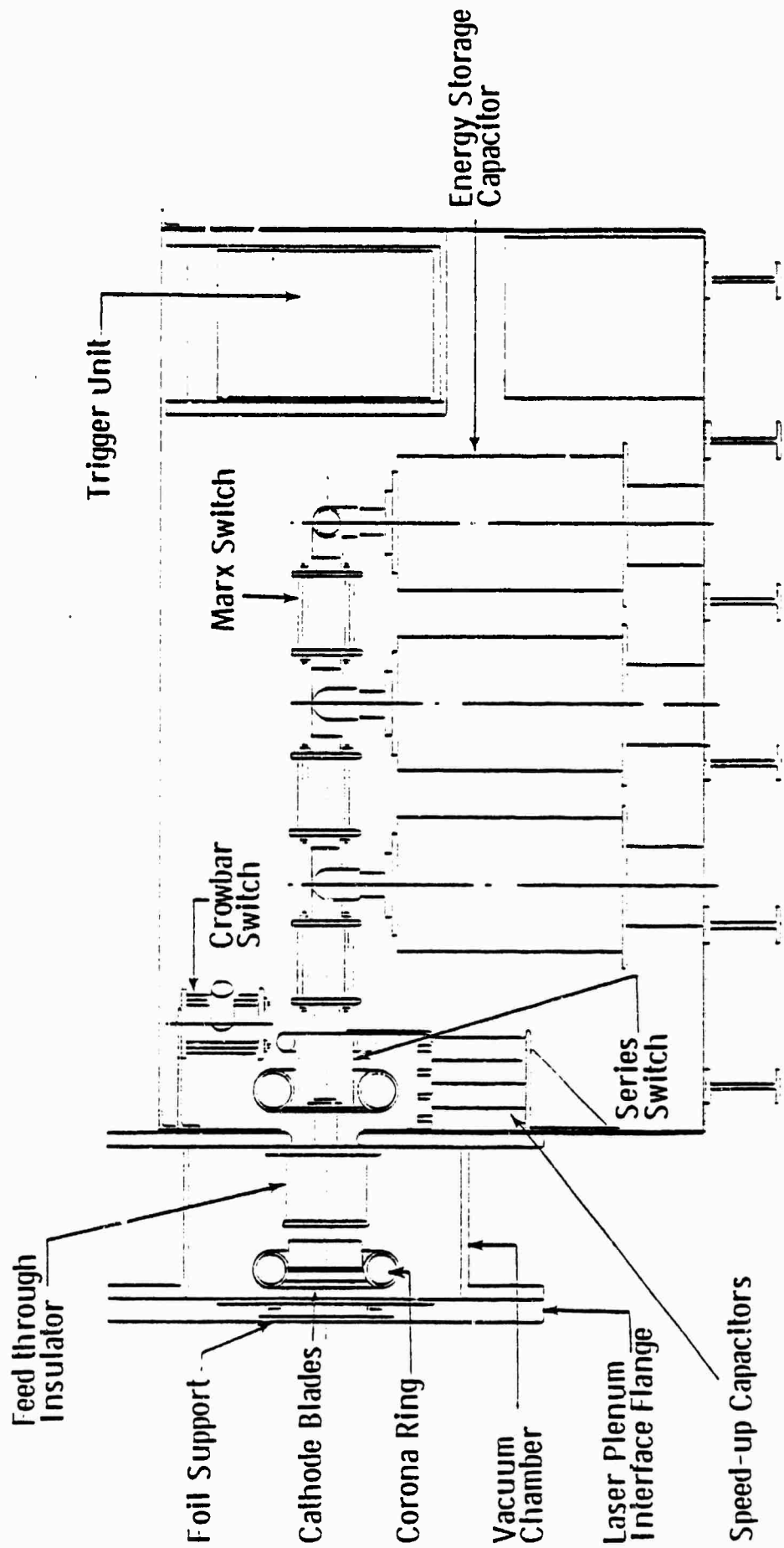
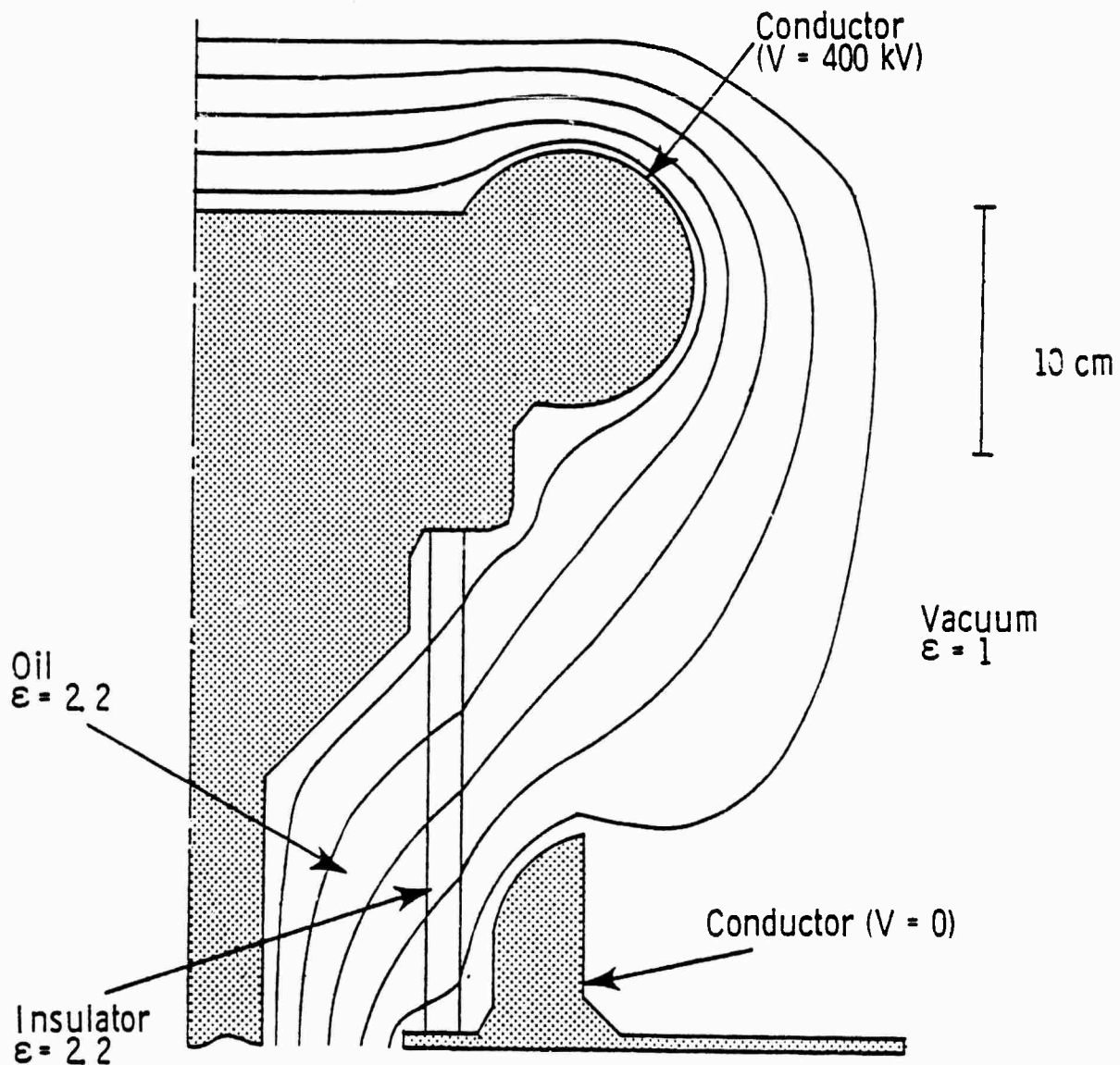Figure 2. Electron Gun Pictorial Schematic

Figure 3. Feedthrough Equipotential Profiles

Conductor
(V = 400 kV)

10 cm

Vacuum
ε = 1

Oil
ε = 2.2

Conductor (V = 0)

Insulator
ε = 2.2

10

intensity of 57 kV/cm for 400 kV applied to the cathode, and since the predicted breakdown field intensity is 196 kV/cm, a safety factor of 3.4 is realised. The triple point field is also comfortably low based on design experience.

The gun circuit elements were specified after analysis of the equivalent circuit shown in Figure 4. The Marx circuit inductance was estimated at about $1.0\,\mu H$, therefore it was expected that the beam voltage risetime would exceed the 100 ns limitation, and indeed this was the case. In order to achieve a shorter risetime, the peaking capacitor, C_2, and series switch, S_2, were added. In this latter case, switch S_2 was set to actuate after C_2 reached the desired peak voltage. The circuit was analyzed for various values of C_2 and an initial charge voltage of 400 kV. A current density of 10 A/cm^2 (20 kA total) was assumed and the nonlinear dependence of current density on voltage and the collapsing anode-cathode spacing were taken into account. The results are shown in Figure 5 and indicate that the desired risetimes are achieveable with slight overshoot in the voltage, dependent on the choice of C_2. These data were reproduced experimentally in their essential details as outlined below in the discussion of gun operation.

With regard to the actual circuit components, each stage of the Marx bank was composed of four capacitors in a series/parallel configuration for a per stage capacitance and voltage capability of $1.85\,\mu F$ and 133 kV, respectively. Therefore, total capacitance and maximum erected voltage for the three identical stages was $0.617\,\mu F$ at 400 kV, at a total energy storage of 50 kJ. The peaking capacitor, C_2, was composed of 2 banks and each capacitor bank was formed from five capacitors in series for a total bank capacitance of 40 nF and a stand-off potential of 500 kV.

A mechanical crowbar was included at the output of the Marx bank which disengaged at the point of full charge. This was found necessary to prevent

11
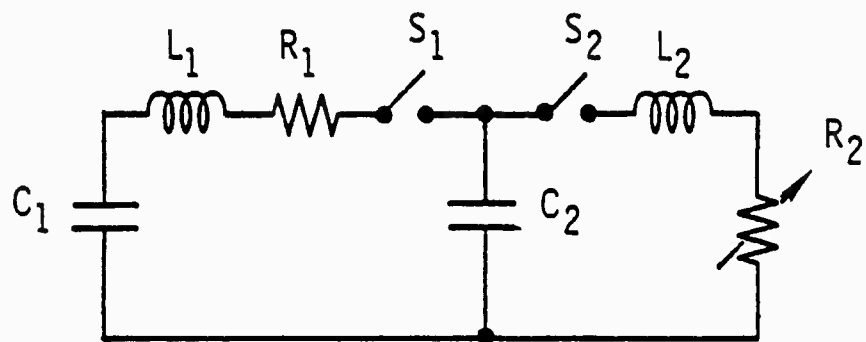
C_1 = Marx capacity = 6.2×10^{-7}, F
L_1 = Marx inductance = 0.9×10^{-6}, H
R_1 = Marx series resistance = $0.15\ \Omega$
S_1 = Switch closes at t = 0
C_2 = Peaking capacitor = 0; 3×10^{-8} F; 1.5×10^{-8} F
S_2 = Switch closes when C_2 charged to 400 kV
L_2 = Peaking circuit inductance = 0.15×10^{-6} H
R_2 = Gun impedance

Figure 4. Electron Gun Equivalent Circuit

12
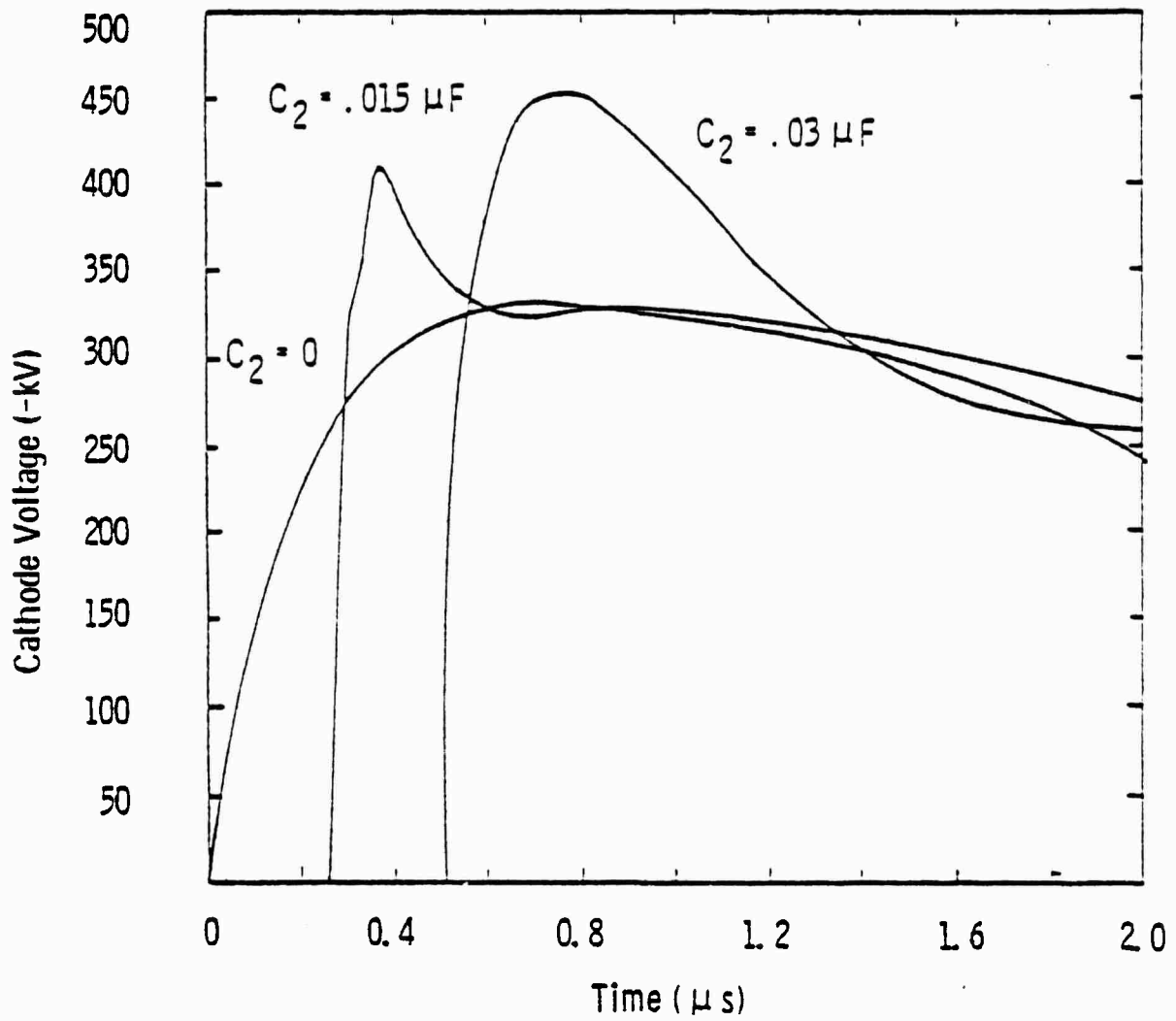
Figure 5.   Equivalent Gun Circuit Response

13

application of voltage to the cathode under conditions of false triggering which otherwise would cause erractic erection of the Marx voltage below its intended level leading to arcing in the vacuum section and possible foil rupture.

The gun voltage was measured with a capacitive divider attached directly at the output of the Marx bank and provided a consistent and accurate monitor of the gun condition. An attempt was made to monitor gun current at each of the feedthroughs and at the Marx ground connection. In the former case, three independent Pearson current probes were installed, one surrounding each of the three current feedthroughs. However, due to the necessity of an extreme high voltage stand-off distance between the feed connection and the grounded probe case, extraneous signals were introduced and that method of measurement was abandoned. The ground connection monitor was found to provide an accurate measurement of total current but was not useful in diagnosing various gun malfunctions and was also abandoned. The gun voltage monitor, correlated with Faraday cup measurements, provided the only reliable gun diagnostic tool.

The console housed all the controls necessary for operation of the gun. This included gauges and setting valves for the switch SF_6 pressures, the delay trigger generator for actuation of the start and stop circuitry, vacuum gauges to determine the condition of the diode section, the Marx bank charging voltage indicator and various interlock mechanisms.

Mechanical Design. Both the cathode and pressure window support were central to the gun design since they directly determined the available current densities and spatial uniformity.

The cathode was composed of 7.6×10^{-4} cm thick tantalum ribbon, spot-welded to a stainless steel sheet base fixture which was then attached to the

14

face of the corona ring. The ribbons projected about 1 cm above the support
sheet and adjacent ribbons, running the 1 M length of the plate, were spaced
approximately 1 cm apart. The entire emitting surface, constructed in this
manner, was 25 x 100 cm^2 in area. Two basic types of cathode were employed
one providing for high current densities on the order of 20 A/cm^2 and the other
providing for current densities up to about 12 A/cm^2. Curvature away from
the anode at the center of the high current cathode was deemed necessary in
order to increase the current density at the cathode edges and so minimize
the counter-effect of beam magnetic pinching. By the Child-Langmuir law
presented above, the central current density would necessarily drop below
that at the edges as a result of increased anode-cathode separation. This
was found to be the case and will be discussed below.

The diode corona ring and specially s aped field grading rings at the
base of the plastic feedthroughs were made of polished aluminum and
swabbed with diffusion pump oil in actual operation. Apparently the thin
film of oil greatly reduced the tendency to arc and therefore increased
general machine reliability.

The cathode structure and corona ring were mounted on moveable,
vacuum tight shafts which projected through the plastic feedthroughs into
the Marx tank. This allowed variation of the anode-cathode distance through a
mechanism external to the vacuum vessel without destroying the diode vacuum
integrity.

The pressure window was composed of a complex sandwich of screens
and foils as shown in Figure 6. In their path from the cathode surface to the
high pressure cell, the electrons are seen to traverse a 1.8×10^{-3} cm
thick aluminum ground foil, a vacuum drift space between the support webs,
a support screen, a 5×10^{-3} cm thick pressure bearing foil and finally the
arc protection screen.

15
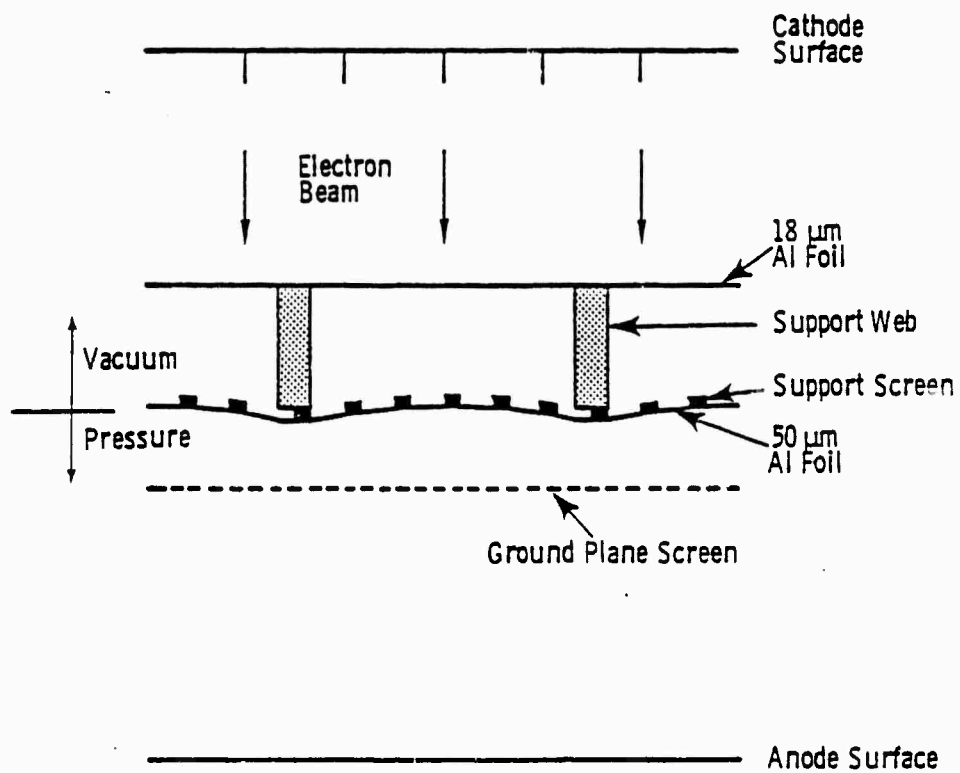
Figure 6. Foil Support Structure

The ground foil was necessary to provide a uniform ground plane for the cathode since in its absence arcing would occur to the sharp support webs. This effect was aggravated by the requirement of high current densities which necessitated a small anode-cathode separation. The ground foil also served to absorb low energy electrons generated during the voltage rise, thereby preventing unnecessary heating of the second foil under stress by high pressure gas.

The support web structure was developed to provide the greatest open area consistent with operating pressures up to 5 atm and the expected beam incidence angles due to magnetic deflection. As a result, the design called for deep, widely spaced webs with a superimposed support screen. The support webs were formed in a ladder configuration, machined from a solid plate of aluminum. All the webs were 0.8 cm thick and spaced so as to provide for open squares of 49 cm^2 area. Those webs running longitudinally down the 1 M extent of the ladder were 3 cm deep and those in the 20 cm transverse direction were 2 cm deep.

The support screen was stamped from .16 cm thick stainless steel in a pattern which allowed for 0.6 cm^2 open squares and 8×10^{-2} cm wide minor ribs. The resulting configuration of support webs and support screen resulted in a geometrical beam transmission factor of 65%. Of course, the actual beam transmission factors were reduced somewhat from this value due to the angular trajectories of electrons striking the support ladder. This effect is taken up below in consideration of beam uniformity.

The 5×10^{-3} cm thick high pressure-vacuum interface foil was formed from aluminum alloy #5056-H19, since this afforded the highest yield strength for the foil temperature rise expected. The maximum pressure called for in the experimental program was 4 atm absolute and under this condition

the foil and its support structures performed satisfactorily under electron beam operation.

Finally, a screen was placed over the foil but separated from it by 1 cm, and served the function of providing a uniform ground plane opposite the discharge anode. Secondarily, arcs generated in the discharge process were terminated on the screen thereby preventing foil rupture. The screen was 70% transmissive and was woven from 0.16 cm diameter stainless steel wire.

Diagnostics. The most important aspects of gun performance were current density and deposition uniformity. In order to determine these properties as accurately as possible, several diagnostic techniques were employed. With regard to current measurement, a 0.635 cm diameter Faraday cup was used to measure temporal behavior and a check on absolute current was made with a Pearson current probe and found to correlate within 10%[33]. Overall spatial uniformity was measured with electron dosimetry film (cinemoid) and calibrated with the Faraday cup which provided excellent spatial resolution owing to its small diameter.

The Faraday cup consisted of the innermost, 0.635 cm diameter aluminum collector surrounded by a pyrex insulator and an outer stainless steel sleeve, connected to the signal cable shield. Crucial to proper operation was the application of insulating tape over the probe end which prevented charge buildup on the collector from shorting either to the shield or to the foil through the plasma generated in air by the electron beam. The signal was transmitted directly to the proper attenuators and a 50 ohm termination at the oscilloscope. With this technique, spurious signals generated by EMI were kept to approximately an oscilloscope trace width.

---

[33] Pearson Electronics, Inc., Palo Alto, California.

A check on the Faraday cup accuracy was performed with the apparatus shown in Figure 7. The entire output aperture of the beam, just beyond the foil was blanked off with the exception of a 2 cm diameter hole in the center which allowed access to a small portion of the beam. A plastic insulator and aluminum collector were fitted into the hole and the collector was returned to ground through the Pearson current probe. The Faraday cup was fitted to the same blank off plate to provide simultaneous measurement. As mentioned above, the absolute current correlated within 10%, with the Faraday cup reading slightly low, and no difference in the two temporal waveforms was discernible.

Spatial plots of the beam output aperture were made with electron dosimetry film and simultaneously with the Faraday cup over a limited spatial extent. It was found that the spatial gradient determined from the film with a transmission densitometer was within 25% of that measured with the Faraday cup.

Electron Gun Performance. Typical oscilloscope traces are shown in Figure 8. Figure 8a indicates Marx voltage and beam current measured with the Faraday cup at the foil pressure window, in the absence of the capacitive peaking circuit. The voltage is shown to rise to roughly half its maximum value before the output current starts, the delay being due to the requirement for substantial cathode voltage for emission. Total voltage risetime is 200 ns, whereas the current risetime is about 300 ns. Beyond the 300 ns point in the current pulse, the slope is still positive, however, this further increase is attributable to the decreasing effective anode-cathode distance as the emitting plasma propagates from the cathode blades to the anode plane. The current waveform, as indicated by the small diameter Faraday cup, shows only slight modulation superimposed on the basic sinusoidal shape. Three Faraday cups separated by 7 cm in the output window major direction and
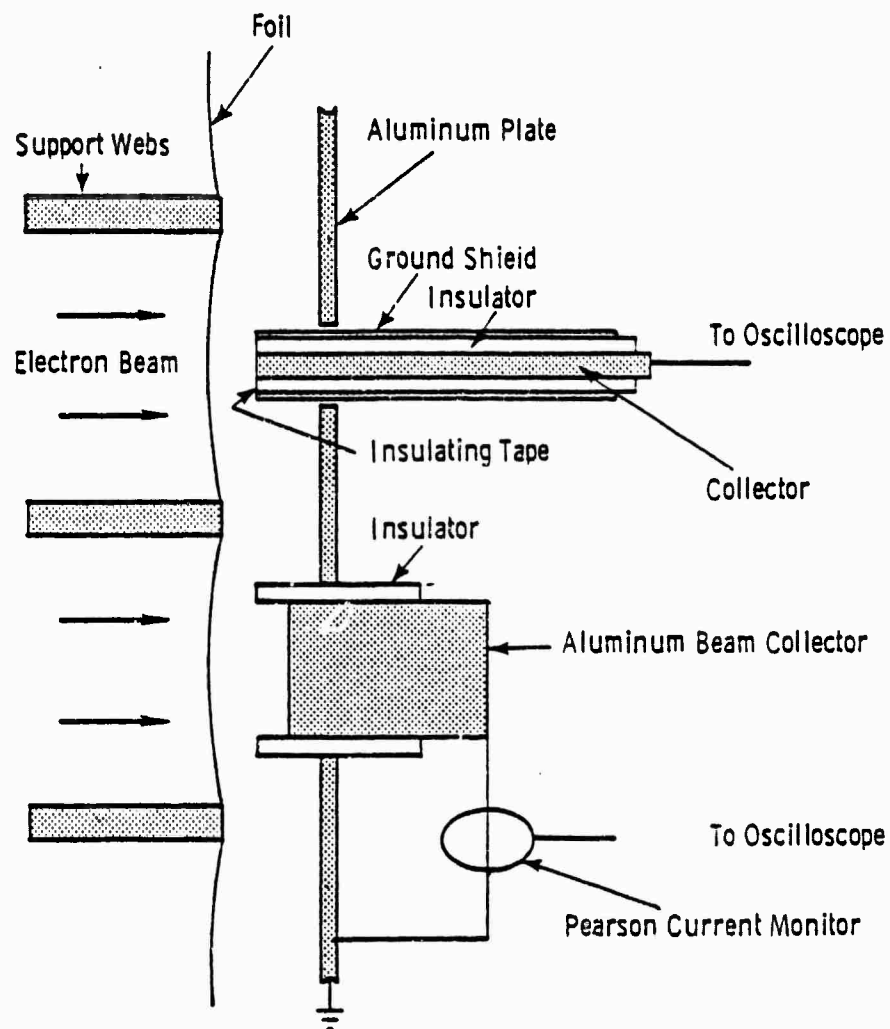
Figure 7.   Current Density Calibration Apparatus

20

(a) Peaking
Capacitance = 0
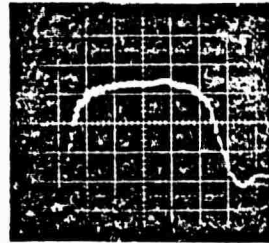
Voltage
70 kV/Div
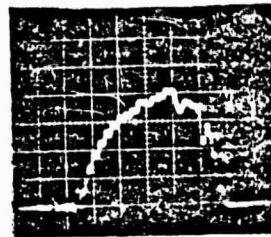
Beam Current
3A/cm^2/Div

| | 200 ns

(b) Peaking
Capacitance = 40
nF
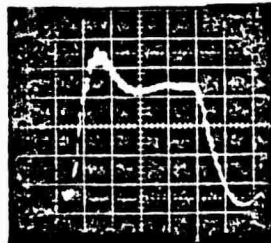
Voltage
70 kV/Div
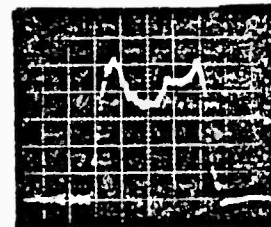
Beam Current
3A/cm^2/Div

→| |←200 ns

Figure 8. Typical Gun Performance Traces

21

operated simultaneously, showed the same basic temporal shape but no correlation in the modulation. Therefore, the slight noise was not due to common mode signals and was spatially randomized, at least over distances of 7 cm.

Figure 8b shows both Marx voltage and resultant output current with the peaking circuit connected. In this case, the voltage risetime is about 100 ns with a 20% overshoot beyond the average value. This is reflected in the fast rising current pulse and leads to more severe modulation which is further accentuated by the plasma propagation mechanism indicated above. A series of Faraday probes, operated as outlined above, showed the same relative behaviors.

Overall uniformity measurements were made with electron dosimetry film which was shown to be sensitive to electron current but insensitive to x-rays. Bleaching of the film was therefore related directly to the electron current density and measurement of this effect with an optical transmission densitometer afforded a direct indication of beam current gradients. Typical profiles obtained in this manner with the film in contact with the foil are shown in Figures 9 and 10. Figure 9 indicates the beam current distribution along the central major axis of the output window for the high density cathode. The accentuated emission at each end is due to the slight cathode curvature as mentioned above and enhances beam uniformity deposition in the high pressure gas at these areas which would otherwise show severe end gradients due to gas scattering. Similar results were obtained with the low density cathode at central current densities of 10 A/cm^2. In this latter case, the increase in end intensity was not as pronounced.

Figure 10 indicates the transverse beam uniformity, scanned from the center of the foil to the top across the output aperture minor axis.

20 A/cm^2 →

Distance (cm)
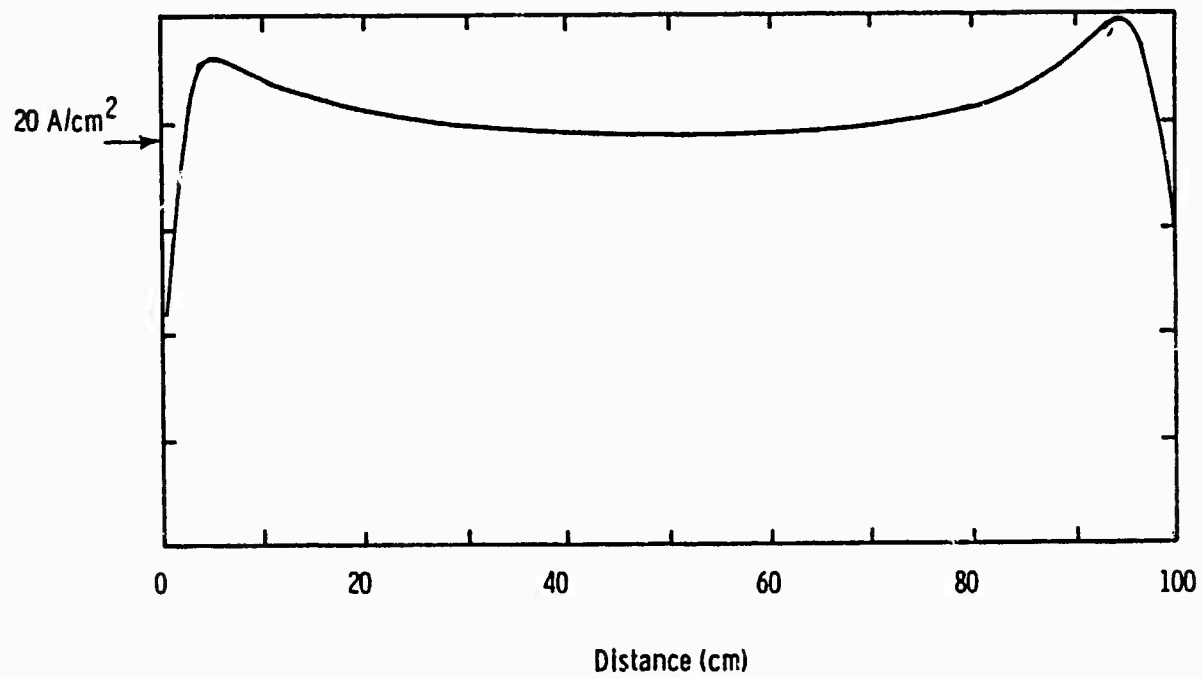
Figure 9.   Longitudinal Beam Current Profile

23
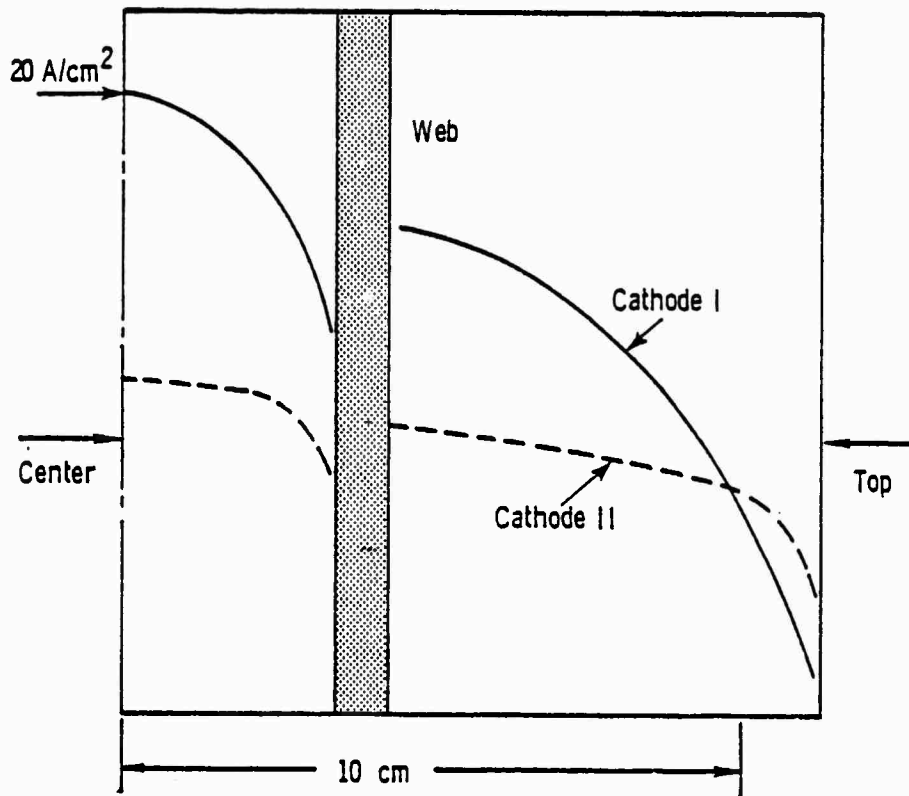
Figure 10. Transverse Beam Current Profile

Characteristic of the high density cathode I is a severe gradient in this dimension, enhanced by the presence of the deep supporting webs. The fall-off in current from 20 A/cm^2 at the center to roughly half this value at the left edge of the web is likely due to the interception of those electrons approaching the right side of the web at large entrance angles due to vacuum magnetic field pinching. Simple calculation of this angle assuming the electrons move at relativistic velocity in the magnetic field established by the vacuum beam current, indicates an entrance angle of about 42° to the normal. This is close to the value indicated by the data of Figure 10, assuming major obscuration over about 3 cm to the left of the web and a web depth of 3 cm. With dosimetry film placed 5 cm away from the foil in air, these large gradients in beam current measured at the foil were not detectable due to randomized gas scattering. The actual experimental conditions called for 1.7-3 atm of Argon, which further reduced the gradients.

Deposition uniformity in the beam direction into the high pressure gas was perhaps the most important characteristic, due to considerations of discharge stability to be discussed with the experimental results. In order to determine the extent of this important effect, both theoretical calculations and experimental estimates were undertaken.

The theoretical effort was based on an electron, Monte Carlo scattering computer code which calculated the combined effects of foil scattering, gas scattering and secondary emission from the anode [34]. Results for a 350 keV beam passing through a 50 μm thick foil and impinging on 3 atm of Argon are shown in Figure 11. The view shown is made to simulate the end view of the present apparatus which had a total beam aperture of 20 cm and a maximum anode-cathode separation of 10 cm. The contour lines indicate

[34] J. A. Halbleib, Jr. and W. H. Vandevender, "Cyltran: A cylindrical-Geometry Multimaterial Electron/Photon Monte Carlo transport Code", Sandia Laboratories, Albuquerque, New Mexico 87115.
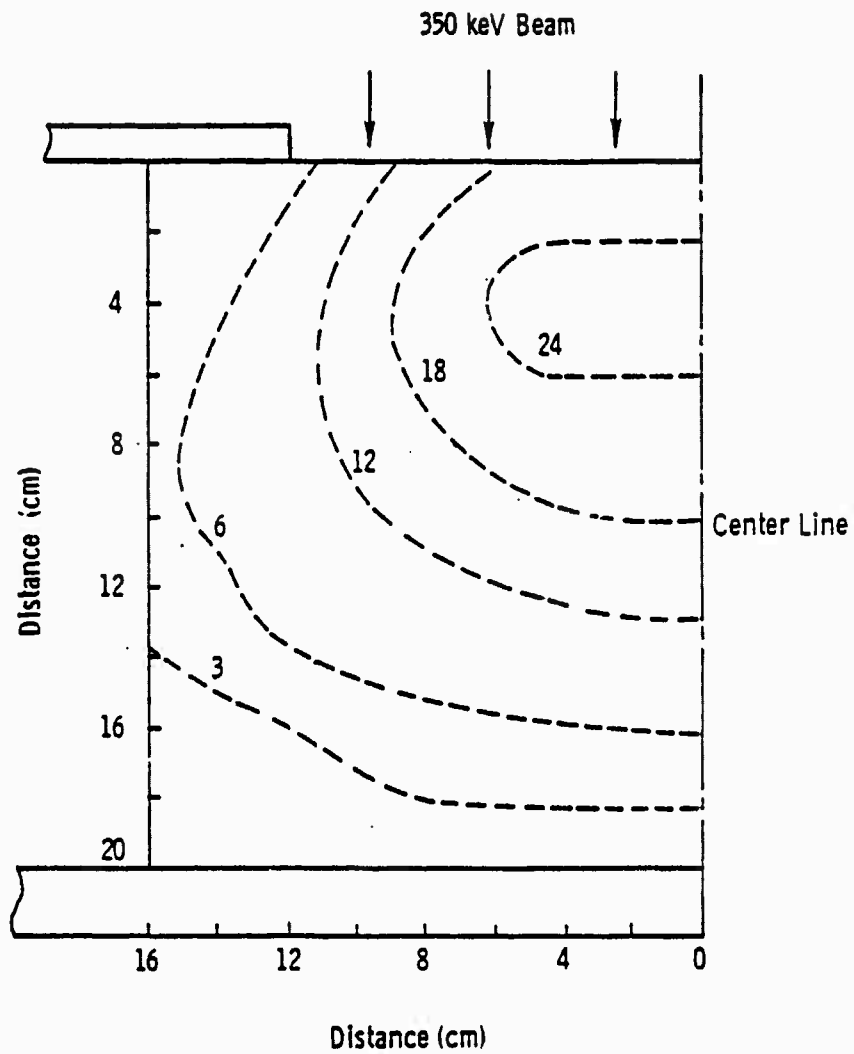
Figure 11. Computed Energy Deposition Profiles

points of constant energy deposition in keV/cm which when multiplied
by the initial current density in A/cm^2, indicate power deposition in kW/cm^3.
The analysis shows that a peak in the deposition occurs at about 4 cm into the
gas after which it falls off by 25% over 10 cm. In the other direction, from
center to edge, the fall off is roughly 50%.

An approximate experimental measurement of beam current density
fall-off with distance from the aluminum foil was attempted by placing both
dosimetry film and a Faraday cup within the high pressure laser cell. The
two techniques correlated within about 20% and indicated a very pronounced
current density fall-off as shown in Figure 12. The beam energy was 320 keV,
and the cell was pressurized with argon. These measurements, of course,
indicate current density only, however, an independent measurement of total
energy deposition via spatially resolved fluorescence in a separate device at
NRTC yielded substantially similar gradients[35].

It will be shown in a subsequent section dealing with the experimental
results how nonuniformities in beam energy deposition were directly
reflected in the laser output energy profiles and how such nonuniformities
greatly limited the attainable discharge energy input.

2.2 Laser Plenum and Gas Handling. Design of the laser plenum and the
associated gas handling apparatus was guided by the requirements for operation
with halogens mixed in high pressure diluents. Additionally, the plenum
geometry was constrained by the necessity for low discharge current return
path inductance. With regard to materials, it was considered crucial that
those appropriate to proper passivation and operational cleanliness be
chosen. Therefore, all metallic parts were constructed out of either
stainless steel or aluminum, and teflon was used for all insulating areas. In

---

[35]J. West, Northrop Research and Technology Center, private communication.

27
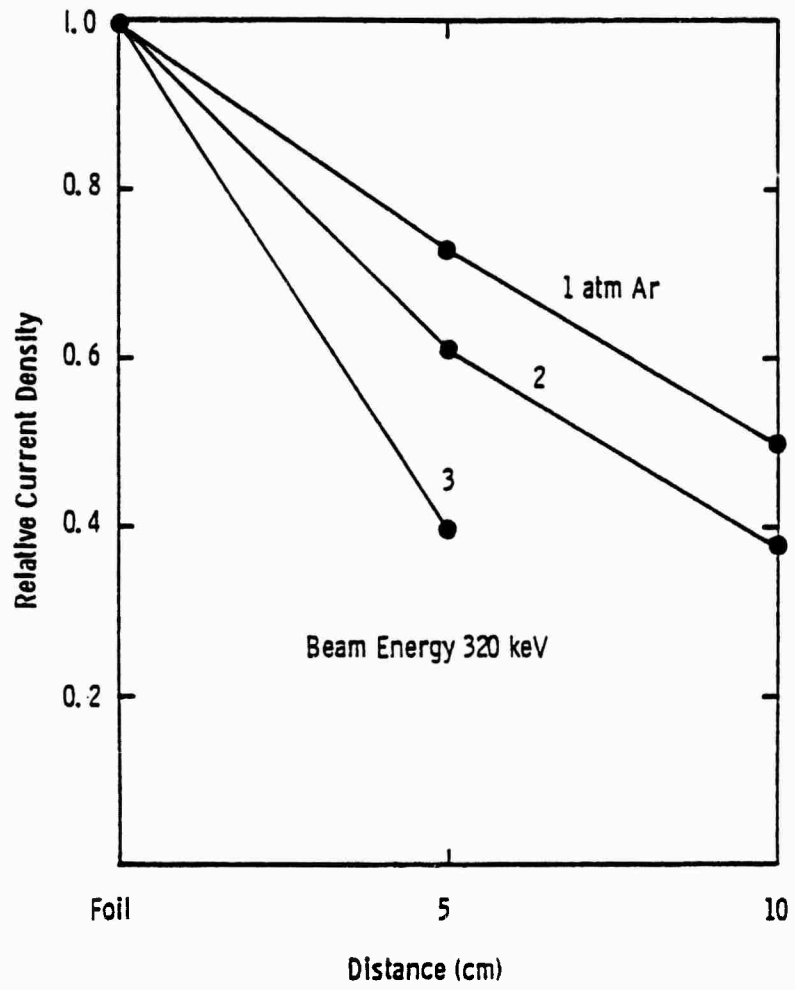
Figure 12. Current Density vs Distance from Foil

28

order to minimize discharge circuit inductance, the basic plenum design called for four parallel discharge current feedthroughs and a 300 liter high pressure cell in roughly a semi-cylindrical geometry.

Operationally, the apparatus performed as designed. The important limitation to the geometry was foreseen as arcing either from the discharge electrode to the chamber walls or tracking along the teflon feedthrough insulators. Neither occurred except under extreme tests, wholly unrepresentative of actual experimental conditions.

Laser Plenum. The high pressure laser plenum was formed from a stainless steel, half-cylinder attached to a massive flange which provided an interface to the electron gun. Material sizes and methods of construction were consistent with a 10 atm static pressure load, assuming fill pressures up to 5 atm and 10 atm, pulsed over-pressures. Safety factors were therefore judged to be a factor of five. The plenum and the pumping apparatus attached to it were in turn secured to an oil filled, aluminum container housing the discharge switching circuitry and capacitor bank. The two attached structures were then allowed to roll on a track providing for separation from the electron gun for servicing both the electron gun and the plenum interior. These components are shown in detail in Figures 13 and 14 which provide an end and front view, respectively. A picture of the assembled apparatus is shown in Figure 15.

Figure 13 shows the method of attachment of the plenum to the discharge capacitor bank housing as well as the placement of the pumping apparatus. With regard to the pumping method, a 6" diameter diffusion pump with a liquid nitrogen cold trap was used and found capable of pumping the entire system down to 5×10^{-5} mmHg before each gas fill.

Figure 14 indicates the positions of the four discharge current feeds and a fifth feed which allowed direct attachment of voltage sampling circuitry to the
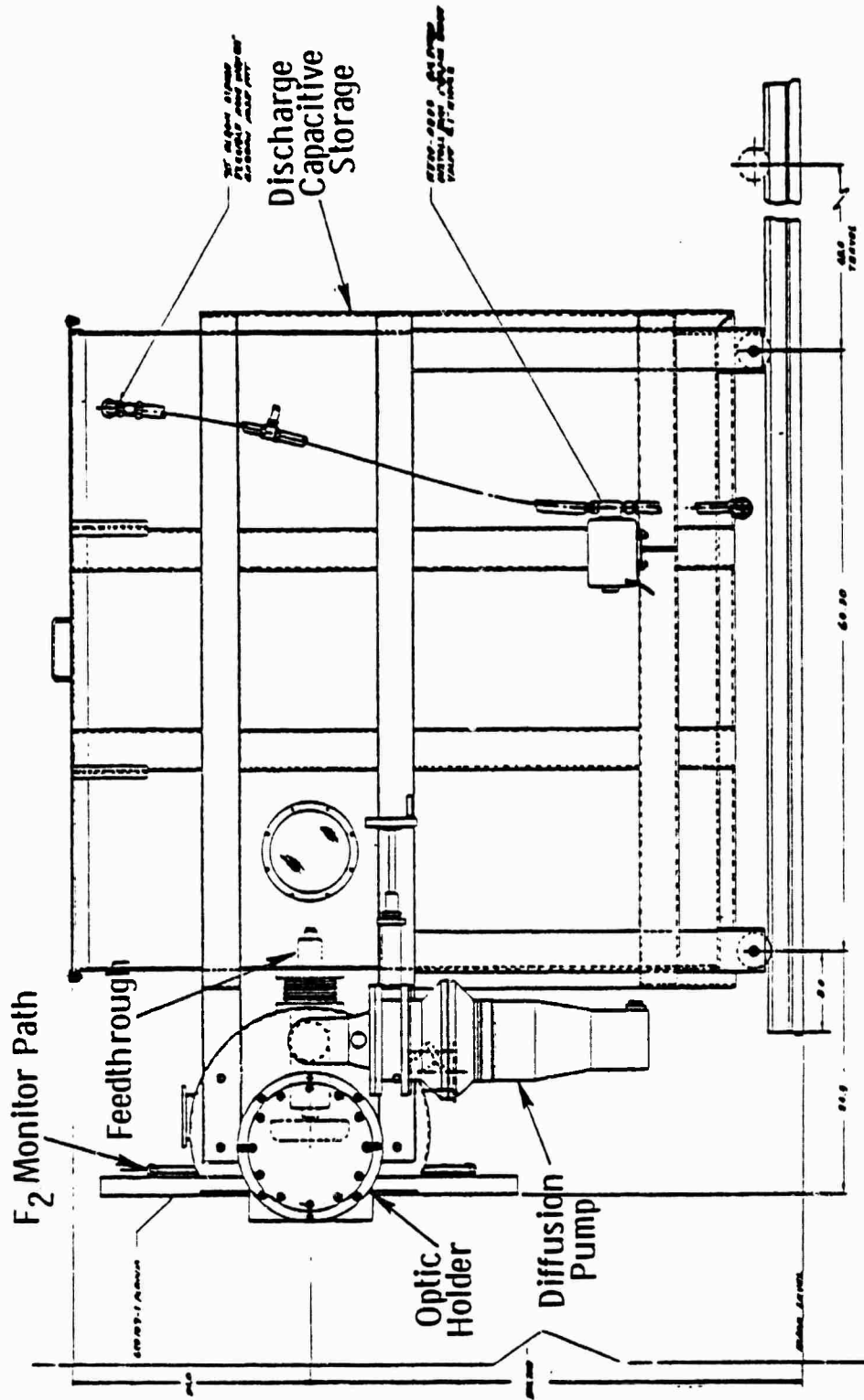
Figure 13. Laser Plenum-End View

30

Figure 14. Laser Plenum-Front View
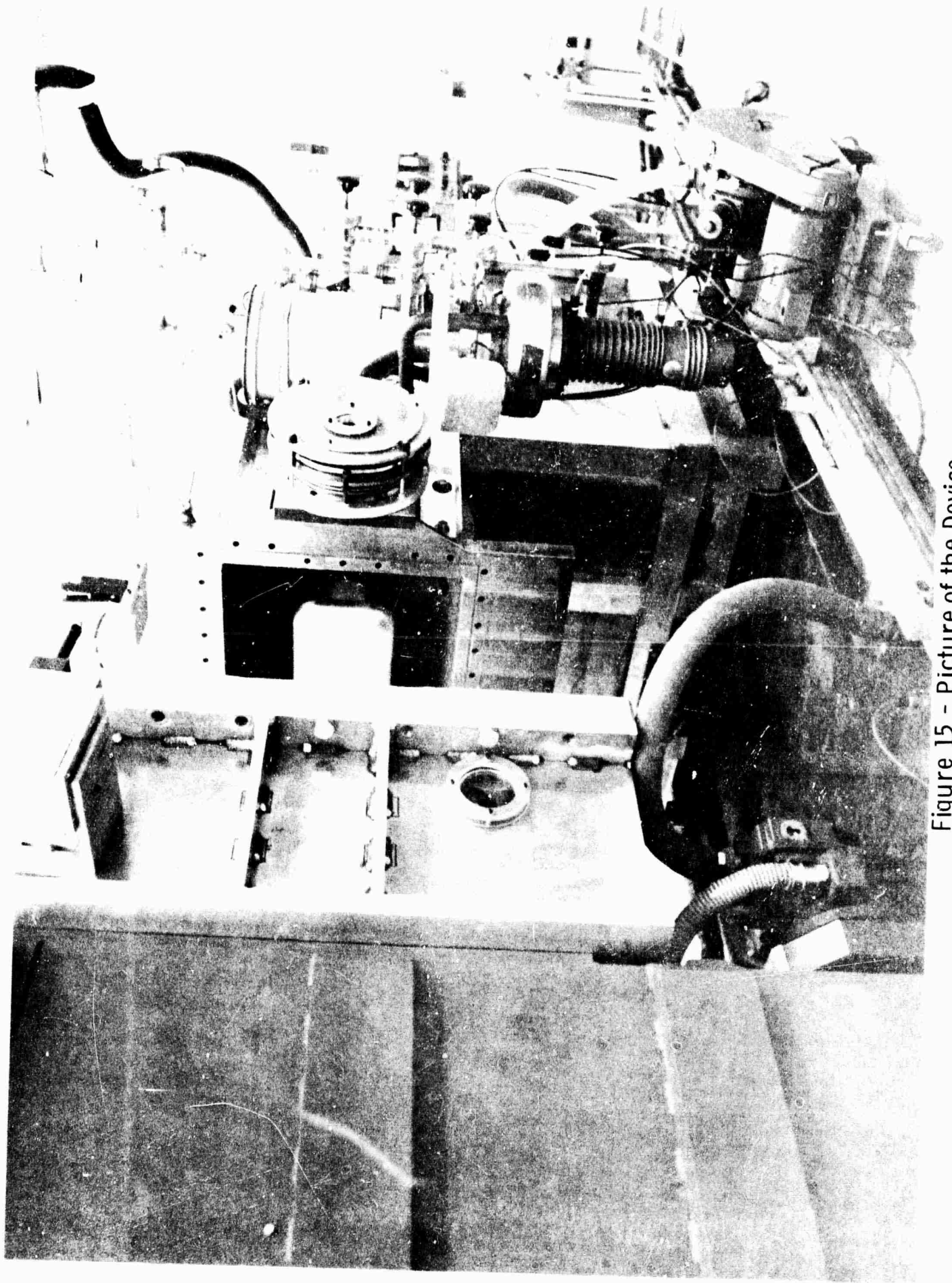
Figure 15 - Picture of the Device

discharge electrode. Also shown is the diagonal optical path for the He-Cd laser used to monitor F_2 partial pressure through absorption at 3250 Å. These diagnostics are discussed below.

Detailed schematics showing the relative positions of the important elements are shown in Figures 16 and 17. Of special interest are the feedthrough geometry, anode attachment and shape, and optical attachment and method of adjustment.

Insulation of the high voltage feedthroughs inside the plenum was provided by the teflon sleeving. Outside this volume, insulation was provided by the transformer oil which was allowed to penetrate the bellows attachment area from the discharge capacitor tank. Attachment to the discharge anode was made via a slip collar, allowing for adjustment of the anode-cathode dimension from a maximum of 10 cm to a minimum of 2 cm. The anode itself, of overall dimension 20 x 100 cm^2, was formed from aluminum into a Rogowski profile consistent with a 10 cm electrode spacing. The profile geometry was considered successful in that traces of arcing at all anode-cathode separations took the form of diffused blemishes along the central third of the electrode, and no tracking was observed along its perimenter. Contributing to this success was the presence of a uniform ground plane presented to the electrode well beyond its edges, as indicated.

Placement of the optical extraction area in relation to the excitation volume was crucial, owing to the nonuniformity of energy deposition in the high pressure gases. As indicated in the accompanying figures, extraction was obtained immediately beyond the ground plane screen, however, the extent of the extraction area in the anode direction depended upon the optical holder profile. In this regard, two types of holder were used providing for optical path lengths of 1.2 and 2.0 M. The first, shown in heavy lines in the

33
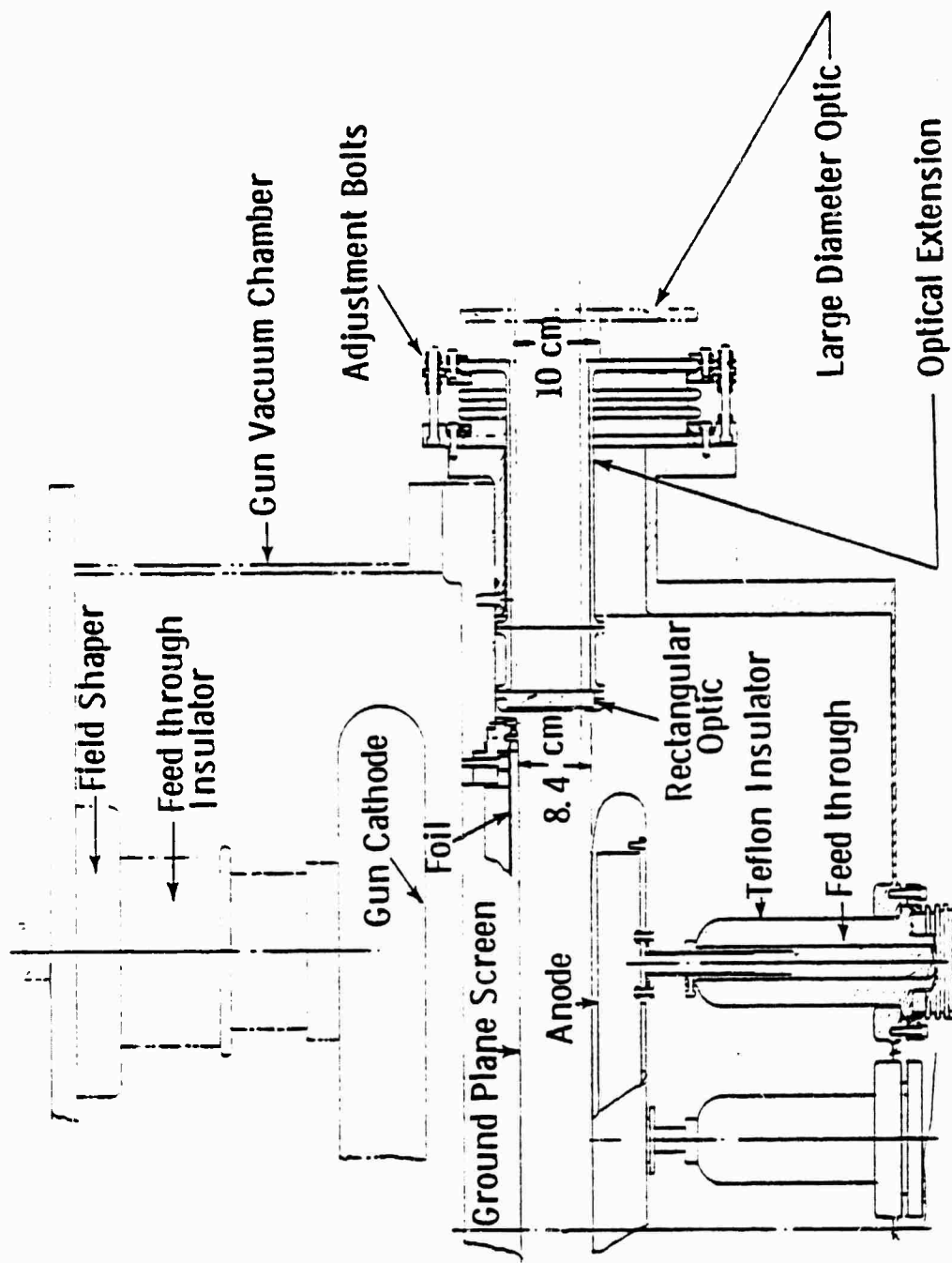
Figure 16. Detailed Plenum Side View

Field Shaper
Feed through Insulator
Gun Cathode
Foil
Ground Plane Screen
Anode
8.4 cm.
Gun Vacuum Chamber
Adjustment Bolts
10 cm.
Large Diameter Optic
Optical Extension
Rectangular Optic
Teflon Insulator
Feed through

Rectangular Optic

Large Diameter
Optic Holder

Teflon Insulator

Gun
Cathode

Ground
Plane
Screen
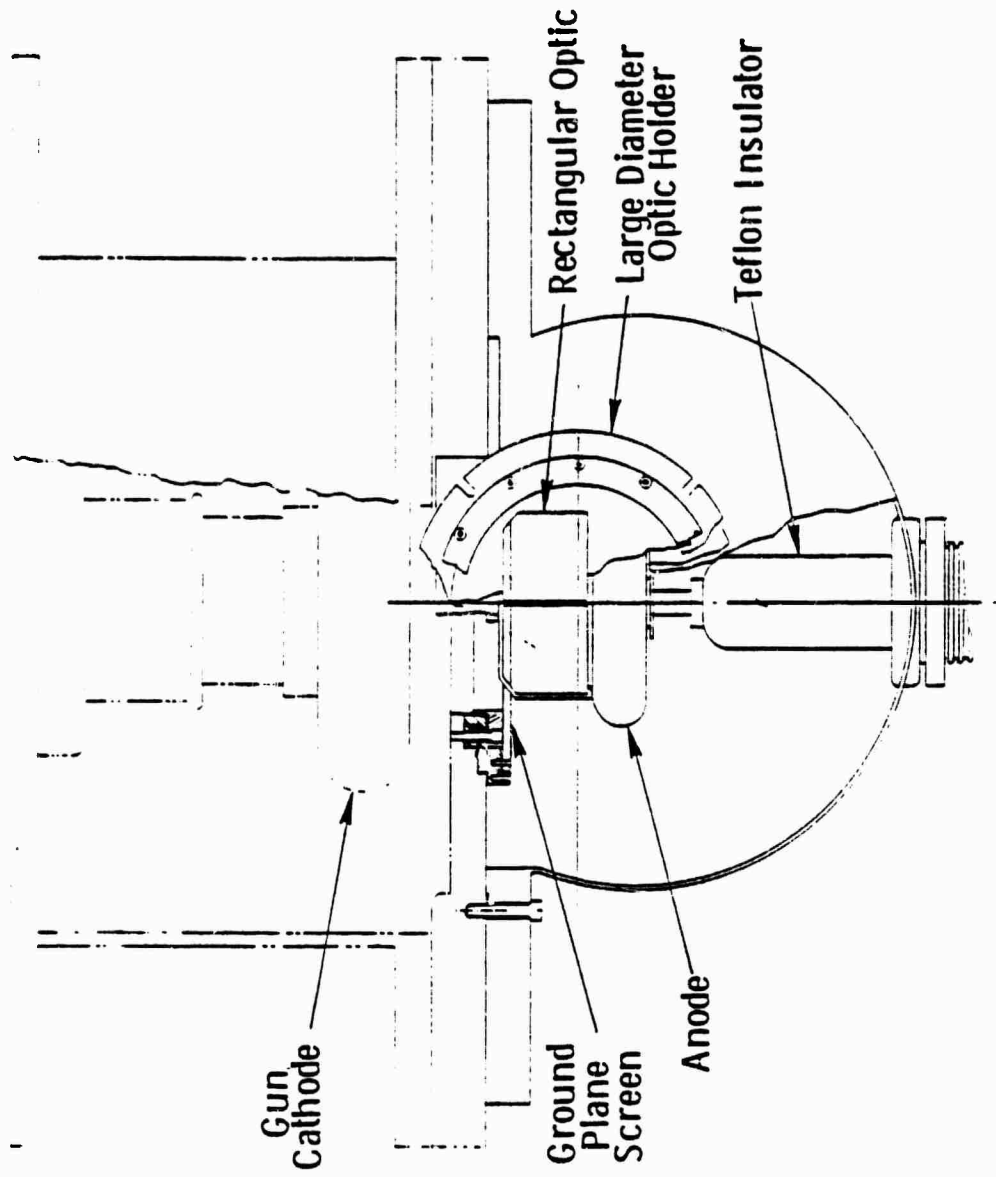
Anode

Figure 17. Detailed Plenum End View

35

figures, provided for extension of a 10 x 20 cm^2 optic well inside the plenum volume and in this case, the available distance in the anode-cathode direction open for extraction was 8.4 cm. The second method used a large, 28 cm diameter optic indicated by the dotted outline in Figure 16 attached directly to the exit port, thus providing for extraction over the full 10 cm anode-cathode dis' nce. In both arrangements, adjustment of the optics was provided by the rnal adjustment bolts attached to the flexible bellows assembly. The provision for changing optical path length at the expense of total extraction volume was important, since it was shown experimentally that the decrease in path length indicated above enhanced the specific energy extraction by about 50%.

Gas Handling. The gas handling system was designed to fulfill several important criteria. The entire system was required to safely handle Fluorine at high pressures in the storage and passivation procedures. This also included the parallel accomodation of high pressure rare gases without contamination ard with additional purification if indicated. Proper mixing of the various gas constituents at high pressure was to be guaranteed before each electron gun burst. A continuous monitor of the F_2 partial pressure was to be provided since this crucial constituent was present in small amounts and subject to chemical reaction at the chamber surfaces. These various topics are described below in detail including the operational experiences. It was found, in general, that the entire system performed well above the experimental requirements.

The gas storage system was by conventional means with an explosion-proof casing for the Fluorine and standard high pressure bottles for the rare gases. Commerically available gases were used and this included Argon (99.998%), Krypton (99.995%), Xenon (99.995%), Neon (99.99%) and Fluorine (97%). No attempt was made to verify the analyses provided by supplier and Fluorine was not purified beyond its stated level. However,

an attempt was made to eliminate water vapor and hydrocarbon contaminants through the use of alumina gel and molecular sieve filters. It was found that the laser behavior did not change with the addition of these filter types. The gases were admitted through well passivated stainless steel tubes to the laser plenum where mixing took place. The partial pressures of Fluorine, on the order of 2-4 Torr, and Krypton, on the order of 100 Torr, were measured with a capacitance manometer which used a stainless steel diaphragm in contact with the gas. The higher total pressures, on the order of 2-4 atm, were measured with stainless steel Bourdon tube gauges.

A high capacity cryo-pump was used to reclaim the costly rare gases. The pump was composed simply of an aluminum cylinder surrounded by a liquid nitrogen bath. Gas which was subjected to about twenty bursts with the electron beam and reclaimed in this manner showed no degradation due to contamination. Upon re-use, no change in laser performance was apparent.

Using a He-Cd laser source, absorption at 3250 $\overset{\bullet}{A}$ was used to monitor F_2 partial pressure in the presence of high pressure rare gases in the laser plenum before each electron gun burst. The monitor also provided an indication of the gas mixing time after high velocity injection of the rare gases through the small inlet orifice. The absorption coefficient of 0.1 atm^{-1} cm^{-1} was checked for the 1.7 M absorption path length with the capacitance manometer in pure Fluorine at low pressures[36]. For these low concentrations, total absorption was 5%/Torr of F_2, well within the resolution of the apparatus. It was estimated that accuracies of 0.25 Torr were realised. It was also determined that the absorption was dependent only upon the F_2 level and independent of the neutral rare gas pressure. Since the technique provided an "on-line" measurement of F_2 partial pressure, disturbances in concentration

[36] J. S. Whittier, M. L. Lundguist, A. Ching, G. E. Thornton, R. Hofland, Jr., J. Appl. Phys. 47, 3542 (1976), and private communication.

along the absorption path were discernible during the mixing process. Mixing was considered complete when the absorption level measured before introduction of the rare gases was attained. Mixing times were on the order of several minutes and operation of the laser at times greatly in excess of this value showed no change in performance.

The arrangement of the monitor is shown in Figure 18. A 2 mW, He-Cd laser operating at 3250 Å was used as the cw source with the output split into two paths, one propagating in air as the reference and the other propagating diagonally through the laser plenum adjacent to the discharge ground screen. A chopping wheel was used to allow the receiving photodiode to sample each beam alternately. The photodiode output was displayed on an oscilloscope and the difference signal interpreted directly as a measure of absorption. Absolute calibration of the system was easily accomplished with the plenum evacuated, in which case the angle sensitive attenuator was adjusted to give zero difference signal.

2.3 Discharge Circuit. Discharges in the high pressure gas mixtures typical of the KrF laser are characterized by very low resistance. For devices of the size under discussion, the characteristic discharge impedance, a function of time, is on the order of 0.25 ohm. In this application, typical high voltage pulsed circuits are limited by their inherent inductance which can be on the order of 100-200 nH. The immediate problem, then, is one of adapting conventional pulsed discharge circuitry, which normally requires high impedance loads for efficient energy transfer. Design of the present discharge circuit was therefore guided by the requirement for minimization of total circuit inductance. The basic circuit itself was of a simple capacitive discharge type with subsequent modification into a two stage, pulse charged configuration in an attempt to circumvent a portion of the circuit inductance.
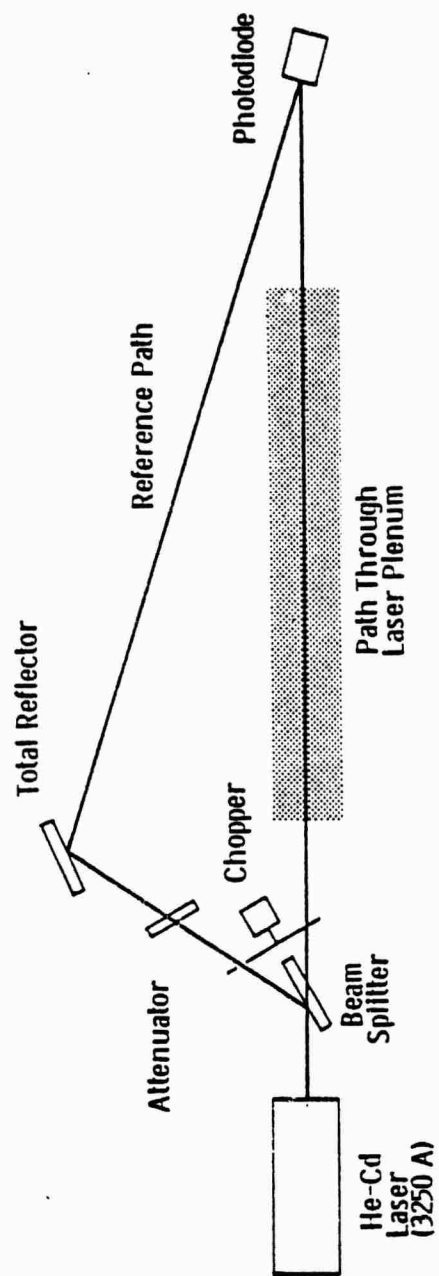
Figure 18. F$_2$ Monitor Arrangement

39

An extensive circuit analysis was first undertaken with best guess parameters. Based on design criteria obtained in this fashion, the actual circuit was constructed and tested with a fixed dummy load. It was found that the circuit behaved substantially as predicted and that the total circuit inductance was about 225 nH as estimated.

Circuit Analysis. The discharge circuit model is shown in Figure 19 with a typical set of component values. Three parallel sets of capacitive storage are indicated, each with a series inductance of 50 nH and resistance of 0.001 ohm. The load is represented by the variable resistance, R, and the balance of the circuit including the switches and feedthroughs is approximated by the 150 nH inductance and 0.010 ohm resistance. The circuit pictured is a Chebishev filter, modified to work into a low impedance load[37]. Basically, the various capacitive and fixed inductance legs can be thought of as contributing different frequency components to the final waveform observed at the load. The complication arises in the interaction of the various legs among themselves. Calculation of the fairly complex resultant waveform was undertaken with a computer code which correctly modeled all aspects of the circuit. The component values were extensively varied theoretically with the result that those indicated were optimum.

In order to determine the circuit sensitivity to inductance, the output was calculated for various experimentally attainable values of inductance; and a load resistance of 0.5 ohm. The result is shown in Figure 20. For an initial charge voltage of 100 kV, a change in inductance from 50 to 200 nH results in a factor of two increase in risetime to maximum voltage, and over this range, the maximum achievable voltage applied across the discharge drops from 80 to 65% of the initial charge voltage. Considering

---

[37]Reference Data for Radio Engineers, Fifth Edition, Howard W. Sams & Co., Inc., p. 8-24 (1968).
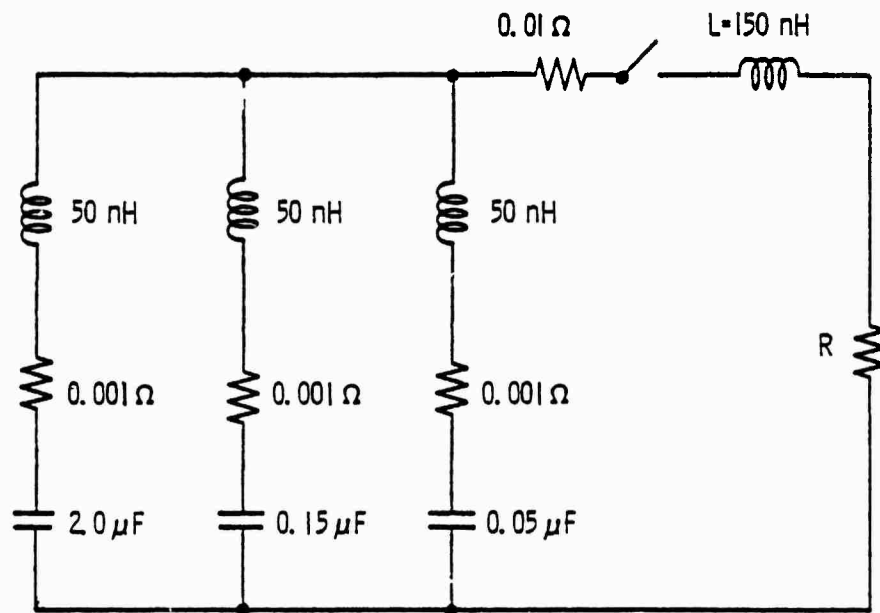
Figure 19.   Discharge Circuit Model

41
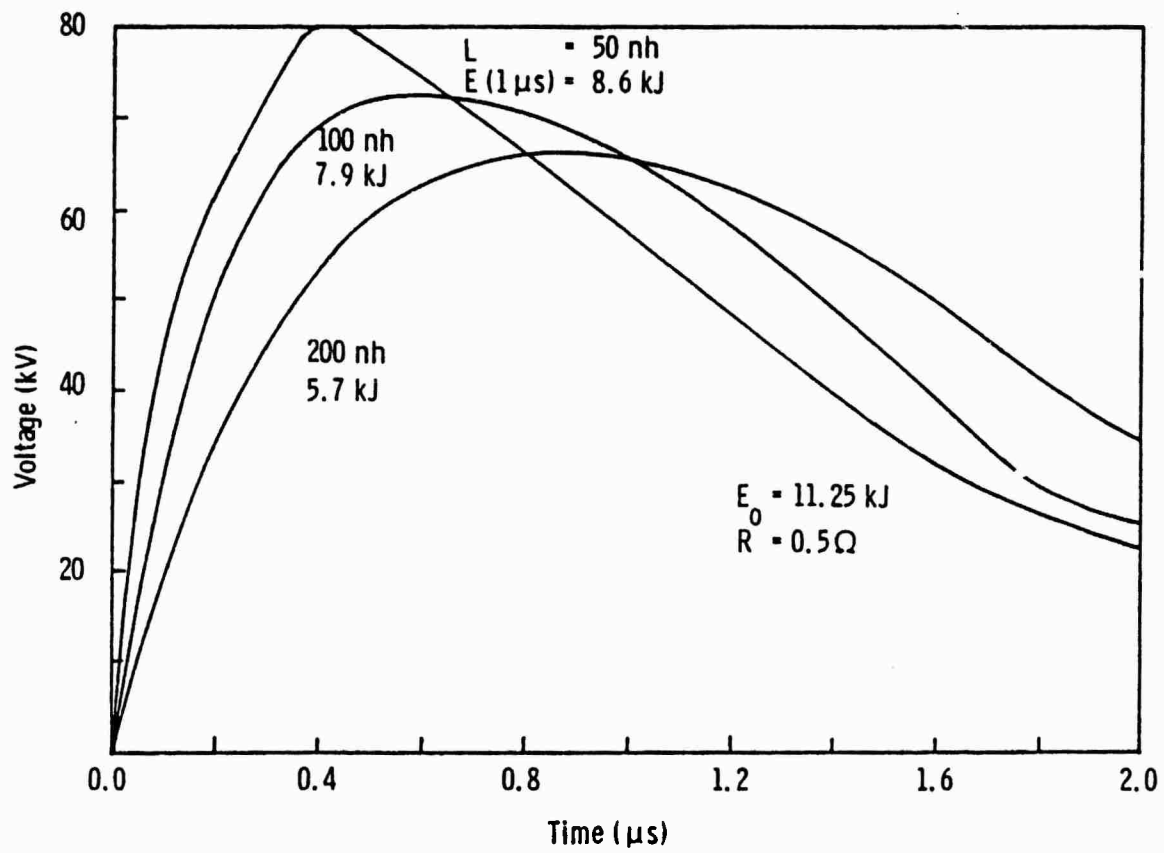
Figure 20. Circuit Response to Variable Inductance

a nominal 1 μs pulse length, the total input energy likewise drops from 8.6 to 5.7 kJ. Inductance is therefore crucial to discharge performance. Figure 21 shows the circuit response to variable load impedance assuming a circuit inducatnce of 150 nH in addition to the 50 nH in each circuit leg. Since the electron beam current density determines the load impedance through primary ionization, each load resistor is associated with a beam current density. Additionally, each value of current density determines the pulse length according to limitations of the cold cathode electron gun technology. For the 0.5 ohm curve, the 2.0 μF capacitor has been increased to 4.0 μF in order to minimize voltage droop over a 2 μs pulse. The combination of low load impedance with a moderately high circuit inductance results in very poor energy coupling into the discharge. The maximum applied voltage is seen to drop from 70 to 45% of the charge voltage and risetime is extended from 400 to 700 ns. The spans shown at the right border of the graph indicate the extent of optimum E/N for 2 and 3 atm total pressures and a 10 cm anode-cathode separation. The implication is that even in the presence of poor discharge coupling, the experimental parameters are within a useful range.

An attempt was made to circumvent a portion of the circuit inductance by placing additional capacitance and a series switch directly across the load, as indicated in Figure 22. Here, C_1 and the 200 nH series inductance represent the initial circuit, C_2 and its 50 nH series inductance represent the circuit addition, the 50 nH inductor in series with the load represents the remaining circuit inductance, and the additional switch is provided by the electron beam which induces an instantaneous impedance collapse from infinity to 0.2 ohms across the discharge. Physically, these modifications were carried out by placing capacitors encased in Pyrex cylinders directly within the laser plenum beyond the major current feedthroughs and switches. The discharge was operated by charging the main bank, C_1, switching this onto C_2 and waiting approximately 1 μs for voltage buildup, and then firing the electron gun which allowed current to flow through the medium from the

43
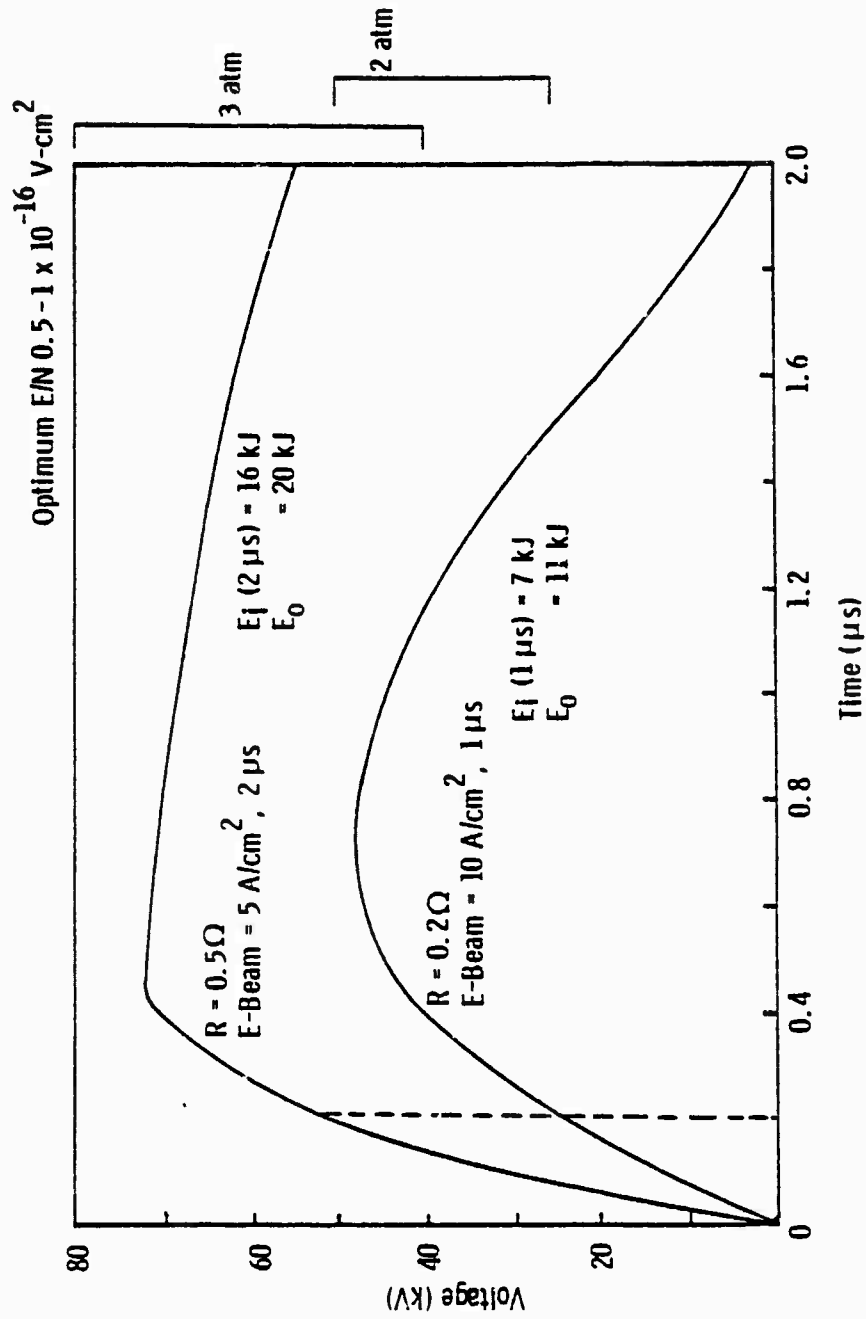
Figure 21. Circuit Response to Variable Resistance
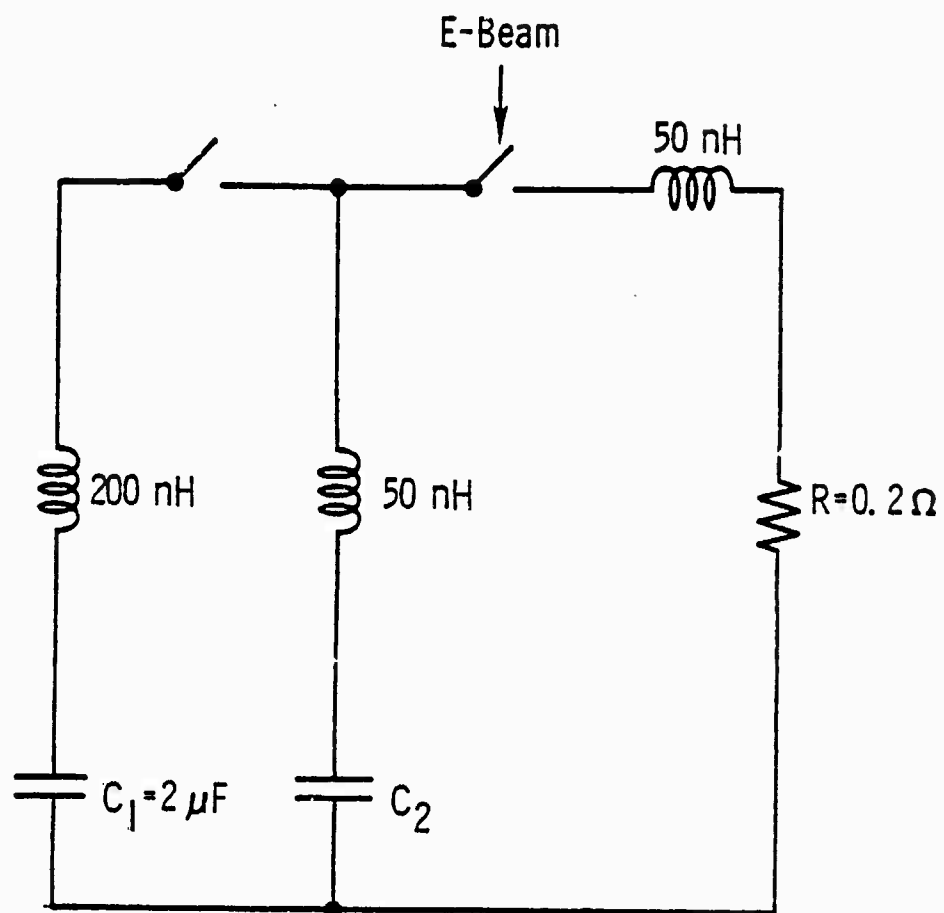
Figure 22. Pulse Charged Circuit Model

composite circuit. The circuit was analyzed simply by assuming both C_1 and C_2 charged to the same potential and switched across a fixed load simultaneously. Figure 23 shows the results for various values of C_2. The indication was that the addition of C_2 greatly improved the circuit risetime and that the value of C_2 should be as large as possible. Physical constraints imposed by the plenum geometry limited C_2 to $0.7\,\mu F$.

Electrical and Mechanical Arrangement. The discharge circuit design was guided primarily by the need for low inductance and secondarily by the requirement for reliability and versatility. Therefore, the basic layout called for stripline capacitive storage, low inductance switching techniques and multiple current feedthroughs. Additionally, the design required that the circuit components be kept in close proximity, therefore, the entire circuit was submerged in insulating oil. The relative arrangement of the circuit components is shown in Figure 24.

The capacitor bank C_1 was composed of twenty parallel capacitors in five rows connected by metal sheets in a stripline configuration. The row closest to the main switch contained four capacitors, two each of 0.015 and $0.15\,\mu F$ capacitance and the remaining pieces were each $0.25\,\mu F$. The intent was to minimize inductance between the smallest capacitances and the load and possibly add an inductor to the remaining bank, to slow up that portion of the circuit and thus keep the voltage from drooping, in the spirit of the Chebyshev circuit described above. However, under operation it was found that significant voltage droop was desirable in order to keep the discharge from arcing, therefore this modification was not attempted.

The switching circuitry was required to meet several criteria: jitter after application of the trigger pulse was to be under 20 ns, reliable switching was to be provided for initial voltages from 20-100 kV and total currents of

46
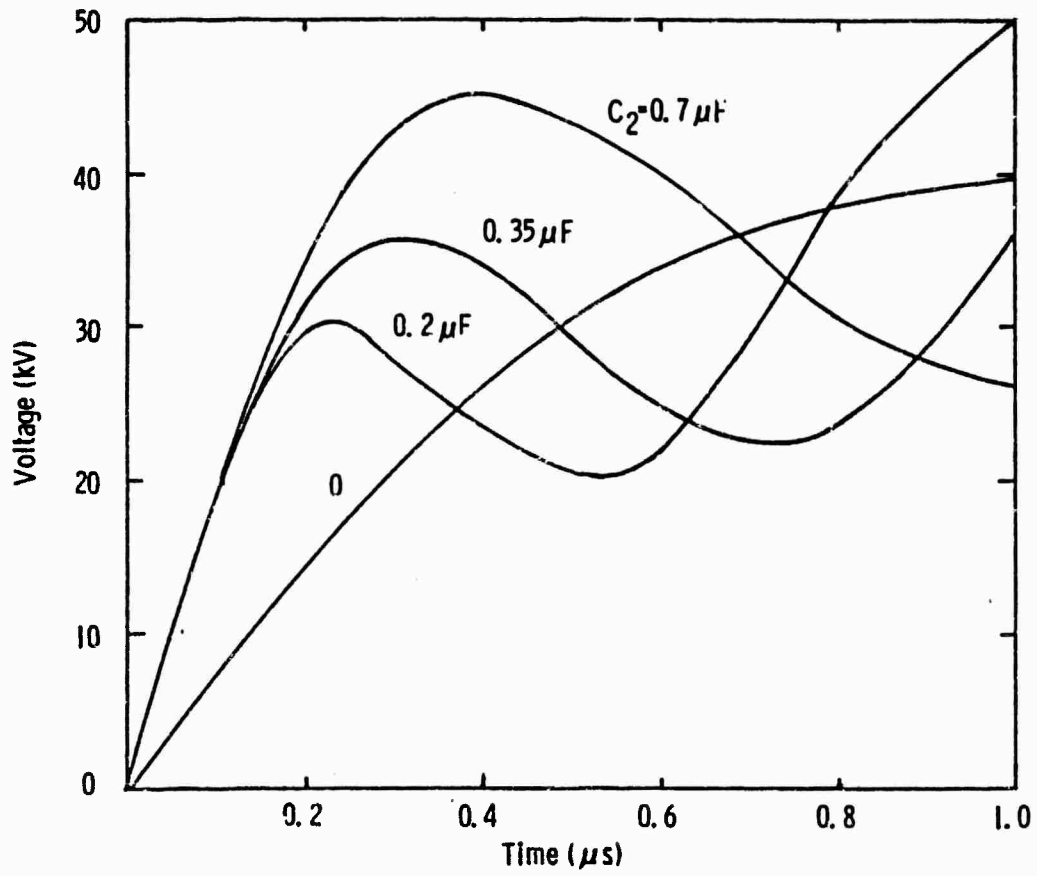
Figure 23. Pulse Charged Circuit Response

47
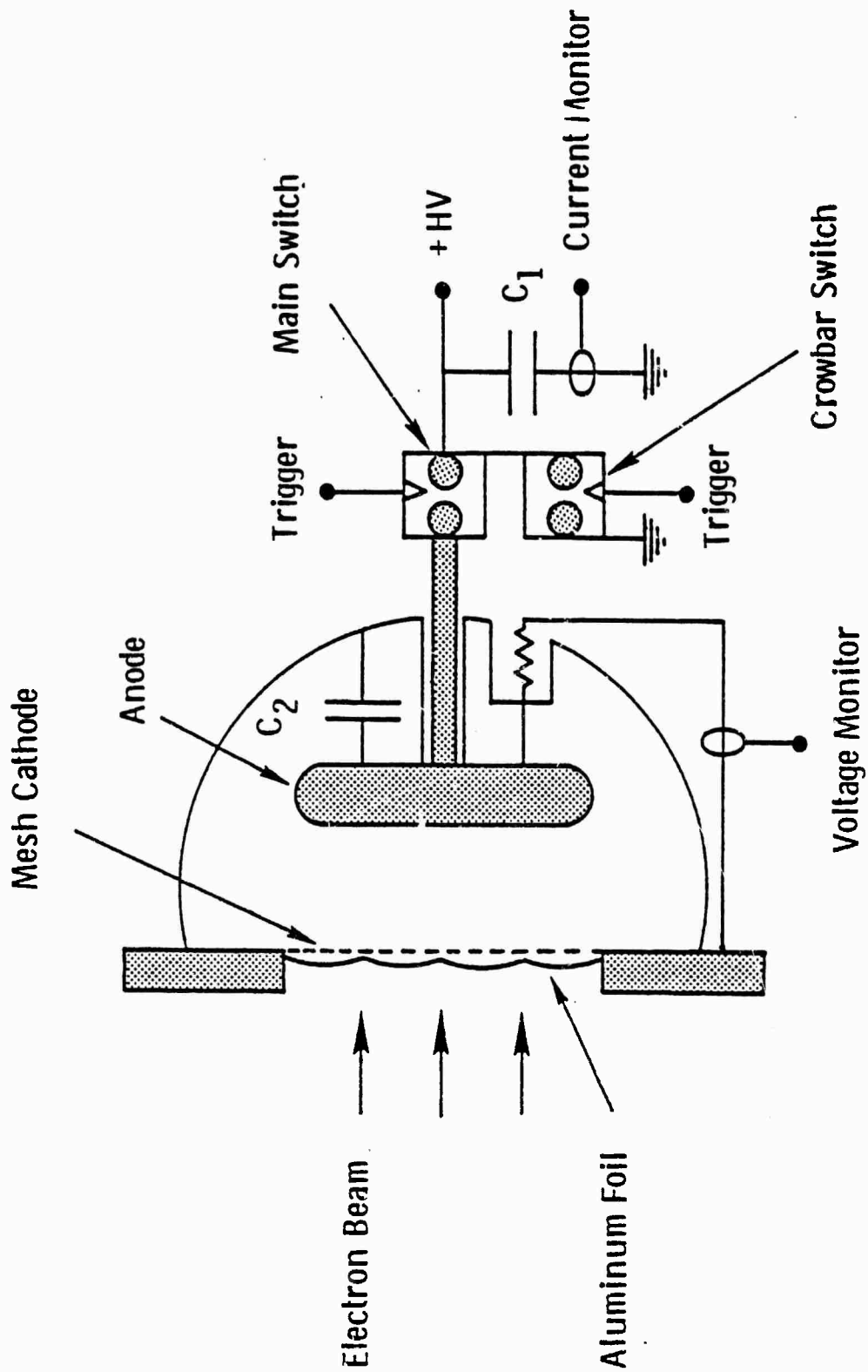
Figure 24. Discharge Circuit Arrangement

100 kA, and switch inductance was limited to 20 nH. In order to meet these specifications, the most reasonable approach was a rail gap composed of two continuous electrodes. Identical geometries were used for both the main and crowbar switches. The other alternative of individual spark gaps in parallel with transit time isolation was considered far less versatile and more difficult to accomodate physically.

Commercially available trigger generators and rail gaps, supplied by the Maxwell Laboratories were used[38]. The rail gaps were constructed in a 30 cm long three electrode geometry with a sharp-edged continuous trigger electrode placed at the 1/3-2/3 point between two cylindrical main electrodes. Two electrode spacings were required corresponding to the voltage ranges 20-50 kV and 50-100 kV, and the gaps operated in a 1/5.7 mixture of SF_6 in Argon at pressures from 20-60 psig. The trigger generators produced a 60 kV peak voltage pulse at a differential risetime of 10 kV/ns and were sufficient to cause the formation of multiple current channels ($\gtrsim 6$) over the full electrode extent for the entire voltage range. The trigger pulses were capacitively coupled into each of the resistively biased trigger electrodes. In addition, an isolating spark gap and capacitive bias in the crowbar trigger input guaranteed isolation and reliable switch initiation after significant voltage droop late in the pulse. It was found that with this arrangement, the crowbar switch would reliably hold off 100 kV at the beginning of a pulse and reliably trigger after the voltage had drooped to 30 kV, providing for a wide margin of operation at other voltages as well. Jitter for both the main and crowbar switches was measured at under 20 ns over the parameter ranges indicated above.

As outlined in the section dealing with plenum design, energy from the capacitive storage bank was transmitted to the discharge electrode via four

---

[38] Maxwell Laboratories, San Diego, California.

49

high voltage feedthroughs. Briefly, the feedthrough length was 60 cm and coaxial over about 20 cm with the remainder open to either the high pressure laser gases or insulating oil.

Various peripheral circuit elements were added for convenience. A 10 ohm Ammonium Chloride liquid resistor was connected at the output of the main switch to ground in order to provide periodic calibration of the voltage and current monitors and voltage bleed-off in the event of false triggering without electron beam operation. A mechanical crowbar was also attached at the same circuit point to prevent premature voltage application to the discharge electrode.

Basic circuit parameters were measured with a voltage probe attached directly to the discharge electrode and current monitor in the ground leg of the capacitor bank. Both monitors were designed to provide high level signals without direct contact, thereby eliminating sources for interference. The voltage probe consisted of a 500 ohm fixed resistor immersed in insulating oil within a teflon cylinder. The cylinder was fit inside the plenum and the resistor attached through a conducting cylinder end cap to the discharge electrode. The opposite end of the resistor, likewise connected to an external cylinder end cap, was connected to ground through a toroidal Pearson[33] current probe with a risetime of 20 ns. Since the Pearson probe calibration was 1V/A, signal levels were on the order of 50-100 V. Absolute calibration and frequency response were verified by parallel measurement with a Tektronix voltage probe and the system operating at reduced voltage.

The current monitor, provided by Physics International[39], was basically a Rogowski coil wound on a line 1/2 M long and placed within a notch in the conducting sheet from the capacitor terminal to ground, thus providing for

----

[39] Physics International, San Diego, California.

50

a low inductance connection. The linear current probe responded to the derivative of magnetic field and required an integrator to display current versus time. The system had a risetime of 10 ns with an integrator of time constant 20 μs (time to droop 10%). Calibration of the system was checked with a reduced capacitor bank and the output measured with a Pearson probe through a fixed dummy load resistor.

Performance. The entire discharge supply was tested with a 1 ohm NH_4Cl liquid resistor as a dummy load. In order to determine the inductance under actual operating conditions, the load was formed from four parallel legs 7.5 cm in diameter by 30 cm long, and returned to ground with 1M wide sheets to simulate the plenum walls. Typical voltage and current waveforms are shown in Figure 25. In Figure 25a, the trace starting at the upper left and going negative is total current measured by the linear probe, and the bottom, positive going trace is voltage applied to the dummy load as measured by the voltage monitor. In this case, bank capacitance was 2.33 μF with an initial charge voltage of 50 kV, and the crowbar was set to actuate 3 μs after pulse initiation. The crowbar action is clearly apparent at the point where the total current begins to rise steeply and load voltage begins to fall abruptly. With the traces extended in time as in Figure 25b, an indication of the ringing frequency through the crowbar circuit was obtained. The crowbar inductance, calculated from the usual expression, was about 174 nH. In similar fashion, the total discharge circuit inductance was measured to be about 225 nH. Therefore, it was expected that the actual discharge with impedance less than 0.2 Ω would compete favorably with the crowbar for capacitor bank energy and indeed this was the case. Discharge arcing was found to take place via a number of low inductance diffuse glows along the discharge electrode, and did not enhance possible diversion of energy through the crowbar. Therefore, although applicable to some situations, the crowbar circuit was generally not useful.

Current
9kA/div.

Voltage
10kV/div.

200 ns

Current
18 kA/div.

2 μs
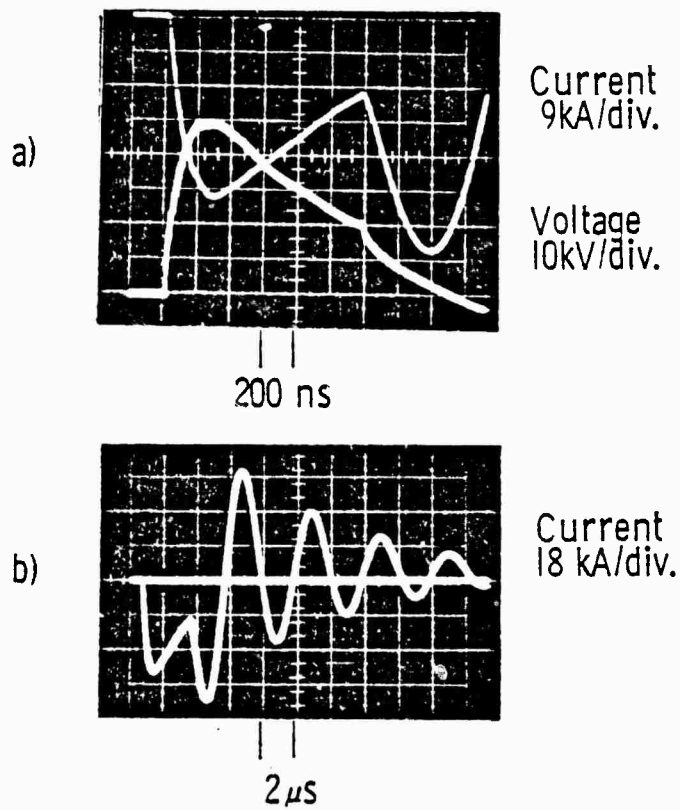
Figure 25. Capacitive Discharge Circuit Waveforms

52

Typical traces for the pulse charged circuit operating into a plasma generated by the electron beam are shown in Figure 26. In this case, $C_1 = 2.33 \, \mu F$, $C_2 = 0.7 \, \mu F$ and the initial charge voltage was 30 kV. Figure 26a shows the electron gun voltage which approximates beam current also, and Figure b shows the corresponding voltage (upper trace) and current (lower trace). The discharge electrode voltage is characterized by a steeply rising leading edge as capacitor C_2, initially at ground potential, begins to charge. Likewise, the current waveform indicates this charging cycle over the first 600 ns. Abruptly at 600 ns into the pulse charge, the electron beam current is sufficient to cause a drastic drop in the discharge impedance from infinity to about 0.5 ohm at which point the discharge voltage drops to its operating point, at 10 kV. After this point, the current probe, which measures total current in the ground leg of the main capacitive storage, does not sense true discharge current supplied by both C_2 and C_1. Discharge voltage, on the other hand, rises then falls as the main bank is depleted. Finally, at termination of the electron gun pulse, the discharge impedance rises and this is indicated in the voltage trace as a slight peak at $1.4 \, \mu s$.

2.4 <u>Laser Diagnostics and Optics.</u> The laser output beam was diagnosed in its important aspects through a variety of techniques. Total beam energy was measured calorimetrically, and two types of calorimeter were tested in order to provide a consistency check. The beam temporal behavior was monitored by a fast response photodiode with ultraviolet filters at the input to shield against extraneous flourescence. Finally, approximate but effective beam profile measurements were obtained through beam burn patterns on unexposed and developed polaroid film. These techniques proved highly consistent and reliable.

The laser optics involved state of the art technology to produce high damage threshold, low absorptance reflectors. Since periodic optical damage was caused by the combined effects of intense laser radiation, F_2 attack and

53

a)   70 kV/div.

b)   Voltage
2. 5kV/div.

Current
9kA/div.

200 ns
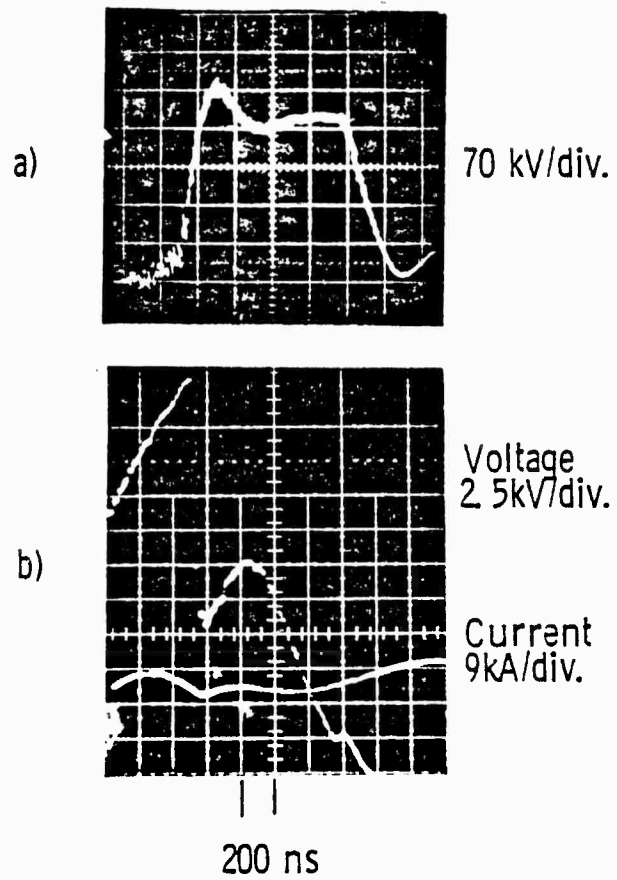
Figure 26.   Pulse Charged Circuit Waveforms

x-ray radiation, optical quality was continually monitored by a simple, 2500 Å reflectometer. In order to reduce costs incurred as a result of large area optic damage, a set of small area optics was used in the initial parameterization studies. As a result of these precautions and careful evaluation of various vendors, performance of the optics was entirely satisfactory.

Electronics. Design of the electronics arrangement was guided primarily by the need to eliminate emi from both the triggering circuits and diagnostic electronics. Primary shielding of the diagnostic electronics was provided by a solid wall shielded room with 100 db attenuation at 100 MHz. All of the oscilloscopes, photodiode bias supplies and low level delay trigger circuitry were placed in this enclosure. The various diagnostic elements themselves were located at the appropriate positions external to the shielded room and connected to it through grounded, solid conduit and shielded cable. The generation of false trigger signals due to emi in the various trigger generators was a major concern. Therefore, an effort was made to maintain high level signals at the components in the emi environment and to maintain electrical isolation of the trigger systems. These efforts proved highly successful, since false triggering was not experienced and noise levels in the shielded room were kept to approximately two oscilloscope trace widths.

Signals were recorded on 100 MHs bandwidth Tektronix oscilloscopes, and common external triggering was provided by a synchronizing pulse from the electron gun trigger generator. Coincidence of the various oscilloscope traces was within 20 ns and this was considered adequate at the 200 ns/div writing speeds used.

Diagnostics. All the laser diagnostics were arranged on a massive optical table as shown in Figure 27. The laser beam at full power was transported first to a large uncoated beam splitter which diverted 10% of the power into the diagnostic setup and allowed the balance to impinge on the burn pattern polaroid film. The low level beam was then partially focused by an uncoated, 1 M focal length lens onto the calorimeter, either a Scientech #364 or Gentec #ED 500. Again, 10% of the beam entering the calorimeter was diverted into a photodiode, ITT #4000(S5). The 10 cm diameter aperture of the Scientech calorimeter provided for complete capture of the partially focused beam; and surface absorptance at 2500 Å was 94%. The diode was operated at a bias of 2.5 kV and sufficient attenuation was used to keep the current well below saturation. In the absence of lasing or with the laser beam blocked from entering the photodiode, no signal was detected, indicating that neither fluorescence nor extraneous signals contributed to the observations. All of the beam diagnostic optics were made of high purity quartz with absorption less than 0.1% in the ultraviolet region for wavelengths greater than 2300 Å.

The beam splitting and focusing arrangement was calibrated by operating the laser at greatly reduced power and allowing the full energy to enter the calorimeters directly. Additionally, the calorimeters were found to give identical results per their stated calibrations under the same output conditions as indicated by the photodiode.

Optics. The laser optical system was formed from three geometrically distinct sets of optics. (1) Small diameter optics for the initial laser parameterization studies. These were 7.6 cm in diameter allowing for a clear aperture of 25 cm^2; (2) Large area rectangular optics for full scale extraction with the shortest possible optical cavity length of 1.2 M. These provided for a clear aperture of 9 x 14 cm^2 although partially obscured by the gun foil support as described in that section; (3) Large area circular
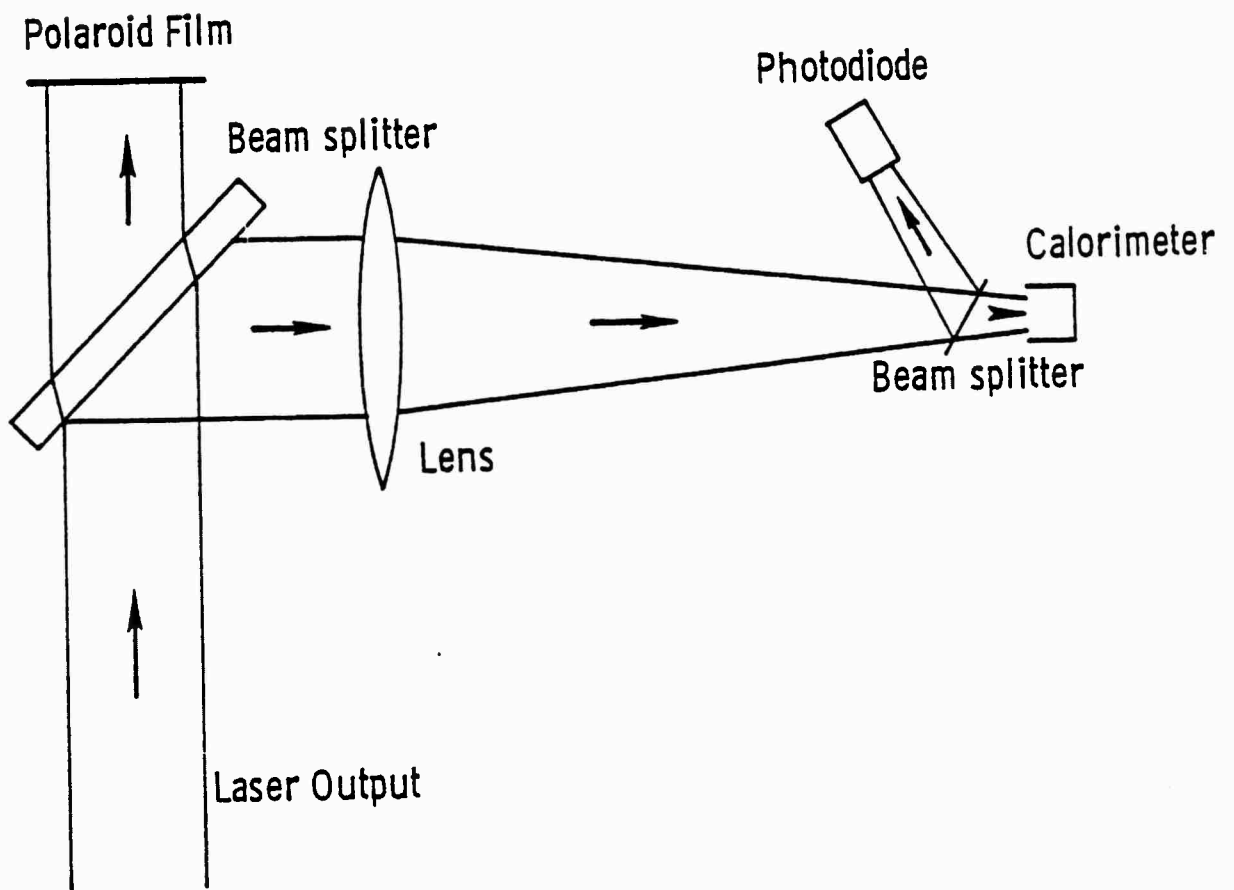
Figure 27. Laser Diagnostic Arrangement

optics for full scale extraction at the largest aperture possible but with an excessive optical cavity length of 1.5 M. Total optic diameter was 28 cm and the extraction area was sufficient to sample the full 20 liter gain volume. In all cases, the optical components were formed from high purity quartz with multi-layer dielectric coatings of MgF_2 and ThF. In some cases, anti-reflection coated windows of the same materials[4] were used, but the usual arrangement was with reflectors only at normal incidence. The mirror surfaces were either flat or possessed a 10 M radius of curvature to provide for slightly stable optical resonators. It was found that output energy and temporal behavior did not change with either flat/flat or flat/radius resonators and since beam divergence was not an important issue, both types of resonator were used interchangeably. The outward force of the high pressure gas induced added curvature to the larger area optics producing radii of curvature estimated at 20 M, and this effect may have contributed to the insensitivity of the output on resonator design.

The mirror surfaces were susceptible to attack by F_2 and changed character through extended use. As a result it was considered imperative that reflectivities be checked periodically, approximately every 100 shots. Since the large size of the mirrors precluded the use of commercially available instruments, a simple spot-check (2500 $\pm$ 50 Å) reflectometer was set up as shown in Figure 28. The intensities of the sample and reference beams were obtained by alternately blocking them. The reflectivity of the test piece was then given by (1-R)r/R, where R is reflectivity of the partial reflector and r is the ratio of sample beam to reference beam intensities. The use of an aperture over the ultraviolet source allowed spatial scan of the optic under test. Calibration tests with small diameter optics, which were checked in commercial instruments, indicated accuracies of $\pm$ 5% in reflectivity.

Alignment of the laser resonator under operating conditions was performed with a spatially filtered and collimated He-Ne laser beam. The reflections from
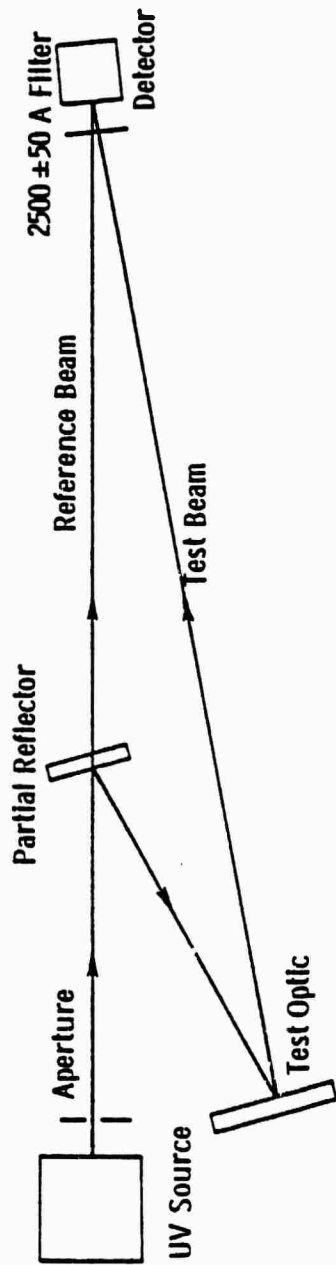
Figure 28. Reflectometer Setup

the laser mirror interior surfaces were propagated over approximately
60 M with resultant spot diameters of about 0.5 cm. Alignment accuracy was
estimated at about half a spot diameter, or 8 sec of arc. This accuracy was
considered to be well within acceptable limits since degradation of the laser
output required resonator misalignment of at least 30 sec of arc.

3. LASER KINETIC ANALYSIS AND MODELING

In order to optimize the performance of the KrF laser and to understand
its scaling to high power and high volume, it is necessary to understand the
kinetic and pumping processes which are responsible for the formation and
quenching of the excited species. In addition, it is necessary to analyze
discharge stability and effects of nonuniformity. The details of an extensive
analytical model and comparisons of its predictions with experimental data
from the large scale-up device discussed above will be described.

The theoretical model for an electrically excited laser requires a
coupled analysis which includes electron kinetics, molecular kinetics,
external driving circuit, and optical radiative extraction. The components of
such an analysis, labelled with brief descriptive remarks, are summarized
in Figure 29. A comprehensive computer code, which has been developed
to implement this coupled analysis for a broad class of electrically excited
laser systems, will be described below.[*] The molecular kinetics are
described by the master equation for the population densities of all the atomic
and molecular species present in the electrically excited gas mixture, in-
cluding electrons, ions, neutrals, excited states, molecules, excimers, etc.
The electron kinetics are described by the Boltzmann transport equation for
the electron energy distribution function $f(u)$, from which all plasma parameters,
secondary electron excitation rates, power partitioning, and discharge
efficiency can be obtained. The formulation of the Boltzmann equation
includes elastic and inelastic electron-neutral collisions, momentum

---

[*]This analysis is formulated for a spatially homogeneous medium, with a
simplified model of the optical resonator, which is assumed to be formed by
two plane parallel mirrors.

● MOLECULAR KINETICS

Master Equation for population densities of all atomic and molecular species (electrons, ions, neutrals, excited states, excimers, etc.).

● ELECTRON KINETICS

Boltzmann transport equation for the electron energy distribution to determine plasma parameters, electrical excitation rates, power partitioning, and discharge efficiency.

● CIRCUIT ANALYSIS

External circuit equations to describe the electrical power loading in a low impedance gas discharge, whose conductivity is function of t.

● OPTICAL EXTRACTION

Oscillator analysis, formulated in terms of intracavity photon density, with transient build-up of laser mode from spontaneous emission and subsequent relaxation to quasi-steady condition with gain at threshold.

Figure 29.   Coupled Laser Kinetics Analysis

61

transfer with recoil, electron-electron scattering, and properly incorporates superelastic collisions from excited species. External circuit equations are required to correctly describe the electrical power loading from an RLC driving circuit into a low impedance gas discharge whose conductivity is a function of time. Finally, radiative extraction is formulated in terms of the photon density in the cavity, and includes a source term from spontaneous emission, amplification from stimulated emission, and losses from output coupling and/or intracavity absorption. Details of each component of the coupled analysis will be discussed in more detail below.

3.1 Molecular Kinetics. For a given set of reactions, the master equation for the population densities of all interacting species can be constructed as shown in Figure 30. For any reaction involving species $X_1, X_2, \ldots, X_n$,

$$\mu_1 X_1 + \mu_2 X_2 + \ldots \mu_n X_n \xrightleftharpoons[k_r]{k_f} \nu_1 X_1 + \nu_2 X_2 + \ldots \nu_n X_n, \qquad (1)$$
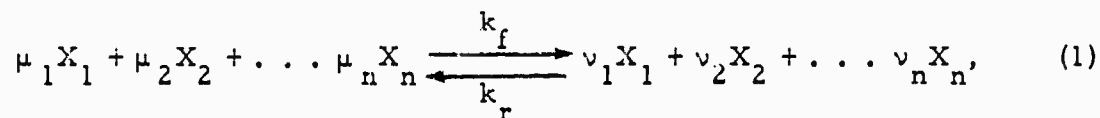
where k_f and k_r are forward and reverse rate constants, and μ_i, ν_i are (nonnegative integer) coefficients, the net rate is given by

$$R = k_f [X_1]^{\mu_1} [X_2]^{\mu_2} \ldots [X_n]^{\mu_n} - k_r [X_1]^{\nu_1} [X_2]^{\nu_2} \ldots [X_n]^{\nu_n} \qquad (2)$$

where $[X_i]$ is the population density (cm^{-3}) of the ith species X_i. The contribution that such a reaction makes to the production (or loss) of the ith species is given by

$$d/dt [X_i] = (\nu_i - \mu_i) R \qquad (3)$$

Thus, for an arbitrary reaction scheme containing several collision processes (labeled by α), the complete master equation becomes

Species i: X_1, X_2, X_3, ... X_i, ... X_n

Reactions a:

$$\mu_1(a) X_1 + \mu_2(a) X_2 + \dots + \mu_i(a) X_i + \dots$$

$$\overset{k_f}{\underset{k_r}{\rightleftharpoons}} \quad \nu_1(a) X_1 + \nu_2(a) X_2 + \dots + \nu_i(a) X_i + \dots$$
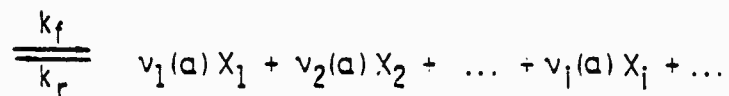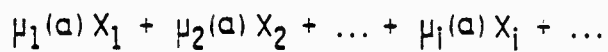
Rate:

$$R(a) = k_f(a)[X_1]^{\mu_1(a)}[X_2]^{\mu_2(a)} \cdots [X_i]^{\mu_i(a)} \cdots$$
$$- k_r(a)[X_1]^{\nu_1(a)}[X_2]^{\nu_2(a)} \cdots [X_i]^{\nu_i(a)} \cdots$$

Molecular Kinetics Master Equation:

$$\frac{d[X_i]}{dt} = \sum_a R(a)[\nu_i(a) - \mu_i(a)]$$

Figure 30.   Molecular Kinetics

$$d/dt \, [X_i] = \sum_\alpha \, [\nu_i(\alpha) - \mu_1(\alpha)] \, R(\alpha) \qquad (4)$$

It is impractical to construct new computer codes for the analysis of each new kinetic reaction scheme. The straightforward approach to write the subroutines which define the molecular kinetics for a complicated reaction scheme is, in general, a difficult and time-consuming task, and the resulting computer program would have little flexibility for analysis of any system except those in a very limited class. (For example, there are currently about 80 reactions considered important for analysis of the KrF laser.) Furthermore, as understanding of the reaction scheme evolves, addition of new reactions (or deletion of old ones) may be continually required, in addition to simple modification of rate constants for the reactions retained. Such a code would itself have to be revised in a continuing manner, rather than merely executed with revised values for the rate constants.

Therefore, in order to have a powerful analytical capability which is applicable to a broad class of problems, a generalized computer code which itself synthesizes a coupled analysis (as described in Figure 29) has been developed. This code automatically generates its own subroutines for analysis of the molecular kinetics by translating symbolic reactions into computer-coded equations. Thus, for the most complicated reaction scheme containing an arbitrary number of kinetic collision processes and interacting species, it is possible to construct the complete computer code required with virtually no effort. In order to generate the coupled analysis for any reaction scheme, all that is required is to provide an input deck, arbitrarily long, consisting of pairs of cards, the first containing a reaction, followed by a second containing forward and reverse rate constants and a reference. The syntax for the reactions is very flexible, with a free format that specifies the reaction just as it would normally be written. The content of each reaction is analyzed, and the appearance of each new species is recognized and its

name stored. The syntax of each reaction is subjected to numerous tests to detect errors. If the reaction is determined to be acceptable, it is translated into appropriate expressions in the generation of synthesized subroutines. Otherwise, diagnostic comments are produced. Program generation and execution are protected by automatic exit (by input request) if specified error conditions are encountered.

Figure 31 presents a schematic flow diagram of the present approach. The rate constants initially assumed in the generation of the program can be changed in the subsequent execution, if desired. The main purpose of the rate constants in the initial input deck is to define whether the forward and/or reverse process is to be included in the rate expressions, for if a zero rate constant is encountered for any process (other than secondary electron collisions), no translation of the forward (or backward) term occurs in the generated subroutines. If the correct values of rate constants are known, they may be entered for once and for all in the original reaction input deck. As Figure 31 indicates, the synthesized molecular kinetics subroutines are automatically combined with the master executive program and all other required subroutines to form a completely self-contained coupled analysis based upon the specified reaction scheme. The section enclosed in the upper box in Figure 31 is thus required only when a new reaction scheme is introduced. For all subsequent calculations based on the given reaction scheme, the initial conditions, experimental parameters, rate modifications (if any), and I/O and control parameters are entered, and the complete code constructed in the upper box is executed. That is, only the lower section of Figure 31 is involved thereafter.

There are several obvious advantages to this approach. First of all, there is the simplicity of automation and the minimization of the possibility of error. For example, approximately 80 reactions are currently believed to contribute

Synthesis:

```
┌─────────────────────────────────────────────────────────────┐
│  ┌───────────────────────────────────────────────────────┐  │
│  │ READ:        Symbolic reactions                        │  │
│  │              (Initial) rate constants                  │  │
│  └───────────────────────────────────────────────────────┘  │
│                            ↓                                  │
│  ┌───────────────────────────────────────────────────────┐  │
│  │ EDIT  reaction syntax to detect errors.                │  │
│  └───────────────────────────────────────────────────────┘  │
│                            ↓                                  │
│  ┌───────────────────────────────────────────────────────┐  │
│  │ TRANSLATE symbolic reactions into computer-coded        │  │
│  │ equations.                                             │  │
│  └───────────────────────────────────────────────────────┘  │
│                            ↓                                  │
│  ┌───────────────────────────────────────────────────────┐  │
│  │ COMPILE synthesized kinetics subroutines: combine with │  │
│  │ other subroutines required for coupled analysis.       │  │
│  └───────────────────────────────────────────────────────┘  │
│                            ↓                                  │
│  ┌───────────────────────────────────────────────────────┐  │
│  │ CATALOG resulting binary file for subsequent            │  │
│  │ calculations based on the input reaction scheme.        │  │
│  └───────────────────────────────────────────────────────┘  │
└─────────────────────────────────────────────────────────────┘
                            ↓
Analysis:
┌─────────────────────────────────────────────────────────────┐
│  ┌───────────────────────────────────────────────────────┐  │
│  │ READ:        Experimental parameters,                  │  │
│  │              Initial conditions,                       │  │
│  │              Rate modifications                        │  │
│  └───────────────────────────────────────────────────────┘  │
│                            ↓                                  │
│  ┌───────────────────────────────────────────────────────┐  │
│  │ EXECUTE the complete analysis, with output as specified.│ │
│  └───────────────────────────────────────────────────────┘  │
└─────────────────────────────────────────────────────────────┘
```

Figure 31. Generalized Synthesis Laser Kinetics Code

to the KrF reaction kinetics, and to write the subroutines for such a complicated system would not be simple. Secondly, the program diagnoses error conditions in the reaction syntax which may not have been noticeable or which may have been overlooked. For example, duplicate reactions are detected (even when written backwards), charge particle and heavy particle conservation is insured, detail balance relations for binary collision processes are enforced, and miscellaneous other error conditions are detected. Secondary electron collision processes are recognized and properly coupled to the electron kinetics analysis, except for the case with no discharge, in which case their rate constants can be defined by input. Finally, the subroutines are constructed in such a way that null operations are completely eliminated (if no rate constant is provided for the forward or reverse process, no translation of the corresponding term occurs), and in such a way as to optimize execution efficiency (repetitious or unnecessary multiplications are minimized).

It is usually the case that the rate constants involved in molecular kinetic reaction schemes can vary over several orders of magnitude, and therefore, the resulting master equations often become a "stiff" system of differential equations. Therefore, the approach which has been taken is to employ a multistep integration technique developed by Gear[40] for solution of such equations. This method automatically adjusts the integration step size as the solution proceeds, in such a way that required accuracy conditions are maintained. The Gear method requires subroutines not only for the rates of change of the population densities, dn_i/dt, but also for the Jacobian, $\delta \dot{n}_i/\delta n_j$, as a function of time. Because numerical evaluation of the Jacobian is not always satisfactory, it is necessary to generate both such subroutines symbolically in the synthesis section of the program, where the reaction

[40] C. William Gear, Numerical Initial Value Problems in Ordinary Differential Equations, Prentice-Hall, Englewood Cliffs, N.J. (1971). (Cf. pp. 155-167).

67

scheme is translated into computer-coded equations.

The entry of control parameters, experimental parameters, revised rate
constants, initial conditions, output requests, etc., is quite flexible,
and permits the code to be executed for a variety of situations of interest.
In the case of pure e-beam excitation, rate constants for secondary electron
processes (which are normally coupled to the Boltzmann analysis) default
automatically to zero, but can be specified by input, if desired. (This is
useful for electron recombination or attachment processes, for example.)
This makes it possible to use the same general code for both discharge and
e-beam excitation conditions. The integration of the coupled set of equations
over the total specified pulse length is carried out with the Gear technique
which automatically adjusts its step size. However, the total pulse length
is divided into 50 subintervals, at which times the electron kinetics are
updated, and a variety of output options can be specified.

3.2 Radiative Extraction. Basic features of the radiation analysis are
summarized in Figure 32. It is convenient to be able to treat stimulated
emission processes as well as absorption of the laser radiation by species in
the active medium, in a manner parallel to that for kinetic collision reactions.
Therefore, the equation for radiative extraction is formulated in terms of
the photon density in the cavity ($n_{ph} = I/ch\nu$), and includes a source term
from spontaneous emission, amplification from stimulated emission, and
losses from output coupling and/or intracavity absorption:

$$\dot{n}_{ph} = (n_{KrF}(t)/\tau_{sp}) \; (\Omega/4\pi) + (L_g/L_c)c \; [\alpha \; (t) - \alpha_{th}] \; n_{ph}. \tag{5}$$

L_g and L_c are the lengths of the gain medium and optical cavity, $\alpha_{th} =$
$[\gamma + 1/2 \; \ln(1/R)]/L_g$ is the threshold loss coefficient expressed in terms of
the intracavity loss per pass γ and the output coupling reflectivity R, $(\Omega/4\pi)$

68

- Spatially uniform intracavity optical fields.

- Plane parallel optical resonator (100%, R), separation L_c.

- Spatially uniform gain medium of length L_g.

- Distributed output coupling and loss (Y) coefficients.

- Cavity threshhold gain coefficient:

$$a_{th} = [Y + (1/2) \ln(1/R)]/L_g$$

- Buildup of optical fields:

    Spontaneous emission in solid angle Ω defined by output coupling aperture and resonator length: A/L_c^2.

    Amplification from stimulated emission, offset by the intracavity absorption and output coupling losses.

- Formulation in terms of intracavity photon density:

$$n_{ph} = I/ch\nu$$

$$dn_{ph}(t)/dt = (L_g/L_c)c[a(t) - a_{th}] n_{ph}(t) + \frac{N^*}{\tau} \frac{\Omega}{4\pi}$$

- Cavity buildup time: $t_c = L_c/L_g a_{th} c$

Figure 32 Optical Extraction

is the fractional part of the total spontaneous emission which builds up the laser mode (taken to be the solid angle Ω subtended by the output coupling mirror viewed from the opposite end of the cavity), and $\alpha(t)$ is the instantaneous net gain coefficient in the medium (i.e., gain offset by absorption),

$$\alpha(t) = n_{KrF}(t) \, \sigma_{stim} - \sum_A n_A(t) \, \sigma_{abs}(A), \qquad (6)$$

where the sum is over all absorbing species A in the medium. This approach allows the radiation intensity to be described for situations where pumping and kinetic times are comparable to the cavity decay time, $t_c = (L_c / L_g \alpha_{th} c)$. For such situations, gain relaxation effects can be observed in which the net gain initially overshoots the cavity threshold and subsequently decays to the steady state gain condition $\alpha(t) = \alpha_{th}$. Under conditions of strong pumping the overshoot can be significant, resulting in an initially enhanced super-radiative extraction, since the stimulated emission from the medium occurs under conditions of high gain. This results in a sharpening of the leading edge of the optical output power, and is observed experimentally.

3.3 Electron Kinetics. The present analysis of an electrically excited laser mixture features a completely coupled description of the molecular and electron kinetics. Plasma calculations consist of numerical solution of the Boltzmann transport equation for the electron energy distribution function, from which the electron transport coefficients, elastic and inelastic collision rates, and electrical power partitioning can be obtained as a function of gas mixture, E/N, and degree of vibrational excitation. Superelastic electron collisions (i.e., reverse processes in which electrons gain energy from collisions with excited molecular species) are included in both the molecular and plasma kinetic equations. Basic features of the electron kinetics analysis are summarized in Figure 33.

- Numerical Solution of the Boltzmann Transport Equation: Electron Energy Distribution Function

- Elastic and Inelastic Processes included: Momentum transfer, Vibrational, Electronic Excitation, Ionization, Attachment, Recombination

- Electron-electron collisions (important for fractional ionization $\geq 10^{-5}$)

- Superelastic collisions included (necessary for analysis of excited gas mixtures)

- Electrical parameters (Mobility, Drift Velocity, Average Energy, Effective Temperature, Plasma Conductivity, Discharge Current Density, etc.) as a function of E/N, Gas Mixture

- Fractional Power Partitioning of Electrical Power into all elastic and inelastic mechanisms

- Forward (and reverse) electrical excitation rates $\langle v\sigma \rangle$ for all inelastic collision processes

Figure 33. Plasma Kinetics Analysis

In general, the electron energy distribution function for the gas mixtures and relatively low E/N values typical of e^--beam sustained electric discharge lasers is highly non-Maxwellian. The availability of extensive experimental data for elastic and inelastic electron cross sections as a function of energy for many gases of interest often makes it possible to implement the electron kinetics analysis by solution of the Boltzmann equation. The electron velocity distribution function $f(\vec{v})$ for a multicomponent gas at temperature T in an external electrical field $\vec{E}$ satisfies the Boltzmann transport equation,

$$\left[\frac{\partial}{\partial t} + \vec{v} \cdot \vec{\nabla}_r - \frac{e}{m} \vec{E}(\vec{r}, t) \cdot \vec{\nabla}_v \right] f(\vec{v}, \vec{r}, t) = \frac{\delta f}{\delta t} \bigg|_{coll.} \qquad (7)$$

where the right-hand side collision term includes the effects of elastic and inelastic scattering processes. Discussion of the Boltzmann transport equation can be found in work by Holstein[41], Allis[42], Shkarofsky et al[43], Frost and Phelps[44], Carleton and Megill[45], and Englehardt et al[46], [47].

[41] T. Holstein, "Energy Distribution of Electrons in High Frequency Gas Discharges", Phys. Rev. 70, 367 (1946).

[42] W. P. Allis, "Motions of Ions and Electrons", in Handbuch der Physik, Vol. XXI (Springer-Verlag, Berlin, 1956).

[43] I. P. Shkarofsky, T. W. Johnston, and M. P. Bachynski, The Particle Kinetics of Plasmas, Addison-Wesley (1966).

[44] L. S. Frost and A. V. Phelps, "Rotational Excitation and Momentum Transfer Cross Sections for Electrons in H_2 and N_2 from Transport Coefficients", Phys. Rev. 127, 1621 (1962).

[45] N. P. Carleton and L. R. Megill, "Electron Energy Distribution in Slightly Ionized Air under the Influence of Electric and Magnetic Fields", Phys. Rev. 126, 2089 (1962).

[46] A. G. Englehardt and A. V. Phelps, "Elastic and Inelastic Collision Cross Sections in Hydrogen and Deuterium from Transport Coefficients", Phys. Rev. 131, 2115 (1963).

[47] A. G. Englehardt, A. V. Phelps, and C. G. Risk, "Determination of Momentum Transfer and Inelastic Cross Sections for Electrons in Nitrogen Using Transport Coefficients", Phys. Rev. A135, 1566 (1964).

Various approximations and techniques for numerical solution of the equation and its application to electric discharge gas lasers have been reported by Nighan et al[48], Rockwood[49], Hancock et al[50], Elliott et al[51], Morgan and Fisher[52], Lowke et al[53], and others.

At the gas densities of interest for laser operation, elastic and inelastic electron-molecule collision frequencies are so high, relative to molecular kinetic processes, that the electron distribution is usually adjusted instantaneously on the time scales over which the molecular levels are evolving. Furthermore, since elastic collision frequencies are typically greater than inelastic, the electron distribution can be assumed to have attained a quasi-steady state even on the time scales of inelastic collision processes. It follows, therefore, that the first term of (7) containing the time derivative can be discarded if the electric field is assumed to be dc or slowly varying. For a spatially uniform field, it is similarly possible to neglect the second term, since the mean free path (which is related to the elastic collision cross

[48] W. L. Nighan, "Electron Energy Distributions and Collision Rates in Electrically Excited N_2, CO, and CO_2", Phys. Rev. 2A, 1989 (1970).

[49] S. D. Rockwood, "Elastic and Inelastic Cross Sections for Electron-Hg Scattering from Hg Transport Data", Phys. Rev. A8, 2348 (1973).

[50] J. H. Hancock, R. C. Jones, and C. B. Mills, "Numerical Solution of the Boltzmann Equation for Energy Distributions of Electrons with Inelastic Scattering on Molecules", Los Alamos Rept. LA-4832, May 1972.

[51] C. J. Elliott, O. P. Judd, A. M. Lockett, and S. D. Rockwood, "Electron Transport Coefficients and Vibrational Excitation Rates for Electrically Excited CO_2 Gas Lasers", Los Alamos Informal Rept. LA-5562-MS, April 1974.

[52] W. L. Morgan and E. R. Fisher, "Calculations on the Electron Energy Distribution in a Molecular Laser Plasma", Research Institute for Eng. Sciences, Wayne State University, Report RIES 74-56, August 1974.

[53] J. J. Lowke, A. V. Phelps, and B. W. Irwin, "Predicted Electron Transport Coefficients and Operating Characteristics of CO_2-N_2-He Laser Mixtures", J. Appl. Phys. 44, 4664 (1973).

section and molecular density) is typically small compared to the discharge dimensions. The Boltzmann equation (7) then becomes

$$- (e/m) \vec{E} \cdot \vec{\nabla}_v f(\vec{v}) = \delta f/\delta t \Big|_{coll} , \qquad (8)$$

and the usual approach for solving this equation begins with an expansion of $f(\vec{v})$ into Legendre polynomials,

$$f(\vec{v}) = f_o(v) + (\vec{v}/v) \cdot \vec{f}_1(v) + (3\vec{vv}/v^2 - \tilde{1}): \tilde{f}_2(v) + \ldots \qquad (9)$$

($\tilde{1}$ and $\tilde{f}_2$ represent dyadic quantities). Usually, f can be approximated using only the first two terms. Physically, the justification of a two-term approximation is related to assumptions about the degree of anisotropy to be expected for the velocity distribution. If the electric field is small enough that the directed speed of the electrons, as measured by their drift velocity, is much less than their random thermal velocities, the small first-order perturbation $\hat{v} \cdot \vec{f}_1$ from an isotropic distribution f_o should be a good approximation. For high values of E/N characteristic of self-sustaining discharges and for certain gases, it has been speculated[54] that the f_2 term may be comparable to the f_1 term, although no analysis has included these higher order terms. Retention of more than the first two terms requires knowledge of angular (differential scattering) cross section data, which is not generally available. Typical experimental data gives only integrated cross sections as a function of the electron energy. Some of the available data in the literature has been determined indirectly by fitting measured transport coefficients to synthetic cross sections using a numerical Boltzmann analysis based on the two-term expansion of $f(\vec{v})$. Thus, consistent use of such data requires that the electron kinetics calculations should be based on

---

[54] W. F. Bailey, Paper DD5 presented at the Twenty-Fifth Gaseous Electronics Conf., London, Ontario, Canada, October 1972.

74

the two-term approximation. For values of E/N typical of e⁻-beam sustained discharges, this approach is justified, and is numerically much simpler than would be the case if angular calculations were required.

In the expansion (9), $f_o(v)$, $\vec{f}_1(v)$, $\vec{f}_2$, ... are functions only of the magnitude v, since the angular dependence occurs in the spherical harmonic coefficients. It can easily be shown that

$$\vec{\nabla}_v f = \frac{1}{3v^2} \frac{d}{dv} (v^2 \vec{f}_1) + \frac{df_o}{dv} \hat{v} + \frac{v}{3} \frac{d}{dv} (v\vec{f}_1) \cdot (3 \hat{v}\hat{v} - \widetilde{I}) + \ldots \quad (10)$$

where $\vec{\nabla}_v f$ has been separated explicitly into terms which have $\ell = 0, 1$, and 2 symmetry, respectively. If (10) is substituted into (8), and separated into scalar and vector parts (which corresponds to multiplying by 1 or v and integrating over the spherical solid angles Ω_v), the following equations result:

$$-\frac{e\vec{E}}{3mv^2} \cdot \frac{d}{dv} (v^2 \vec{f}_1) = \frac{\delta f_o}{\delta t} \bigg|_{coll} \quad (11)$$

$$-\frac{e\vec{E}}{m} \cdot \frac{df_o}{dv} = \frac{\delta \vec{f}_1}{\delta t} \bigg|_{coll} \quad (12)$$

The most important physical mechanism for reducing the asymmetry in the distribution function is electron-molecule momentum transfer collisions. The collisional rate of change of $\vec{f}_1$ can be approximated by[43]

$$-\frac{\delta \vec{f}_1}{\delta t} \bigg|_{coll} = -\sum_X \nu_m^X (v) \vec{f}_1, \quad (13)$$

where $\nu_m^X = N_X v Q_m^X (v)$ is the momentum transfer collision frequency for molecules X in terms of the population density N_X and momentum transfer

cross section Q_m^X. In terms of the electron energy $u = mv^2/2e$ (in units of eV), the equation for f_o becomes, after manipulation of (11), (12), and substitution of (13),

$$- (E^2/3) \, d/du \left[\frac{u}{\sum_X N_X Q_m^X (u)} \, df_o/du \right] \sqrt{\frac{2e}{m}} = \sqrt{u} \, \frac{\delta f_o}{\delta t} \bigg|_{coll} \qquad (14)$$

Expressions for the collision term on the right hand side have been developed by Allis[42], Shkarofsky et al[43], Frost and Phelps[44] and others for elastic momentum transfer and inelastic electron-neutral scattering processes. In addition, whenever the fractional ionization is $\gtrsim 10^{-5}$, it is often necessary[55] to include the effects of electron-electron Coulomb scattering. Rockwood[40] has shown how the Boltzmann equation may be expressed in terms of a "flux divergent" description of the electron distribution in energy space, viz.,

$$-dJ_f/du - dJ_{el}/du - dJ_{ee}/du + \sum_\alpha \left[(u + u_\alpha) \, f_o (u + u_\alpha) \, N_\alpha Q_\alpha (u + u_\alpha) - \right.$$

$$u f_o(u) N_\alpha Q_\alpha(u) + (u - u_\alpha) \, f_o(u - u_\alpha) \, N_\alpha^* Q_{-\alpha}(u - u_\alpha) -$$

$$\left. u f_o(u) N_\alpha^* Q_{-\alpha}(u) \right] = 0 \qquad (15)$$

where

$$J_f(u) = -(E^2/3) \left[\frac{u}{<N \, Q_m(u)>} \, df_o/du \right] \qquad (16)$$

$$J_{el}(u) = -\left[u^2 <(2m/M) N Q_m> (f_o + kT/e \, df_o/du) \right] \qquad (17)$$

$$J_{ee}(u) = -(2\pi/3) \frac{q^4}{e^2} n_e \ln \Lambda \left[P(u) \, df_o/du + Q(u) \, f_o(u) \right] \qquad (18)$$

$$P(u) = 2 \int_0^u dw \, w^{3/2} \, f_o(w) + 2u^{3/2} \int_u^\infty dw \, f_o(w) \qquad (19)$$

[55] W. H. Long, "Electron Kinetics in the KrF Laser", Appl. Phys. Lett 31, 391 (1977).

$$Q(u) = 3 \int_0^u dw\ w^{1/2} f_o(w) \qquad\qquad (20)$$

In the definition of J_{ee}, $q = 300\ e = 4.8 \times 10^{-10}$ esu is the electronic charge (cgs units), and $\Lambda = \ell_D/r_{min}$, where ℓ_D and r_{min} are the Debye lengths and classical distance of closest approach, defined by

$$\Lambda = \ell_D/r_{min} \qquad\qquad (21)$$

$$\ell_D = (kT_e/4\pi n_e^2)^{1/2} \qquad\qquad (22)$$

$$r_{min} = q^2/(e\bar{u}) = q^2/(1.5kT_e) \qquad\qquad (23)$$

$Q_{\pm\alpha}(u)$ are (forward and reverse) cross sections for the inelastic collision processes, labeled by α, and

$$<NQ_m(u)> = \sum_X N_X Q_m^X(u)$$

$$<(2m/M)\ NQ_m(u)> = \sum_X (2m/M_X)\ N_X Q_m^X(u). \qquad\qquad (24)$$

N_α and N_α^* are population densities of the lower and upper (excited) states, and u_α is the inelastic energy transferred during the collision. The principle of detailed balance provides relations between the cross sections for forward and reverse processes:

$$(u + u_\alpha)\ Q_\alpha\ (u + u_\alpha) = uQ_{-\alpha}(u)$$

$$\qquad\qquad (25)$$

$$(u - u_\alpha)\ Q_{-\alpha}\ (u - u_\alpha) = uQ_\alpha(u)$$

The first two terms in the sum over α in (15) correspond to collisions in which the electrons lose energy, while the last two terms (which represent the

77

superelastic processes) correspond to collisions in which excited molecular species transfer energy to the electrons. Only binary electron-molecule collisions, including, for example, vibrational excitation, electronic excitation, attachment, recombination, ionization, etc. will be considered. It should also be noted, therefore, that the collision term for process α does not always contain all four of the terms indicated in the general expression given in (15). For example, only the second term occurs for recombination or attachment, and for ionization or dissociation, only the first two terms occur. Effects of recoil in elastic energy transfer processes are included in the second term of (17), where the molecular distribution is assumed to be Maxwellian at temperature T. Effects of rotational excitation can be included in the same way as momentum transfer by making a suitable continuum approximation.

The normalization condition for $f_o(u)$ is taken to be

$$\int_0^\infty du\, u^{1/2} f_o(u) = 1 \tag{26}$$

where the factor $u^{1/2}$ originates from the density of states $v^2 dv/du$. From the solution for $f_o(u)$, all of the forward and reverse excitation rates, electrical power partitioning, and plasma parameters (drift velocity, mobility, average and characteristic energies, effective temperature, etc.) can be obtained. The important quantities required for the coupled laser analysis are the secondary electron excitation rates, given by

$$\nu_\alpha = n_e (2e/m)^{1/2} \int_0^\infty du\, u\, f_o(u)\, Q_\alpha(u) \tag{27}$$

and the electrical power balance (W/cm^3), obtained by multiplying (15) by $e(2e/m)^{1/2} u$ and integrating:

78

$$e\mu E^2 = e(2e/m)^{1/2} \left\{ \int_0^\infty du\ u^2 <(2m/M)\ NQ_m> [f_0 + (kT/e)\ df_0/du] \right.$$

$$\left. + \sum_\alpha u_\alpha \int_0^\infty du\ u\ f_0(u)\ [N_\alpha Q_\alpha(u) - N_\alpha^* Q_{-\alpha}(u)] \right\} \qquad (28)$$

where μ is the mobility. The physical significance of (28) is that the total electrical power input (on the LHS) is balanced by elastic heating from momentum transfer collisions, and by power dissipation from inelastic excitation (and de-excitation) processes. Note that there is no contribution from elastic electron-electron scattering: this mechanism merely redistributes electron energy and tends to drive the distribution toward a Maxwellian shape. Note also that, for processes such as recombination and attachment, in which electrons are lost, only the second term of the collision expression in (15) occurs, and in that case, the corresponding term for the power balance (28) must be replaced by

$$e\ (2e/m)^{1/2}\ N_\alpha \int_0^\infty du\ u^2 f_0(u)\ Q_\alpha(u)$$

Expressions for miscellaneous plasma parameters are:

$$\mu = -(1/3)\ (2e/m^{1/2} \int_0^\infty du\ (u/<NQ_m(u)>)\ df_0/du$$

$$D = (1/3)\ (2e/m)^{1/2} \int_0^\infty du\ (u/<NQ_m(u)>)\ f_0(u)$$

$$\bar{u} = \int_0^\infty du\ u^{3/2}\ f_0(u) = (3/2)\ kT_e \qquad (29)$$

$$\epsilon_k = D/\mu$$

$$v_d = \mu E$$

$$I_{sus} = n_e e\ v_d$$

79

Numerical solution of the Boltzmann equation is carried out by reducing the differential equation (15) to a finite difference equation, defined over a uniform grid of equally spaced energy values. This results in a large set (typically, $\gtrsim 500$) of coupled algebraic equations, which is solved by an iterative approach that reduces the system to a tridiagonal set of equations. The algorithm[56] which has been implemented is extremely fast, and has been constructed in such a way that execution speed is optimized when a good initial guess is available. Thus, the present approach is quite suitable to a coupled analysis in which the excited state population densities and discharge voltage change as a function of time, since the previous electron distribution always provides a good initial guess for obtaining an updated distribution. For example, with an electron grid of 500 points, 15 inelastic collision processes and electron-electron scattering, the electron distribution converges to an accuracy $\lesssim 2 \times 10^{-3}$ after ~8 iterations in ~0.7 CP sec. (Sample output is present in Figure 41, 42 and 43 in the following section.)

3.4 <u>External Driving Circuit</u>. Basic features of the equations which describe the external driving circuit are illustrated in Figure 34. A plane parallel discharge of area A, with anode and cathode separated by a distance d, is driven by an external RLC circuit with a capacitor initially charged to high voltage. The discharge is sustained by an external e^--beam with an arbitrary temporal current density. Initially, there is no voltage across the discharge because of the external circuit inductance. As the secondary electron density in the gas changes, the plasma conductivity (and hence the discharge impedance) will change. Thus, the plasma kinetics analysis is directly coupled to the circuit equations which define the instantaneous voltage (and thus, the value of E/N) across the discharge:

---

(56) W. B. Lacina, "Supersonic Continuous Wave Carbon Monoxide Laser Development, Volume I: CO Laser Kinetics Code", Northrop Report NRTC-75-25R, July 1975.
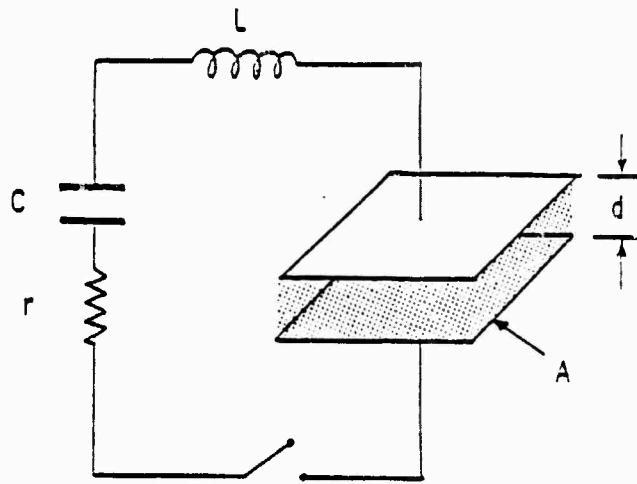
Plasma conductivity: $\sigma = n_e(t)e\mu(t)$

Plasma impedance: $R_d(t) = d/A\sigma(t)$

$$L\frac{di}{dt} + (r + R_d(t))i + \frac{q}{C} = 0$$

Figure 34. External Driving Circuit

$$L \, di/dt + (r + R_d(t)) \, i + q/C = 0, \tag{33}$$

where L = inductance, r = external resistance, C = capacitance, and i = current. The discharge impedance $R_d(t)$ is a function of time, and is given by

$$r_d(t) = d/A\sigma(t), \tag{34}$$

where

$$\sigma(t) = n_e(t) \, e \, \mu(t) \tag{35}$$

and $\mu(t)$ is the electron mobility. The electron kinetics analysis requires $(E/N)(t) = i(t) \, R_d(t)/(d/N)$.

3.5 **Typical Analytical Results.** Sample output from a typical computer run, taken from a simulation of experimental conditions to be discussed in a subsequent section, will be presented here to illustrate the features of the analysis.

The molecular kinetic processes presently included for the KrF system are summarized in Figure 35, which is a reproduction of the input data deck which defines the reaction scheme. Figure 38 is a reproduction of output summarizing details and comments about the reaction scheme; this table is generated during the synthesis of the rate subroutines as the input reaction scheme is processed, scanned for errors, and translated into computer coded equations. Figure 37 presents the results of an edit of the reaction scheme: the occurence of each species encountered in each reaction is summarized. As Figure 35 and 36 indicate, the kinetic processes for KrF include excitation of excited states and ions of Ar and Kr by secondary and high energy beam electrons, fluorine attachment, formation and quenching of several excimers, charge transfer, electron and negative ion (F^-) recombination with positive ions, miscellaneous replacement reactions, a variety of energy transfer

82

```
CARD           1         2         3         4         5         6         7         8
NO.    1234567890123456789012345678901234567890123456789012345678901234567890

-------------------------------------------------------------------------------

 1 .... NORTHROP KRF LASER KINETICS
 2 ....AR + E ~ AR* + E
 3 ....                      SCHAPER, SCHEIBNER, BEITR. AUS PLASMA PHYS. 9, 45
 4 ....KR + E ~ KR* + E
 5 ....                      SCHAPER, SCHEIBNER, BEITR. AUS PLASMA PHYS. 9, 45
 6 ....AR + E ~ AR** + E
 7 ....                      0.1 X AR* CROSS SECTION, 13.4 EV THRESH
 8 ....KR + E ~ KR** + E
 9 ....                      0.1 X AR* CROSS SECTION, 11.5 EV THRESH
10 ....AR* + E ~ AR** + E
11 ....                      60.E-16 CM2 AT 2 EV THRESHHOLD ASSUMED.
12 ....KR* + E ~ KR** + E
13 ....                      60.E-16 CM2 AT 1.6 EV THRESHHOLD ASSUMED.
14 ....AR + E ~ AR(+) + E + E
15 ....                      RAPP, ENGLANDER-GOLDEN JCP 43, 1464 (65)
16 ....KR + E ~ KR(+) + E + E
17 ....                      RAPP, ENGLANDER-GOLDEN JCP 43, 1464 (65)
18 ....AR* + E ~ AR(+) + E + E
19 ....                      7.E-16 CM2 AT 4.2 EV THRESHHOLD ASSUMED.
20 ....KR* + E ~ KR(+) + E + E
21 ....                      10.E-16 CM2 AT 4.0 EV THRESHHOLD ASSUMED.
22 ....AR** + E ~ AR(+) + E + E
23 ....                      30 E-16 CM2 AT 2.4 EV THRESHOLD.
24 ....KR** + E ~ KR(+) + E + E
25 ....                      30 E-16 CM2 AT 3.1 EV THRESHOLD.
26 ....AR2(+) + E ~ AR* + AR
27 ....                      MEHR, BIONDI (SYNTHETIC: TE**(-3/2) LAW)
28 ....KR2(+) + E ~ KR* + KR
29 ....                      OSKAM, MITTELSTADT (SYNTHETIC: TE**(-3/2) LAW)
30 ....F2 + E ~ F + F-
31 ....                      HOFLAND, AEROSPACE CORP.
32 ....AR2* + E ~ AR + AR + E
33 .... 1.00 E-07
34 ....KR2* + E ~ KR + KR + E
35 .... 1.00 E-07
36 ....AR + HE- ~ AR(+) + HE- + E
37 .... 4.34 E-18            BERGER-SELTZER: STOP = 1.7 MEVCM2/GM (300 KEV)
38 ....AR + HE- ~ AR* + HE-
39 .... 1.24 E-18 1.24 E-18  (1/3.5) X AR + HE ~ AR(*) + E + HE
40 ....KR + HE- ~ KR(+) + HE- + E

-------------------------------------------------------------------------------

       1234567890123456789012345678901234567890123456789012345678901234567890
           1         2         3         4         5         6         7         8
```

Figure 35.   Summary of Card Images for Input Data Deck

```
CARD          1         2         3         4         5         6         7         8
NO.  1234567890123456789012345678901234567890123456789012345678901234567890123456789

----------------------------------------------------------------------------------

41 ....  8.04 E-18                BERGER-SELTZER: STOP = 1.5 MEVCM2/GM (300 KEV)
42 ....KR + HE- + KR* + HE-
43 ....  2.30 E-18 2.30 E-18      (1/3.5) X KR + HE + KR(+) + E + HE
44 ....AR(+) + AR + M + AR2(+) + M
45 ....  2.00 E-31                W. F. LIU, D. C. CONWAY  JCP 62, 3070 (1975)
46 ....AR(+) + KR + M + ARKR(+) + M
47 ....    2.5E-31
48 ....KR(+) + KR + M +KR2(+) + M
49 ....  2.40 E-31                C. J. TRACY, H. J. OSKAM  JCP 65, 3387 (1976)
50 ....KR(+) + AR + M + ARKR(+) + M
51 ....    1.0E-31
52 ....AR(+) + KR + AR + KR(+)
53 ....  3.00 E-11
54 ....AR2(+) + KR + KR(+) + AR + AR
55 ....    7.5E-10                BOHME ET AL, J. CHEM. PHYS. 52, 5094 (1970)
56 ....ARKR(+) + KR + KR2(+) + AR
57 ....    3.2E-10                BOHME ET AL, J. CHEM. PHYS. 52, 5094  (1970)
58 ....AR* + AR + M + AR2* + M
59 ....  1.00 E-32                HILL, GUTCHECK, HUESTIS, ET AL, SRI REPORT, 1974.
60 ....AR* + KR + M + ARKR* + M
61 ....    1.0E-32
62 ....KR* + KR + M + KR2* + M
63 ....    5.5E-32                HUGHES LASL ASPEN 9/76
64 ....KR* + AR + M + ARKR* + M
65 ....    1.0E-32
66 ....ARKR* + KR + KR2* + AR
67 ....  1.00 E-10                SRI REPORT NO. MP 76-99, DEC., 1976
68 ....AR2(+) + F- + ARF* + AR
69 ....  5.00 E-07
70 ....AR2(+) + F- + AR2F*
71 ....  5.00 E-07
72 ....AR(+) + F- + ARF*
73 ....    1.0E-06
74 ....KR2(+) + F- + KRF* + KR
75 ....  5.00 E-07
76 ....KR2(+) + F- + KR2F*
77 ....  5.00 E-07
78 ....KR(+) + F- + KRF*
79 ....    1.0E-06
80 ....ARKR(+) + F- + KRF* + AR

----------------------------------------------------------------------------------

   1234567890123456789012345678901234567890123456789012345678901234567890123456789
          1         2         3         4         5         6         7         8
```

Figure 35 (Continued)

```
CARD          1         2         3         4         5         6         7         8
NO.   12345678901234567890123456789012345678901234567890123456789012345678901234567890

----------------------------------------------------------------------------------------

 81 .... 5.00 E-07
 82 ....ARKR(+) + F- ~ ARKRF*
 83 ... 5.00 E-07
 84 ...KR* + F2 ~ KRF* + F
 85 ... 7.20 E-10               VELAZCO, KOLTS, SETSER, JCP 65, 3469 (1976)
 86 ....AR* + F2 ~ ARF* + F
 87 ... 7.50 E-10               VELAZCO, KOLTS, SETSER, JCP 65, 3469 (1976)
 88 ....AR* + KR ~ AR + KR*
 89 .... 4.20 E-12              PIPER, SETSER, CLYNE, JCP 63, 4018 (1975)
 90 ...KRF* + AR + M ~ ARKRF* + M
 91 .... 6.00 E-32              AVCO
 92 ...KRF* + KR + M ~ KR2F* + M
 93 .... 5.00 E-31              AVCO
 94 ...ARF* + AR + M ~ AR2F* + M
 95 .... 4.00 E-31              AVCO
 96 ...ARF* + KR + M ~ ARKRF* + M
 97 .... 1.00 E-31
 98 ...AR2* + KR ~ AR + AR + KR*
 99 .... 8.00 E-11              ZAHIR (PRIV. COMMUN. TO SRI)
100 ...AR2* + AR2* ~ AR2(+) + AR + AR + E
101 ...    3.0E-10
102 ...ARF* + KR ~ KRF* + AR
103 .... 1.50 E-10              SRI REPORT NO. MP 76-99, DEC., 1976
104 ...AR2* + F ~ ARF* + AR
105 ....    3.0E-10
106 ...KR2* + F ~ KRF* + KR
107 ....    3.0E-10
108 ...AR2* + F2 ~ AR2F* + F
109 ... 2.50 E-10               SRI REPORT NO. MP 76-99, DEC., 1976
110 ...ARKR* + F2 ~ KRF* + AR + F
111 .... 6.00 E-10              SRI REPORT NO. MP 76-99, DEC., 1976
112 ...ARKR* + F2 ~ ARKRF* + F
113 ....    3.0E-10
114 ...KR2* + F2 ~ KR2F* + F
115 .... 3.00 E-10              SRI REPORT NO. MP 76-99, DEC., 1976
116 ...AR2F* + F2 ~ AR + AR + F + F2
117 .... 1.00 E-09              SRI REPORT NO. MP 76-99, DEC., 1976
118 ...ARKRF* + F2 ~ AR + KR + F + F2
119 .... 1.00 E-09              SRI REPORT NO. MP 76-99, DEC., 1976
120 ...KR2F* + F2 ~ KR + KR + F + F2

----------------------------------------------------------------------------------------

      12345678901234567890123456789012345678901234567890123456789012345678901234567890
          1         2         3         4         5         6         7         8
```

```
CARD              1         2         3         4         5         6         7         8
NO.     12345678901234567890123456789012345678901234567890123456789012345678901234567890

--------------------------------------------------------------------------------------------

121  .... 1.00 E-09              SRI REPORT NO. MP 76-99, DEC., 1976
122  ....ARKRF* + KR ~ KR2F* + AR
123  .... 1.00 E-10              SRI REPORT NO. MP 76-99, DEC., 1976
124  ....KRF* + F2 ~ KR + F + F2
125  .... 1.00 E-09              SRI REPORT NO. MP 76-99, DEC., 1976
126  ....ARF* + F2 ~ AR + F + F2
127  .... 1.00 E-09              SRI REPORT NO. MP 76-99, DEC., 1976
128  ....AR2F* + KR ~ KRF* + AR + AR
129  ....    1.0E-10
130  ....AR** + M ~ AR* + M
131  .... 1.00 E-10
132  ....KR** + M ~ KR* + M
133  .... 1.00 E-10
134  ....ARF* ~ AR + F
135  .... 3.30 E 07              SRI REPORT NO. MP 76-99, DEC., 1976
136  ....AR2* ~ AR + AR
137  .... 3.80 E 06              SRI REPORT NO. MP 76-99, DEC., 1976
138  ....ARKR* ~ AR + KR
139  ....    3.0E+06
140  ....KR2* ~ KR + KR
141  .... 3.30 E 06              SRI REPORT NO. MP 76-99, DEC., 1976
142  ....AR2F* ~ AR + AR + F
143  .... 2.00 E 08              SRI REPORT NO. MP 76-99, DEC., 1976
144  ....ARKRF* ~ AR + KR + F
145  .... 5.00 E 07              SRI REPORT NO. MP 76-99, DEC., 1976
146  ....KR2F* ~ KR + KR + F
147  .... 6.70 E 07              SRI REPORT NO. MP 76-99, DEC., 1976
148  ....KRF* ~ KR + F + HNU
149  .... 1.10 E 08              R. BURNHAM, S. S. SEARLES (SUBMITTED TO JCP)
150  ....KRF* + RAD ~ KR + F + RAD
151  .... 2.00 E-16              LASER TRANSITION: STIMULATED EMISSION X-SECTION
152  ....F2 + RAD ~ F + F
153  .... 1.50 E-20
154  ....F- + RAD ~ F + E
155  .... 5.40 E-18              A. MANDL, PHYS REV A3, 251 (1971)
156  ....KR2F* + RAD ~ AR* + KR + F
157  .... 1.00 E-99              CROSS SECTION UNKNOWN
158  ....AR2(*) + RAD ~ AR + AR(*)
159  .... 1.50 E-17              STEVENS (PARK CITY CONFERENCE)
160  ....KR2(*) + RAD ~ KR + KR(*)

--------------------------------------------------------------------------------------------

        12345678901234567890123456789012345678901234567890123456789012345678901234567890
            1         2         3         4         5         6         7         8
```

Figure 35 (continued)

SUMMARY OF INPUT: REACTIONS AND RATE CONSTANTS (SEC-1, CM3/SEC, CM6/SEC, ..., OR CM2) WITH REFERENCES

(IF A RATE CONSTANT KF OR KR FOR A BINARY ELECTRON COLLISION IS NOT EXPLICITLY SPECIFIED, IT WILL BE COMPUTED SELF CONSISTENTLY AS A FUNCTION OF E/N. GAS COMPOSITION, AND EXCITED LEVEL DENSITIES FROM A COUPLED ELECTRON ANALYSIS.)

I	REACTION(I) (IGNORED REACTIONS ARE NOT NUMBERED)	RATE CONSTANTS		RATE REFERENCES AND/OR COMMENTS
		KF(I)	KR(I)	
1	AR + E -> AR* + E	(COMPUTED)	(COMPUTED)	SCHAPER, SCHEIBNER, BEITR. AUS PLASMA PHYS. 9, 45 FORWARD RATE IS OBTAINED FROM E- KINETICS ANALYSIS REVERSE RATE IS OBTAINED FROM E- KINETICS ANALYSIS
2	KR + E -> KR* + E	(COMPUTED)	(COMPUTED)	SCHAPER, SCHEIBNER, BEITR. AUS PLASMA PHYS. 9, 45 FORWARD RATE IS OBTAINED FROM E- KINETICS ANALYSIS REVERSE RATE IS OBTAINED FROM E- KINETICS ANALYSIS
3	AR + E -> AR** + E	(COMPUTED)	(COMPUTED)	0.1 X AR* CROSS SECTION. 13.4 EV THRESH FORWARD RATE IS OBTAINED FROM E- KINETICS ANALYSIS REVERSE RATE IS OBTAINED FROM E- KINETICS ANALYSIS
4	KR + E -> KR** + E	(COMPUTED)	(COMPUTED)	0.1 X AR* CROSS SECTION. 11.5 EV THRESH FORWARD RATE IS OBTAINED FROM E- KINETICS ANALYSIS REVERSE RATE IS OBTAINED FROM E- KINETICS ANALYSIS
5	AR* + E -> AR** + E	(COMPUTED)	(COMPUTED)	60.E-16 CM2 AT 2 EV THRESHHOLD ASSUMED. FORWARD RATE IS OBTAINED FROM E- KINETICS ANALYSIS REVERSE RATE IS OBTAINED FROM E- KINETICS ANALYSIS
6	KR* + E -> KR** + E	(COMPUTED)	(COMPUTED)	60.E-16 CM2 AT 1.6 EV THRESHHOLD ASSUMED. FORWARD RATE IS OBTAINED FROM E- KINETICS ANALYSIS REVERSE RATE IS OBTAINED FROM E- KINETICS ANALYSIS
7	AR + E -> AR(+) + E + E	(COMPUTED)		RAPP, ENGLANDER-GOLDEN JCP 43, 1464 (65) FORWARD RATE IS OBTAINED FROM E- KINETICS ANALYSIS REVERSE REACTION IS IGNORED -- KR = 0.
8	KR + E -> KR(+) + E + E	(COMPUTED)		RAPP, ENGLANDER-GOLDEN JCP 43, 1464 (65) FORWARD RATE IS OBTAINED FROM E- KINETICS ANALYSIS REVERSE REACTION IS IGNORED -- KR = 0.
9	AR* + E -> AR(+) + E + E	(COMPUTED)		7.E-16 CM2 AT 4.2 EV THRESHHOLD ASSUMED. FORWARD RATE IS OBTAINED FROM E- KINETICS ANALYSIS REVERSE REACTION IS IGNORED -- KR = 0.
10	KR* + E -> KR(+) + E + E	(COMPUTED)		10.E-16 CM2 AT 4.0 EV THRESHHOLD ASSUMED. FORWARD RATE IS OBTAINED FROM E- KINETICS ANALYSIS REVERSE REACTION IS IGNORED -- KR = 0.
11	AR** + E -> AR(+) + E + E	(COMPUTED)		30 E-16 CM2 AT 2.4 EV THRESHOLD. FORWARD RATE IS OBTAINED FROM E- KINETICS ANALYSIS REVERSE REACTION IS IGNORED -- KR = 0.

GENERALIZED KINETICS SYNTHESIS CODE: DR. WILLIAM B. LACINA, NORTHROP RESEARCH AND TECHNOLOGY. DATE: 10/21/77

Figure 36. Summary of Input: Reactions and Rate Constants

87

SUMMARY OF INPUT: REACTIONS AND RATE CONSTANTS (SEC-1, CM3/SEC, CM6/SEC, ..., OR CM2) WITH REFERENCES

(IF A RATE CONSTANT KF OR KR FOR A BINARY ELECTRON COLLISION IS NOT EXPLICITLY SPECIFIED, IT WILL BE COMPUTED SELF CONSISTENTLY AS A FUNCTION OF E/N, GAS COMPOSITION, AND EXCITED LEVEL DENSITIES FROM A COUPLED ELECTRON ANALYSIS.)

I	REACTION(I) (IGNORED REACTIONS ARE NOT NUMBERED)	RATE CONSTANTS KF(I)	KR(I)	RATE REFERENCES AND/OR COMMENTS
12	KR** + E ⇌ KR(•) + E + E	(COMPUTED)		30 E-16 CM2 AT 3.1 EV THRESHOLD. FORWARD RATE IS OBTAINED FROM E- KINETICS ANALYSIS REVERSE REACTION IS IGNORED -- KR = 0.
13	AR2(•) + E ⇌ AR** + AR	(COMPUTED)		MEHR, BIONDI (SYNTHETIC) TE**(-3/2) LAW) FORWARD RATE IS OBTAINED FROM E- KINETICS ANALYSIS REVERSE REACTION IS IGNORED -- KR = 0.
14	KR2(•) + E ⇌ KR** + KR	(COMPUTED)		OSKAM, MITTELSTADT (SYNTHETIC) TE**(-3/2) LAW) FORWARD RATE IS OBTAINED FROM E- KINETICS ANALYSIS REVERSE REACTION IS IGNORED -- KR = 0.
15	F2 + E ⇌ F + F-	(COMPUTED)		HOFLAND, AEROSPACE CORP. FORWARD RATE IS OBTAINED FROM E- KINETICS ANALYSIS REVERSE REACTION IS IGNORED -- KR = 0.
16	AR2** + E ⇌ AR + AR + E	1.0000E-07		REVERSE REACTION IS IGNORED -- KR = 0.
17	KR2** + E ⇌ KR + KR + E	1.0000E-07		REVERSE REACTION IS IGNORED -- KR = 0.
18	AR + HE- ⇌ AR(•) + HE- + E	4.3400E-18		BERGER-SELTZER: STOP = 1.7 MEVCM2/GM (300 KEV) REVERSE REACTION IS IGNORED -- KR = 0.
19	AR + HE- ⇌ AR** + HE-	1.2400E-18	1.2400E-18	(1/3.5) X AR + HE ⇌ AR(•) + E + HE
20	KR + HE- ⇌ KR(•) + HE- + E	8.0400E-18		BERGER-SELTZER: STOP = 1.5 MEVCM2/GM (300 KEV) REVERSE REACTION IS IGNORED -- KR = 0.
21	KR + NE- ⇌ KR** + HE-	2.3000E-18	2.3000E-18	(1/3.5) X KR + HE ⇌ KR(•) + E + HE
22	AR(•) + AR + M ⇌ AR2(•) + M	2.0000E-31		W. F. LIU, D. C. CONWAY JCP 62, 3C70 (1975) REVERSE REACTION IS IGNORED -- KR = 0.
23	AR(•) + KR + M ⇌ ARKR(•) + M	2.5000E-31		REVERSE REACTION IS IGNORED -- KR = 0.
24	KR(•) + KR + M ⇌ KR2(•) + M	2.4000E-31		C. J. TRACY, N. J. OSKAM JCP 65, 3387 (1976) REVERSE REACTION IS IGNORED -- KR = 0.
25	KR(•) + AR + M ⇌ ARKR(•) + M	1.0000E-31		REVERSE REACTION IS IGNORED -- KR = 0.
26	AR(•) + KR ⇌ AR + KR(•)	3.0000E-11	X E(-E/KT)	REVERSE RATE IS OBTAINED FROM DETAILED BALANCE.

GENERALIZED KINETICS SYNTHESIS CODE: DR. WILLIAM B. LACINA, NORTHROP RESEARCH AND TECHNOLOGY.   DATE: 10/21/77

Figure 36 (continued)

SUMMARY OF INPUT: REACTIONS AND RATE CONSTANTS (SEC-1, CM3/SEC, CM6/SEC, ..., OR CM2) WITH REFERENCES

(IF A RATE CONSTANT KF OR KR FOR A BINARY ELECTRON COLLISION IS NOT EXPLICITLY SPECIFIED, IT WILL BE COMPUTED SELF CONSISTENTLY AS A FUNCTION OF E/N. GAS COMPOSITION, AND EXCITED LEVEL DENSITIES FROM A COUPLED ELECTRON ANALYSIS.)

I	REACTION(I) (IGNORED REACTIONS ARE NOT NUMBERED)	RATE CONSTANTS KF(I) KR(I)	RATE REFERENCES AND/OR COMMENTS
27	AR2(+) + KR ⇌ KR(+) + AR + AR	7.5000E-10	BOHME ET AL, J. CHEM. PHYS. 52, 5094 (1970) REVERSE REACTION IS IGNORED -- KR = 0.
28	ARKH(+) + KR ⇌ KH2(+) + AR	3.2000E-10 X E(-E/KT)	BOHME ET AL, J. CHEM. PHYS. 52, 5094 (1970) REVERSE RATE IS OBTAINED FROM DETAILED BALANCE.
29	AR* + AR + M ⇌ AR2* + M	1.0000E-32	HILL, GUTCHECK, MUESTIS, ET AL. SRI REPORT, 1974. REVERSE REACTION IS IGNORED -- KR = 0.
30	AR* + KR + M ⇌ ARKR* + M	1.0000E-32	REVERSE REACTION IS IGNORED -- KR = 0.
31	KR* + KR + M ⇌ KR2* + M	5.5000E-32	HUGHES LASL ASPEN 9/76 REVERSE REACTION IS IGNORED -- KR = 0.
32	KR* + AR + M ⇌ ARKR* + M	1.0000E-32	REVERSE REACTION IS IGNORED -- KR = 0.
33	ARKR* + KR ⇌ KR2* + AR	1.0000E-10 X E(-E/KT)	SRI REPORT NO. MP 76-99, DEC. 1976 REVERSE RATE IS OBTAINED FROM DETAILED BALANCE.
34	AR2(+) + F- ⇌ ARF* + AR	5.0000E-07 X E(-E/KT)	REVERSE RATE IS OBTAINED FROM DETAILED BALANCE.
35	AR2(+) + F- ⇌ AR2F*	5.0000E-07	REVERSE REACTION IS IGNORED -- KR = 0.
36	AR(+) + F- ⇌ ARF*	1.0000E-06	REVERSE REACTION IS IGNORED -- KR = 0.
37	KR2(+) + F- ⇌ KRF* + KR	5.0000E-07 X E(-E/KT)	REVERSE RATE IS OBTAINED FROM DETAILED BALANCE.
38	KR2(+) + F- ⇌ KR2F*	5.0000E-07	REVERSE REACTION IS IGNORED -- KR = 0.
39	KR(+) + F- ⇌ KRF*	1.0000E-06	REVERSE REACTION IS IGNORED -- KR = 0.
40	ARKR(+) + F- ⇌ KRF* + AR	5.0000E-07 X E(-E/KT)	REVERSE RATE IS OBTAINED FROM DETAILED BALANCE.
41	ARKR(+) + F- ⇌ ARKRF*	5.0000E-07	REVERSE REACTION IS IGNORED -- KR = 0.
42	KR* + F2 ⇌ KRF* + F	7.2000E-10 X E(-E/KT)	VELAZCO, KOLTS, SETSEH, JCP 65, 3469 (1976) REVERSE RATE IS OBTAINED FROM DETAILED BALANCE.
43	AR* + F2 ⇌ ARF* + F	7.5000E-10 X E(-E/KT)	VELAZCO, KOLTS, SETSER, JCP 65, 3469 (1976), REVERSE RATE IS OBTAINED FROM DETAILED BALANCE.

GENERALIZED KINETICS SYNTHESIS CODE: DR. WILLIAM B. LACINA, NORTHROP RESEARCH AND TECHNOLOGY.   DATE: 10/21/77

Figure 36 (continued)

SUMMARY OF INPUT) REACTIONS AND RATE CONSTANTS (SEC-1, CM3/SEC, CM6/SEC, ..., OR CM2) WITH REFERENCES

(IF A RATE CONSTANT KF OR KR FOR A BINARY ELECTRON COLLISION IS NOT EXPLICITLY SPECIFIED, IT WILL BE COMPUTED SELF
CONSISTENTLY AS A FUNCTION OF E/N, GAS COMPOSITION, AND EXCITED LEVEL DENSITIES FROM A COUPLED ELECTRON ANALYSIS.)

I	REACTION(I) (IGNORED REACTIONS ARE NOT NUMBERED)	RATE CONSTANTS KF(I)	KR(I)	RATE REFERENCES AND/OR COMMENTS
44	AR* + KR ≈ AR + KR*	6.2000E-12 × E(-E/KT)		PIPER, SEISER, CLYNE, JCP 63, 618 (1975) / REVERSE RATE IS OBTAINED FROM DETAILED BALANCE.
45	KRF* + AR ≈ H + ARKRF* + N	6.0000E-32		AVCO / REVERSE REACTION IS IGNORED -- KR = 0.
46	KRF* + AR ≈ H + KR2F* + M	5.0000E-31		AVCO / REVERSE REACTION IS IGNORED -- KR = 0.
47	ARF* + AR ≈ N + AR2F* + M	4.0000E-31		AVCO / REVERSE REACTION IS IGNORED -- KR = 0.
48	ARF* + KR ≈ M + ARKRF* + M	1.0000E-31		REVERSE REACTION IS IGNORED -- KR = 0.
49	AR2* + KR ≈ AR + AR + KR*	8.0000E-11		ZAMIR (PRIV. COMM'N. TO SRI) / REVERSE REACTION IS IGNORED -- KR = 0.
50	AR2* + AR2(*) ≈ AR + AR + E	3.0000E-10		REVERSE REACTION IS IGNORED -- KR = 0.
51	ARF* + KR ≈ F* + AR	1.5000E-10 × E(-E/KT)		SRI REPORT NO. MP 76-99, DEC., 1976 / REVERSE RATE IS OBTAINED FROM DETAILED BALANCE.
52	AR2* + F ≈ ARF* + AR	3.0000E-10 × E(-E/KT)		REVERSE RATE IS OBTAINED FROM DETAILED BALANCE.
53	KR2* + F ≈ KRF* + KR	3.0000E-10 × E(-E/KT)		REVERSE RATE IS OBTAINED FROM DETAILED BALANCE.
54	AR2* + F2 ≈ AR2F* + F	2.5000E-10 × E(-E/KT)		SRI REPORT NO. MP 76-99, DEC., 1976 / REVERSE RATE IS OBTAINED FROM DETAILED BALANCE.
55	ARKR* + F2 ≈ KRF* + AR + F	6.0000E-10		SRI REPORT NO. MP 76-99, DEC., 1976 / REVERSE REACTION IS IGNORED -- KR = 0
56	ARKR* + F2 ≈ ARKRF* + F	3.0000E-10 × E(-E/KT)		REVERSE RATE IS OBTAINED FROM DETAILED BALANCE.
57	KR2* + F2 ≈ KR2F* + F	3.0000E-10 × E(-E/KT)		SRI REPORT NO. MP 76-99, DEC., 1976 / REVERSE RATE IS OBTAINED FROM DETAILED BALANCE.
58	AR2F* + F2 ≈ AR + AR + F + F2	1.0000E-09		SRI REPORT NO. MP 76-99, DEC., 1976 / REVERSE REACTION IS IGNORED -- KR = 0.
59	ARKRF* + F2 ≈ AR + KR + F + F2	1.0000E-09		SRI REPORT NO. MP 76-99, DEC., 1976 / REVERSE REACTION IS IGNORED -- KR = 0.

GENERALIZED KINETICS SYNTHESIS CODE; DR. WILLIAM B. LACINA, NORTHROP RESEARCH AND TECHNOLOGY.   DATE: 10/21/77

Figure 36 (continued)

90

SUMMARY OF INPUT: REACTIONS AND RATE CONSTANTS (SEC-1, CM3/SEC, CM6/SEC, ..., OR CM2) WITH REFERENCES

(IF A RATE CONSTANT KF OR KR FOR A BINARY ELECTRON COLLISION IS NOT EXPLICITLY SPECIFIED, IT WILL BE COMPUTED SELF CONSISTENTLY AS A FUNCTION OF E/N. GAS COMPOSITION, AND EXCITED LEVEL DENSITIES FROM A COUPLED ELECTRON ANALYSIS.)

I	REACTION(I) (IGNORED REACTIONS ARE NOT NUMBERED)	RATE CONSTANTS KF(I)	KR(I)	RATE REFERENCES AND/OR COMMENTS
60	KR2F* + F2 + KR + KR + F + F2	1.0000E-09		SRI REPORT NO. MP 76-99, DEC., 1976 REVERSE REACTION IS IGNORED -- KR = 0.
61	ARKRF* + KR + KR2F* + AR	1.0000E-10	X E(-E/KT)	SRI REPORT NO. MP 76-99, DEC., 1976 REVERSE RATE IS OBTAINED FROM DETAILED BALANCE.
62	KRF* + F2 + KR + F + F2	1.0000E-09		SRI REPORT NO. MP 76-99, DEC., 1976 REVERSE REACTION IS IGNORED -- KR = 0.
63	ARF* + F2 + AR + F + F2	1.0000E-09		SRI REPORT NO. MP 76-99, DEC., 1976 REVERSE REACTION IS IGNORED -- KR = 0.
64	AR2F* + KR + KRF* + AR + AR	1.0000E-10		REVERSE REACTION IS IGNORED -- KR = 0.
65	AR** + M + AR* + M	1.0000E-10	X E(-E/KT)	REVERSE RATE IS OBTAINED FROM DETAILED BALANCE.
66	KR** + M + KR* + M	1.0000E-10	X E(-E/KT)	REVERSE RATE IS OBTAINED FROM DETAILED BALANCE.
67	ARF* + AR + F	3.3000E-07		SRI REPORT NO. MP 76-99, DEC., 1976 REVERSE REACTION IS IGNORED -- KR = 0.
68	AR2* + AR + AR	3.8000E-06		SRI REPORT NO. MP 76-99, DEC., 1976 REVERSE REACTION IS IGNORED -- KR = 0.
69	ARKR* + AR + KR	3.0000E-06		REVERSE REACTION IS IGNORED -- KR = 0.
70	KR2* + KR + KR	3.3000E-06		SRI REPORT NO. MP 76-99, DEC., 1976 REVERSE REACTION IS IGNORED -- KR = 0.
71	AR2F* + AR + AR + F	2.0000E-08		SRI REPORT NO. MP 76-99, DEC., 1976 REVERSE REACTION IS IGNORED -- KR = 0.
72	ARKRF* + AR + KR + F	5.0000E-07		SRI REPORT NO. MP 76-99, DEC., 1976 REVERSE REACTION IS IGNORED -- KR = 0.
73	KR2F* + KR + KR + F	6.7000E-07		SRI REPORT NO. MP 76-99, DEC., 1976 REVERSE REACTION IS IGNORED -- KR = 0.
74	KRF* + KR + F + HNU	1.1000E-08		R. BURNHAM, S. S. SEARLES (SUBMITTED TO JCP) REVERSE REACTION IS IGNORED -- KR = 0. NO REVERSE REACTION ALLOWED FOR RADIATIVE DECAY.

GENERALIZED KINETICS SYNTHESIS CODE: DR. WILLIAM B. LACINA, NORTHROP RESEARCH AND TECHNOLOGY.   DATE: 10/21/77

Figure 36 (continued)

SUMMARY OF INPUT: REACTIONS AND RATE CONSTANTS (SEC-1, CM3/SEC, CM6/SEC, ..., OR CM2) WITH REFERENCES

(IF A RATE CONSTANT KF OR KR FOR A BINARY ELECTRON COLLISION IS NOT EXPLICITLY SPECIFIED, IT WILL BE COMPUTED SELF CONSISTENTLY AS A FUNCTION OF E/N. GAS COMPOSITION, AND EXCITED LEVEL DENSITIES FROM A COUPLED ELECTRON ANALYSIS.)

I	REACTION(I) (IGNORED REACTIONS ARE NOT NUMBERED)	RATE CONSTANTS KF(I)	KR(I)	RATE REFERENCES AND/OR COMMENTS
75	KRF* + RAD +́ KR + F + RAD	2.0000E-16		LASER TRANSITION: STIMULATED EMISSION X-SECTION REVERSE REACTION IS IGNORED -- KR = 0.
76	F2 + RAD +́ F + F	1.5000E-20		REVERSE REACTION IS IGNORED -- KR = 0.
77	F- + RAD +́ F + E	5.4000E-18		A. MANDL, PHYS REV A3, 251 (1971) REVERSE REACTION IS IGNORED -- KR = 0.
78	KR2F* + RAD +́ AR* + KR + F	1.0000E-99		CROSS SECTION UNKNOWN REVERSE REACTION IS IGNORED -- KR = 0.
79	AR2(+) + RAD +́ AR + AR(+)	1.5000E-17		STEVENS (PARK CITY CONFERENCE) REVERSE REACTION IS IGNORED -- KR = 0.
80	KR2(+) + RAD +́ KR + KR(+)	3.5000E-19		J. WEST (NRTC) REVERSE REACTION IS IGNORED -- KR = 0.

GENERALIZED KINETICS SYNTHESIS CODE: DR. WILLIAM B. LACINA, NORTHROP RESEARCH AND TECHNOLOGY.   DATE: 10/21/77

OF 80 INPUT REACTIONS SCANNED, 80 WERE RETAINED (MAXIMUM ALLOWED = 200) AND 0 WERE IGNORED FOR REASONS ITEMIZED IN THE TABLE. OF THOSE RETAINED, 15 REQUIRE RATES FROM AN E- KINETICS ANALYSIS. 24 SEPARATE SPECIES WERE ENCOUNTERED (MAXIMUM ALLOWED = 30).

Figure 36 (continued)

92

SUMMARY OF REACTIONS FOR WHICH EACH SPECIES OCCURS NTYPE = 24
(THIS EDIT PERMITS RAPID DELETION OF ANY SPECIES FROM THE KINETIC SYSTEM)

REACTIONS CONTAINING GAS(I)

I	GAS(I)	Reactions
1	RAD	75, 76, 77, 78, 79, 80.
2	E(-)	1, 2, 3, 4, 5, 6, 7, 8, 9, 10, 11, 12, 13, 14, 15, 16, 17, 18, 20, 50, 77.
3	AR	1, 3, 7, 13, 16, 18, 19, 22, 25, 26, 27, 28, 29, 32, 33, 34, 40, 44, 45, 47, 43, 50, 51, 52, 55, 58, 59, 61, 63, 64, 67, 68, 69, 71, 72, 79.
4	AR°	1, 5, 9, 13, 19, 29, 30, 43, 44, 65, 78.
5	KR	2, 4, 8, 14, 17, 20, 21, 23, 24, 26, 27, 28, 30, 31, 33, 34, 37, 44, 46, 48, 49, 51, 53, 59, 60, 61, 62, 64, 69, 70, 72, 73, 74, 75, 78, 80.
6	KR°	2, 6, 10, 14, 21, 31, 32, 42, 44, 49, 66.
7	AR°°	3, 5, 11, 65.
8	KR°°	4, 6, 12, 66.
9	AR(°)	7, 9, 11, 18, 22, 23, 26, 36, 79.
10	KR(°)	8, 10, 12, 20, 24, 25, 26, 27, 39, 80.
11	AR2(°)	13, 22, 27, 34, 35, 50, 79.
12	KR2(°)	14, 24, 28, 37, 38, 80.
13	F2	15, 42, 43, 54, 55, 56, 57, 58, 59, 60, 62, 63, 76.
14	F	15, 42, 43, 52, 53, 54, 55, 56, 57, 58, 59, 60, 62, 63, 67, 71, 72, 73, 74, 75, 76, 77, 78.
15	F-	15, 34, 35, 36, 37, 38, 39, 40, 41, 77.
16	AR2°	16, 29, 49, 50, 52, 54, 68.
17	KR2°	17, 31, 33, 53, 57, 70.
18	AHKR(°)	23, 25, 28, 40, 41.
19	AHKR°	30, 32, 33, 55, 56, 69.

Figure 37.   Summary of Reactions for which each Species Occurs

93

SUMMARY OF REACTIONS FOR WHICH EACH SPECIES OCCURS; NTYPE = 24
(THIS EDIT PERMITS RAPID DELETION OF ANY SPECIES FROM THE KINETIC SYSTEM)

I	GAS(I)	REACTIONS CONTAINING GAS(I)
20	ARF*	34, 36, 43, 47, 48, 51, 52, 63, 67,
21	AR2F*	35, 47, 54, 58, 64, 71,
22	KRF*	37, 39, 40, 42, 45, 46, 51, 53, 55, 62, 64, 74, 75,
23	KR2F*	38, 46, 57, 60, 61, 73, 78,
24	ARKRF*	41, 45, 48, 56, 59, 61, 72,

GENERALIZED KINETICS SYNTHESIS CODE; DR. WILLIAM B. LACINA, NORTHROP RESEARCH AND TECHNOLOGY. DATE: 10/21/77

Figure 37 (continued)

94

SUMMARY OF CARO IMAGES FOR INPUT OATA DECK
(OATE: 10/21/77)

```
CAHO              1         2         3         4         5         6         7         8
NO.      1234567890123456789012345678901234567890123456789012345678901234567890123456789012345678901234567890
```

```
  1 .... SCONTROL          IO(1) = 10,0,0,10,10,5,0,0,25,1$
  2 .... SPARAM            TPULSE = 1.0E-06,
  3 ....                   ATM = 1.7$
  4 .... SOPTICAL          REFLECT = 70.,
  5 ....                   LOSS = 0.,
  6 ....                   AREA = 25.,
  7 ....                   CAVITY = 130.,
  8 ....                   LENGTH = 75.0$
  9 .... SEBEAM            JBEAM = 12.0,
 10 ....                   ENERGY = 320.,
 11 ....                   TAXIS(1) =      0.,  50.,  100.,  150.,  200.,
 12 ....                                 250.,  300.,  350.,  400.,  450.,
 13 ....                                 500.,  550.,  600.,  650.,  700.,
 14 ....                                 750.,  800.,  850.,  900.,  950.,  1000.,
 15 ....                   JSHAPE(1) =   0.00,  0.82,  1.00,  0.99,  0.90,
 16 ....                                 0.85,  0.77,  0.73,  0.69,  0.67,
 17 ....                                 0.69,  0.72,  0.75,  0.75,  0.72,
 18 ....                                 0.65,  0.42,  0.20,  0.05,  0.02,  0.00,
 19 ....                   DEPOSIT = 2.$
 20 .... SCIRCUIT          CAPAC = 1.33E-06,
 21 ....                   INDUCT = 200.E-09,
 22 ....                   RESIST = 0.,
 23 ....                   KVOLT = 40.0,
 24 ....                   AREA = 2000.,
 25 ....                   OIST = 10.$
 26 .... SRATES $
 27 ....AR           1191.                    40.
 28 ....KR            100.                    84.
 29 ....F2              1.5                    38.           PLOT
 30 ....AR*                      11.5
 31 ....KR*                       9.9                        PLOT
 32 ....AR2(*)                   13.0
 33 ....KR2(*)                   11.8                        PLOT
 34 ....ARKR(*)                  12.4
 35 ....AR**                     13.5
 36 ....AR(*)                    15.8
 37 ....KR**                     11.5
 38 ....KR(*)                    14.4
 39 ....F-                         .01                       PLOT
 40 ....ARF*                      6.5
```

```
         1234567890123456789012345678901234567890123456789012345678901234567890123456789012345678901234567890
              1         2         3         4         5         6         7         8
```

Figure 38.   Summary of Card Images for Input Data Deck

95

SUMMARY OF CARD IMAGES FOR INPUT DATA DECK
(DATE: 10/21/77)

```
CARD            1         2         3         4         5         6         7         8
NO.    12345678901234567890123456789012345678901234567890123456 8901234567890
------------------------------------------------------------------------------

                                           5.0              PLOT
41 ....KRF*                                9.5
42 ....AR2*                                8.2
43 ....KR2*                                5.0
44 ....AR2F*                               4.0
45 ....ARKRF*                              3.0
46 ....KR2F*                               8.8
47 ....ARKR*                                                PLOT
48 ....E(-)
------------------------------------------------------------------------------

       1234567890123456789012345670 012345678901234567890123456789012345678901234567890
              1         2         3         4         5         6         7         8
```

Figure 38 (continued)

96

collisions and quenching processes, spontaneous radiative decay, stimulated emission, and absorption from F_2 and various excited transient species in the active medium. Figure 38 illustrates the input data deck for execution of the analysis for conditions typical of the scale-up device experiments.[*] Figure 39 summarizes the input reaction scheme after rate constants (if any) have been modified (none for the present example).

Figures 40-57 illustrate typical output generated during execution of the analysis. The formating is explicit enough that the material presented in these figures should be self-explanatory. In order to provide some quantitative assessment of the sensitivity of the various reactions included in the kinetic scheme, the computer code generates, according to output request, tables such as those presented in Figure 45. These tables summarize the numerical value of the contribution each reaction makes (at any given time) to each species in the system, expressed for each species as a percentage of the maximum rate occuring for that species. Those reactions which never contribute more than a specified percentage are flagged with an asterisk, and are summarized at the conclusion of the analysis. Thus, after a variety of calculations have been made for different experimental conditions and parameters, it is possible to determine whether any given reaction may be considered to be relatively unimportant and deleted from the kinetic scheme.

Figures 46-57 represent a portion of the computer plots generated at the termination of the analysis. Included are temporal plots of e^--beam current density, radiation intensity, intracavity gain and absorption coefficients, electrical input and optical extraction power densities, discharge current density and voltage, plasma conductivity and impedance, output energy and efficiency, and (requested) population densities of excited species.

---

[*] Due to multiple scattering effects, energy deposition in a high pressure gas is somewhat greater than that given by the Berger-Seltzer cross sections. The effective cross sections used in the analysis are taken to be a factor of 2.0 higher (cf. DEPOSIT = 2.0 in Figure 39).

(VSIG(K,I) ARE FORWARD (K=1) OR REVERSE (K=2) RATES FOR THE ITH INELASTIC PROCESS IN THE E- KINETICS ANALYSIS)

I	REACTION(I)	KF(I)	KR(I)	REFERENCES OR COMMENTS
1	AR + E ⇌ AR* + E	VSIG(1, 1)	VSIG(2, 1)	SCHAPER, SCHEIBNER, BEITR. AUS PLASMA PHYS. 9, 45
2	KR + E ⇌ KR* + E	VSIG(1, 2)	VSIG(2, 2)	SCHAPER, SCHEIBNER, BEITR. A"S PLASMA PHYS. 9, 45
3	AR + E ⇌ AR** + E	VSIG(1, 3)	VSIG(2, 3)	0.1 X AR* CROSS SECTION, 13.4 EV THRESH
4	KR + E ⇌ KR** + E	VSIG(1, 4)	VSIG(2, 4)	0.1 X AR* CROSS SECTION, 11.5 EV THRESH
5	AR* + E ⇌ AR** + E	VSIG(1, 5)	VSIG(2, 5)	60.E-16 CM2 AT 2 EV THRESHOLD ASSUMED.
6	KR* + E ⇌ KR** + E	VSIG(1, 6)	VSIG(2, 6)	60.E-16 CM2 AT 1.6 EV THRESHOLD ASSUMED.
7	AR + E ⇌ AR(+) + E + E	VSIG(1, 7)		RAPP, ENGLANDER-GOLDEN JCP 43, 1464 (65)
8	KR + E ⇌ KR(+) + E + E	VSIG(1, 8)		RAPP, ENGLANDER-GOLDEN JCP 3, 1464 (65)
9	AR* + E ⇌ AR(+) + E + E	VSIG(1, 9)		7.E-16 CM2 AI 4.2 EV THRESHOLD ASSUMED.
10	KR* + E ⇌ KR(+) + E + E	VSIG(1,10)		10.E-16 CM2 AT 4.0 EV THRESHOLD ASSUMED.
11	AR** + E ⇌ AR(+) + E + E	VSIG(1,11)		30 E-16 CM2 AT 2.4 EV THRESHOLD.
12	KR** + E ⇌ KR(+) + E + E	VSIG(1,12)		30 E-16 CM2 AT 3.1 EV THRESHOLD.
13	AR2(+) + E ⇌ AR* + AR	VSIG(1,13)		MEHR, BIONDI (SYNTHETIC: TE**(-3/2) LAW)
14	KR2(+) + E ⇌ KR* + KR	VSIG(1,14)		OSKAM, MITTELSTADT (SYNTHETIC: TE**(-3/2) LAW)
15	F2 + E ⇌ F- + F-	VSIG(1,15)		HOFLAND, AEROSPACE CORP.
16	AR2* + E ⇌ AR + AR + E	1.0000E-07		
17	KR2* + E ⇌ KR + KR + E	1.0000E-97		
18	AR + HE- ⇌ AR(+) + HE- + E	4.3400E-18		BERGER-SELTZER: STOP = 1.7 MEVCM2/GM (300 KEV)
19	AR + HE- ⇌ AR* + HE-	1.2400E-18	1.2400E-18	(1/3.5) X AR + HE ⇌ AR(+) + E + HE
20	KR + HE- ⇌ KR(+) + HE- + E	8.0400E-18		BERGER-SELTZER: STOP = 1.5 MEVCM2/GM (300 KEV)
21	KR + HE- ⇌ KR* + HE-	2.3000E-18	2.3000E-18	(1/3.5) X KR + HE ⇌ KR(+) + E + HE
22	AR(+) + AR + M ⇌ AR2(+) + M	2.0000E-31		W. F. LIU, D. C. CONWAY JCP 62, 3070 (1975)
23	AR(+) + KR + M ⇌ ARKR(+) + M	2.5000E-31		
24	KR(+) + KR + M ⇌ KR2(+) + M	2.4000E-31		C. J. TRACY, M. J. OSKAM JCP 65, 3307 (1976)
25	KR(+) + AR + M ⇌ ARKR(+) + M	1.0000E-31		

Figure 39. Summary of Updated Rates for Input Reaction Scheme
of Synthetic Kinetics Code

98

SUMMARY OF UPDATED RATES FOR INPUT REACTION SCHEME OF SYNTHETIC KINETICS CODE GENERATED ON 10/21/77
WILLIAM B. LACINA, NORTHROP RESEARCH AND TECHNOLOGY CENTER, HAWTHORNE, CALIFORNIA

(VSIG(K,I) ARE FORWARD (K=1) OR REVERSE (K=2) RATES FOR THE ITH INELASTIC PROCESS IN THE E- KINETICS ANALYSIS)

I	REACTION(I)	KF(I)	KR(I)	REFERENCES OR COMMENTS
26	AR(*) + KR ≁ AR + KR(*)	3.0000E-11	X E(-E/KT)	
27	AR2(*) + KR ≁ KR(*) + AR + AR	7.5000E-10		BOHME ET AL, J. CHEM. PHYS. 52, 5094 (1970)
28	ARKR(*) + KR ≁ KR2(*) + AR	3.2000E-10	X E(-E/KT)	BOHME ET AL, J. CHEM. PHYS. 52, 5094 (1970)
29	AR* + AR + M ≁ AR2* + M	1.0000E-32		MILL, GUTCHECK, MUESTIS, ET AL, SRI REPORT, 1974.
30	AR* + KR + M ≁ ARKR* + M	1.0000E-32		
31	KR* + KR + M ≁ KR2* + M	5.5000E-32		HUGHES LASL ASPEN 9/76
32	KR* + AR + M ≁ ARKR* + M	1.0000E-32		
33	ARKR* + KR ≁ KR2* + AR	1.0000E-10	X E(-E/KT)	SRI REPORT NO. N° 76-99, DEC., 1976
34	AR2(*) + F- ≁ ARF* + AR	5.0003E-07	X E(-E/KT)	
35	AR2(*) + F- ≁ AR2F*	5.0000E-07		
36	AR(*) + F- ≁ ARF*	1.0000E-06		
37	KR2(*) + F- ≁ KRF* + KR	5.0000E-07	X E(-E/KT)	
38	KR2(*) + F- ≁ KR2F*	5.0000E-07		
39	KR(*) + F- ≁ KRF*	1.0000E-06		
40	ARKR(*) + F- ≁ KRF* + AR	5.0000E-07	X E(-E/KT)	
41	ARKR(*) + F- ≁ ARKRF*	5.0000E-07		
42	KR* + F2 ≁ KRF* + F	7.2000E-10	X E(-E/KT)	VELAZCO, KOLTS, SETSER, JCP 65, 3469 (1976)
43	AR* + F2 ≁ ARF* + F	7.5000E-10	X E(-E/KT)	VELAZCO, KOLTS, SETSER, JCP 65, 3469 (1976)
44	AR* + KR + AR ≁ KR*	6.2000E-12	X E(-E/KT)	PIPER, SETSER, CLYNE, JCP 63, 4018 (1975)
45	K-- + AR + M ≁ ARKRF* + M	6.0000E-32		AVCO
46	KRF* + KR + M ≁ KR2F* + M	5.0000E-31		AVCO
47	ARF* + AR + M ≁ AR2F* + M	4.0000E-31		AVCO
48	ARF* + KR + M ≁ ARKRF* + M	1.0000E-31		
49	AR2* + KR ≁ AR + AR + KR*	8.0000E-11		ZAMIR (PRIV. COMMUN. TO SRI)
50	AR2* + AR2(*) ≁ AR + AR + AR + E	3.0000E-10		

Figure 39 (continued)

SUMMARY OF UPDATED RATES FOR INPUT REACTION SCHEME OF SYNTHETIC KINETICS CODE GENERATED ON 10/21/77
WILLIAM B. LACINA, NORTHROP RESEARCH AND TECHNOLOGY CENTER, HAWTHORNE, CALIFORNIA

(VSIG(IK,1) ARE FORWARD (K=1) OR REVERSE (K=2) RATES FOR THE ITH INELASTIC PROCESS IN THE E- KINETICS ANALYSIS)

I	REACTION(I)	KF(I)	KR(I)	REFERENCES OR COMMENTS
51	ARF* + KR → KRF* + AR	1.5000E-10	X E(-E/KT)	SRI REPORT NO. MP 76-99, DEC., 1976
52	AR2* + F → ARF* + AR	3.0000E-10	X E(-E/KT)	
53	KR2* + F → KRF* + KR	3.0000E-10	X E(-E/KT)	
54	AR2* + F2 → AR2F* + F	2.5000E-10	X E(-E/KT)	SRI REPORT NO. MP 76-99, DEC., 1976
55	ARKR* + F2 → KRF* + AR + F	5.0000E-10		SRI REPORT NO. MP 76-99, DEC., 1976
56	ARKR* + F2 → ARKRF* + F	3.0000E-10	X E(-E/KT)	
57	KR2* + F2 → KR2F* + F	3.0000E-10	X E(-E/KT)	SRI REPORT NO. MP 76-99, DEC., 1976
58	AR2F* + F2 → AR + AR + F + F2	1.0000E-09		SRI REPORT NO. MP 76-99, DEC., 1976
59	ARKRF* + F2 → AR + KR + F + F2	1.0000E-09		SRI REPORT NO. MP 76-99, DEC., 1976
60	KR2F* + F2 → KR + KR + F + F2	1.0000E-09		SRI REPORT NO. MP 76-99, DEC., 1976
61	ARKRF* + KR → KR2F* + AR	1.0000E-10	X E(-E/KT)	SRI REPORT NO. MP 76-99, DEC., 1976
62	KRF* + F2 → KR + F + F2	1.0000E-09		SRI REPORT NO. MP 76-99, DEC., 1976
63	ARF* + F2 → AR + F + F2	1.0000E-09		SRI REPORT NO. MP 76-99, DEC., 1976
64	AR2F* + KR → KRF* + AR + AR	1.0000E-10		
65	AR** + M → AR* + M	1.0000E-10	X E(-E/KT)	
66	KR** + M → KR* + M	1.0000E-10	X E(-E/KT)	
67	ARF* + AR → F	3.3000E-07		SRI REPORT NO. MP 76-99, DEC., 1976
68	AR2* + AR → AR	3.0000E-06		SRI REPORT NO. MP 76-99, DEC., 1976
69	ARKR* + AR → KR	3.0000E-06		
70	KR2* + KR → KR	3.3000E-06		SRI REPORT NO. MP 76-99, DEC., 1976
71	AR2F* + AR → AR + F	2.0000E-08		SRI REPORT NO. MP 76-99, DEC., 1976
72	ARKRF* + AR → KR + F	5.0000E-07		SRI REPORT NO. MP 76-99, DEC., 1976
73	KR2F* + KR → KR + F	6.7000E-07		SRI REPORT NO. MP 76-99, DEC., 1976
74	KRF* + KR → F + HNU	1.1000E-08		R. BURNHAM, S. S. SEARLES (SUBMITTED TO JCP)
75	KRF* + RAD → KR + F + RAD	2.0000E-16		LASER TRANSITION: STIMULATED EMISSION X-SECTION

Figure 39 (continued)

SUMMARY OF UPDATED RATES FOR INPUT REACTION SCHEME OF SYNINETICS CODE GENERATED ON 10/21/77
WILLIAM B. LACINA, NORTHROP RESEARCH AND TECHNOLOGY CENTER, HAWTHORNE, CALIFORNIA

(VSIG(IK,I) ARE FORWARD (K=1) OR REVERSE (K=2) RATES FOR THE ITH INELASTIC PROCESS IN THE E- KINETICS ANALYSIS)

I	REACTION(I)	KF(I)	KR(I)	REFERENCES OR COMMENTS
76	F2 + RAD + F + F	1.5000E-20		
77	F + RAD + F + E	5.4000E-18		A. MANDL, PHYS REV A3, 251 (1971)
78	KR2F + RAD + AR + KR + F	1.0000E-99		CROSS SECTION UNKNOWN
79	AR2(+) + RAD + AR + AR(+)	1.5000E-17		STEVENS (PARK CITY CONFERENCE)
80	KR2(+) + RAD + KR + KR(+)	3.5000E-18		J. WEST (NRTC)

Figure 39 (continued)

101

TIME T = 4.000E-07 SEC

POPULATION DENSITIES AND RATES OF CHANGE

I	SPECIES NAME	E(I) (EV)	N(I) (CM-3)	DN(I)/DT (CM-3/SEC)
1	RAD	0.00	1.192E+14	3.218E+19
2	E(-)	0.00	2.413E+14	4.930E+20
3	AR	0.00	3.830E+19	-2.697E+20
4	AR*	11.50	9.944E+13	1.784E+20
5	KR	0.00	3.214E+18	-1.326E+21
6	KR*	9.90	1.819E+14	4.560E+20
7	AR**	13.50	2.700E+12	9.595E+19
8	KR**	11.50	5.375E+12	1.655E+20
9	AR(+)	15.80	3.550E+13	-1.179E+19
10	KR(+)	14.40	8.096E+13	2.183E+19
11	AR2(+)	13.00	4.453E+12	-3.089E+18
12	KR2(+)	11.80	1.707E+14	1.225E+20
13	F2	0.00	3.566E+16	-3.058E+22
14	F	0.00	2.494E+16	6.149E+22
15	F-	.01	6.321E+13	-3.651E+20
16	AR2*	9.50	5.238E+12	3.302E+18
17	KR2*	8.20	8.502E+13	1.726E+20
18	ARKR(+)	12.40	1.289E+13	-1.578E+18
19	ARKR*	8.80	8.443E+12	1.808E+19
20	ARF*	6.50	4.237E+12	-3.195E+18
21	AR2F*	5.00	5.184E+12	-3.418E+18
22	KRF*	5.00	1.967E+13	-1.038E+18
23	KR2F*	3.00	9.255E+13	3.841E+19
24	ARKRF*	4.00	5.975E+12	2.947E+17

ELECTRICAL AND OPTICAL PARAMETERS

PARAMETER		VALUE	UNITS
JBEAM	=	8.28	AMP/CM2
DEPOSITION	=	2.00	
ENERGY	=	320.	KEV
OVDX	=	11.22	KV/CM
P(BEAM)	=	92.94	KW/CM3
R(EXT)	=	0.00	OHM
L(EXT)	=	2.000E-07	HENRY
C(EXT)	=	1.330E-06	FARAD
AREA	=	2000.00	CM2
DIST	=	10.00	CM
CONDUCT	=	2.225E-02	/OHM/CM
R(DISCH)	=	2.247E-01	OHM
Q	=	3.990E-02	COULOMB
I(DISCH)	=	5.892E+04	AMP
J(DISCH)	=	2.946E+01	AMP/CM2
ESUS	=	1.324	KVOLT/CM
ESUS*JSUS	=	39.01	KW/CM3
Q/C	=	29.997	KVOLT
V(DISCH)	=	13.242	KVOLT
L*DI/DT	=	16.754	KVOLT
REFLECT	=	70.00	%
LOSS	=	0.00	%/PASS
T(CAVITY)	=	24.3	NS
L(CAVITY)	=	130.00	CM
LENGTH	=	75.00	CM
OMEGA/4/PI	=	1.177E-04	
THRES:	=	2.378E-03	CM-1
NET GAIN	=	2.393E-03	CM-1
LASER GAIN	=	3.934E-03	CM-1
ABSORPTION	=	1.541E-03	CM-1
INTENSITY	=	2.862E+06	WATT/CM2
OPTICAL	=	6.85	KW/CM3
EFFICIENCY	=	5.19	%
STEP SIZE	=	3.643E-09	SEC
T(EXTRAP)	=	3.986E-07	SEC
ORDER	=	2	

DR. WILLIAM B. LACINA, 10/21/77
NORTHROP RESEARCH AND TECHNOLOGY

Figure 40. Population Densities and Rates of Change
Electrical and Optical Parameters

```
            TIME T =  4.000E-07 SEC
GAS MIXTURE --

  AR /KR /F2  =  92.15 /  7.74 /   .12

        PLASMA PARAMETERS

------------------------------------------

  E/N       =  3.1302E-17   VOLT CM2
            =     1.01      V/CM/TORR
            =      .77      KV/CM/ATM

  PTOT      =   1292.0      TORR
            =     1.70      ATM

  TMOL      =    300.       DEG K

  NTOT      =  4.1559E+19   CM-3

  E         =  1.3009E+03   VOLT/CM

  UAVG      =   3.492       EV

  TE        =  27022.       DEG K

  D         =  2.3065E+03   CM2/SEC

  MU        =  5.7548E+02   CM2/VOLT/S

  MU=NTOT   =  2.3916E+22   /S/VOLT/CM

  COND/NE   =  9.2191E-17   CM2/OHM

  EK = D/MU =   4.008       EV

  VD = MU*E =  7.4864E+05   CM/SEC

  MU=E**2   =  1.5602E-10   WATT/ELECT

  P/NE      =  1.6551E-10   WATT/ELECT

  P/NE/NMOL =  3.9824E-30   WCM3/EL/MOL

  J/NE      =  1.1993E-13   AMPCM/ELECT

  VSIG(MOM) =  6.9536E-08   CM3/SEC

  NU(MOM)   =  2.8899E+12   SEC-1

  NE/NMOL   =  5.8065E-06

------------------------------------------

CALCULATION PARAMETERS USED&
MESH = 500, EMAX = 15.00 EV, DE = .030 EV.
```
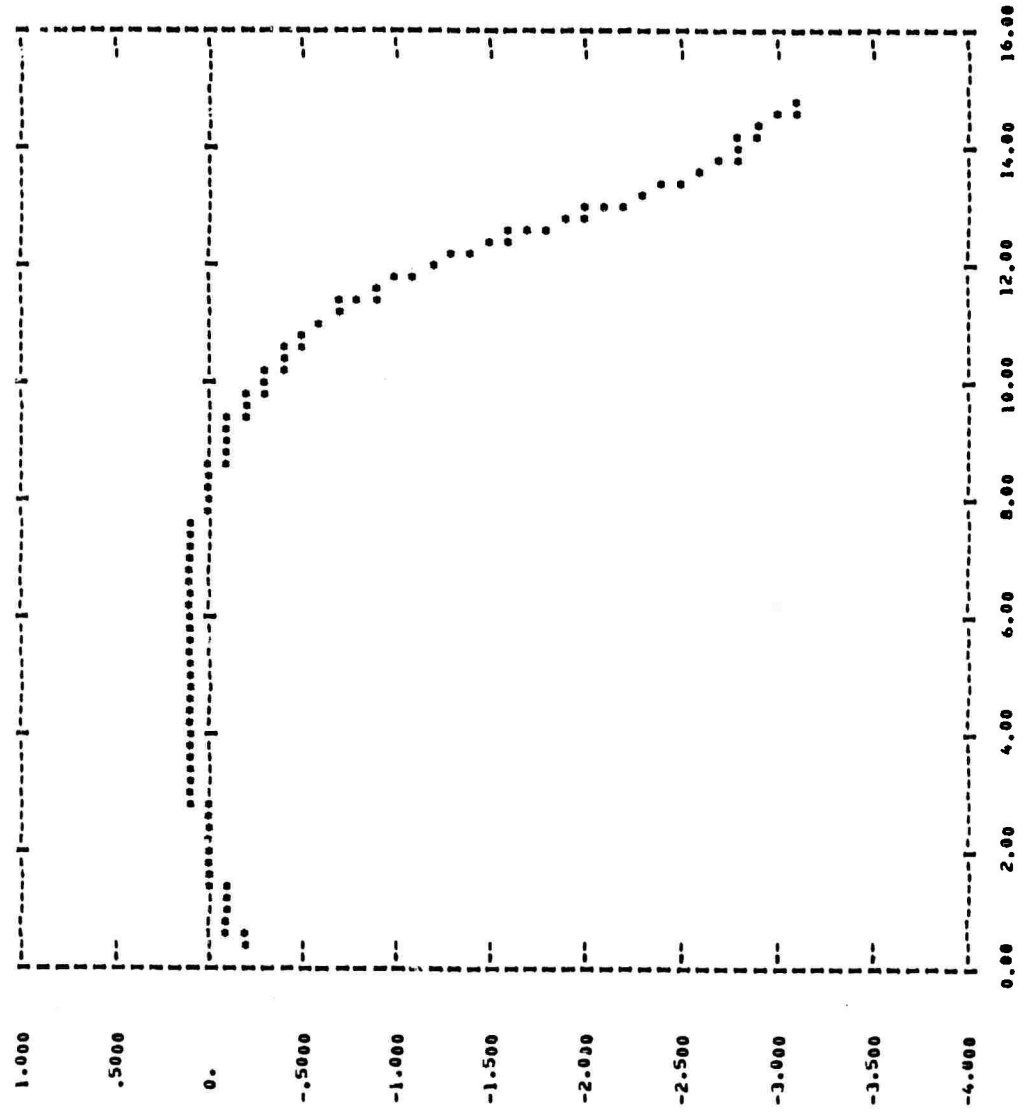
Figure 41.   Plasma Parameters

103

LOG PLOT OF RELATIVE ELECTRON DISTRIBUTION FUNCTION F(U)/FBOLTZ(U,TE), WHERE :E = (2/3)UAVG/KB = 27022. DEG K

E/NTOT = 3.130E-17 VOLT CM2 = 1.007 VOLT/CM/TORR = .765 KVOLT/CM/ATM
FRACTIONAL IONIZATION = NE/NTOT = 5.807E-06
AR /KR /F2 = 92.15 / 7.74 / .12, TMOL = 300. DEG K

ELECTRON ENERGY U (EV)

DR. WILLIAM B. LACINA, 10/21/77
NORTHROP RESEARCH AND TECHNOLOGY

Figure 42   Log Plot of Relative Electron Distribution

104

TIME T = 4.000E-07 SEC

PLASMA KINETICS ANALYSIS WITH SUMMARY OF ELECTRON PARAMETERS, COLLISION RATES, AND POWER BALANCE FOR ALL ELASTIC AND INELASTIC COLLISION PROCESSES INCLUDED

E/NTOT = 3.130E-17 VOLT CN2 = 1.007 VOLT/CM/TORR = .765 KVOLT/CM/ATN
    FRACTIONAL IONIZATION = NE/NTOT = 5.80TE-06
    AR /KR /F2 = 62.15 / 7.74 / .12, TMOL = 300. DEG K

U(AVG) = 3.492 EV, TE = 2T02?. DEG K. VD = 7.49E-05 CN/SEC. NU = 5.75E-02 CN2/VOLT/SEC
    POWER = 1.66E-10 WATT/ELECTRON, J/NE = 1.20E-13 AMP CN/ELECTRON

J	REACTION(J) A + E(-) P B + E(-)	N(A) (CM-3)	N(B) (CM-3)	U(J) EV	<VSIG(A=B)> (CM3/SEC)	<VSIG(B=A)> (CM3/SEC)	(NET) POWER (WATT/ELECTRON)	PERCENT POWER
0	NONENTUM TRANSFER COLLISIONS						6.633E-11	40.08
1	AR + E P AR* + E	3.030E+19	9.944E-13	11.500	2.671E-13	3.077E-09	1.820E-11	11.04
2	KR + E P KR* + E	3.214E+18	1.819E-14	9.900	5.856E-12	6.044E-09	2.811E-11	16.99
3	AR + E P AR** + E	3.030E+19	2.700E-12	13.500	3.674E-16	7.900E-11	2.997E-14	.02
4	KR + E P KR** + E	3.214E+18	5.375E-12	11.500	6.035E-15	2.146E-10	3.361E-14	.02
5	AR* + E P AR** + E	9.944E-13	2.700E-12	2.000	5.03TE-07	1.077E-06	1.511E-11	9.13
6	KR* + E P KR** + E	1.819E-14	5.375E-12	1.600	5.479E-07	9.975E-07	2.418E-11	14.61
7	AR + E P AR(+) + E + E	3.030E+19		15.000	0.		0.	0.00
8	KR + E P KR(+) + E + E	3.214E+18		14.400	2.59TE-15		1.926E-14	.01
9	AR* + E P AR(+) + E + E	9.944E-13		4.300	2.728E-09		1.860E-12	1.13
10	KR* + E P KR(+) + E + E	1.019E+14		4.500	3.173E-08		4.161E-12	2.51
11	AR** + E P AR(+) + E + E	2.700E-12		2.300	1.067E-07		1.061E-13	.06
12	KR** + E P KR(+) + E + E	5.375E-12		2.903	2.005E-07		5.006E-13	.30
13	AR2(+) + E P AR* + AR	4.453E-12			4.537E-08		.95E-14	.04
14	KR2(+) + E P KR* + KR	1.70TE-14			6.806E-08		.252E-12	2.57
15	F2 + E P F + F-	3.566E+16			2.336E-09		2.450E-12	1.40

E*MU*LVCN**2 = 1.560E-10 WATT/ELECT.   TOTAL POWER = 1.6.5E-10   100.00

DISTRIBUTION FUNCTION CONVERGED !!! .T SECONDS AFTER 6 ITERATIONS, WITH A RELATIVE CHANGE BETWEEN SUCCESSIVE ITERATIONS LESS THAN 2.463E-03, AND A POWER BALANCE ACCURACY DEFINED BY 100*(E*MU*EVCH**2/POWER-1) = -5.73 %. ADDITIONAL TIME REQUIRED FOR CALCULATION OF PLASMA PARAMETERS, AND GENERATION OF TABLES AND PLOTS = .74 SEC. NET ELECTRON-ELECTRON POWER TRANSFER DISCREPANCY = -3.253E-13 WATT/ELECTRON = -.20 % OF POWER.

DR. WILLIAN B. LACINA, 10/21/77
NORTHROP RESEARCH AND TECHNOLOGY

Figure 43.   Plasma Kinetics Analysis

TIME T = 5.000E-07 SEC

POPULATION DENSITIES AND RATES OF CHANGE

ELECTRICAL AND OPTICAL PARAMETERS

I	SPECIES NAME	E(I) (EV)	N(I) (CM-3)	DN(I)/DT (CM-3/SEC)
1	RAO	0.00	1.271E+14	1.229E+20
2	E(-)	0.00	2.683E+14	-7.292E+19
3	AR	0.00	3.830E+19	-1.274E+20
4	AR*	11.50	1.138E+14	1.546E+20
5	KR	0.00	3.214E+18	-9.052E+20
6	KR*	9.90	2.235E+14	4.155E+20
7	AR**	13.50	3.437E+12	-1.111E+20
8	KR**	11.50	7.334E+12	-1.881E+20
9	AR(+)	15.80	3.617E+13	1.622E+19
10	KR(+)	14.40	8.699E+13	7.115E+19
11	AR2(+)	13.00	4.533E+12	3.583E+18
12	KR2(+)	11.80	1.858E+14	1.441E+20
13	F2	0.00	3.256E+16	-3.206E+22
14	F	0.00	3.115E+16	6.375E+22
15	F-	.01	5.900E+13	3.251E+20
16	AR2*	9.50	5.918E+12	5.249E+18
17	KR2*	8.20	9.961E+13	9.313E+19
18	ARKR(+)	12.40	1.382E+13	1.720E+19
19	ARKR*	8.80	1.044E+13	1.510E+19
20	ARF*	6.50	4.260E+12	8.781E+17
21	AR2F*	5.00	5.222E+12	1.320E+18
22	KRF*	5.00	1.980E+13	-3.363E+18
23	KR2F*	3.00	9.724E+13	5.159E+19
24	ARKRF*	4.00	6.082E+12	1.606E+17

PARAMETER		VALUE	UNITS
JBEAM	=	8.28	AMP/CM2
DEPOSITION	=	2.00	
ENERGY	=	320.	KEV
DVOX	=	11.22	KV/CM
P(BEAM)	=	92.94	KW/CM3
R(EXT)	=	0.00	OHM
L(EXT)	=	2.000E-07	HENRY
C(EXT)	=	1.330E-06	FARAD
AREA	=	2000.00	CM2
OIST	=	10.00	CM
CONDUCT	=	2.538E-02	/OHM/CM
R(OISCH)	=	1.970E-01	OHM
Q	=	3.362E-02	COULOMB
I(OISCH)	=	6.602E+04	AMP
J(OISCH)	=	3.301E+01	AMP/CM2
E.US	=	.301	KVOLT/CM
ESUS*JSUS	=	42.94	KW/CM3
O/C	=	25.282	KVOLT
V(OISCH)	=	13.007	KVOLT
L*DI/DT	=	12.274	KVOLT
REFLECT	=	70.00	%
LOSS	=	0.00	%/PASS
T(CAVITY)	=	24.3	NS
L(CAVITY)	=	130.00	CM
LENGTH	=	75.00	CM
OMEGA/4/PI	=	1.177E-04	
THRESH	=	2.378E-03	CM-1
NET GAIN	=	2.434E-03	CM-1
LASER GAIN	=	3.959E-03	CM-1
ABSORPTION	=	1.525E-03	CM-1
INTENSITY	=	3.054E+06	WATT/CM2
OPTICAL	=	7.43	KW/CM3
EFFICIENCY	=	5.47	%
STEP SIZE	=	1.072E-09	SEC
T(EXTRAP)	=	4.997E-07	SEC
ORDER	=	1	

DR. WILLIAM B. LACINA, 10/21/77
NORTHROP RESEARCH AND TECHNOLOGY

Figure 44. Population Densities and Rates of Change
Electrical and Optical Parameters

PERCENTAGE CONTRIBUTION OF REACTION K TO DN(I)/DT, EXPRESSED (FOR EACH SPECIES)
AS A PERCENTAGE OF THE MAXIMUM RATE OCCURING FOR ALL REACTIONS INCLUDED

TIME T = 5.000E-07 SEC

K	RATE(K)	MAX %	RAD	E(I-)	AR	AR*	KR	KR*	AR**	KR**	AR(+)	KR(+)
1	3.021E+21	21.1			-13.823	21.149						
2	4.954E+21	32.8					-32.812	16.150				
3	4.440E+18	.0			-.020		-					
4	5.807E-18	.0					-.038		.031	.019		
5	1.427E+22	99.9				-99.872			99.872			
6	3.068E+22	100.0						-100.000		100.000		.019
7	0.	0.0										
8	2.589E+18	0.0		.012			-.017					
9	8.222E+20	5.8		3.943		-5.756		-6.120			4.786	13.561
10	1.877E+21	13.6		9.002								
11	9.727E+19	.7		.466					-.681		.566	
12	3.901E+20	2.8		1.871						-1.272		2.818
13	5.560E+19	.5		-.267	.254	.389						
14	3.419E+21	24.0		-16.395			22.646	11.146				
15	2.085E+22	100.0		-100.000								
16	1.588E+20	8.8			1.453							
17	2.673E+21	79.6		82.382			35.409				100.000	
18	1.718E+22	100.0			-78.613							
19	4.909E+21	34.4			-22.461	34.365						
20	2.671E+21	19.3		12.810			-17.693	2.491				19.296
21	7.642E+20	5.1			-52.681		-5.061					
22	1.151E+22	100.0									-67.013	
23	1.208E+21	8.5					-8.000				-7.031	
24	2.709E+21	20.1					-18.471					-20.144
25	1.384E+22	100.0			-63.349							-100.000
26	3.408E+21	25.2			15.959		-23.100				-20.301	25.193
27	1.093E+22	100.0			100.000		-72.372					78.928
28	1.422E+22	100.0			65.065	-12.585	-94.177					
29	1.812E+20	100.0			-8.291	-1.065						
30	1.521E+20	4.3					-1.007	-5.353				
31	1.642E+21	48.9			-16.277		-10.876	-11.596				
32	3.557E+21	100.0			15.360							
33	3.357E+21	100.0			.612		-22.233					
34	1.337E+20	4.8										
35	1.337E+20	4.9										
36	2.134E+21	76.8									-12.422	
37	5.482E+21	38.6					36.310					
38	5.482E+21	84.2										
39	5.133E+21	37.1										-37.073
40	4.078E+20	2.9			1.866							
41	4.078E+20	20.9										
42	5.240E+20	34.7						-17.081				
43	2.780E+21	100.0			10.381	-19.462						
44	2.269E+21	15.9			-8.649	-15.883	-15.926	7.396				
45	1.890E+21	96.7					-8.757					
46	1.322E+21	20.3										
47	2.712E+21	100.0			-12.410							
48	5.691E+19	2.9					-.377					
49	1.522E+21	84.0			13.927		-10.079	4.961				
50	1.051E+16	.0		.000	.000							

* THIS REACTION CONTRIBUTES LESS THAN 5. % 10 ALL SPECIES THROUGHOUT THE ENTIRE CALCULATION SO FAR

Figure 45.   Percentage Contribution of Reaction K to DN(I)/DT

PERCENTAGE CONTRIBUTION OF REACTION K   TIME 1 = 5.1000E-17 SEC. EXPRESSED (FOR EACH SPECIES)
AS A PERCENTAGE OF THE MAXIMUM RATE OCCURING FOR ALL REACTIONS INCLUDED

K	RATE(K)	MAX %	RAD	E(-)	AR	AR*	KR	KR*	AR**	KR**	AR(+)	KR(+)
51	2.054E-21	71.9			9.399		-13.604					
52	5.531E-19	3.1			.253							
• 53	9.310E-20	27.7					6.166					
54	4.817E-19	2.7										
55	2.040E-20	5.7			.934							
56	1.020E-20	5.2										
57	9.730E-20	29.0			1.556							
58	1.700E-20	6.3			.906		1.311					
59	1.980E-20	10.1					41.936					
60	3.166E-21	48.6					-12.947					
61	1.955E-21	100.0			8.945		4.269					
62	6.445E-20	4.3										
• • 63	1.387E-20	5.0			.635							
64	1.678E-21	61.9			15.359	100.000	-11.116					
65	1.420E-22	100.0						99.360				
66	3.040E-22	99.4							-100.000	-99.360		
67	1.406E-20	5.1			.643							
• 68	2.249E-19	1.2			.206							
• • 69	3.133E-19	.9			.143		.208					
70	3.287E-20	9.8					4.354					
71	1.044E-21	38.5			9.557							
72	3.041E-20	15.6			1.391		2.014					
73	6.515E-21	100.0					86.296					
74	2.177E-21	14.4					14.421					
75	1.510E-22	100.0	100.000				100.000					
76	1.863E-21	17.9	-12.336									
77	1.215E-21	8.0	-8.048	5.027								
• • 78	3.700E-61	.0	-.000			.000	.000					
• • 79	2.593E-20	2.3	-1.717		1.187		16.429				1.509	
80	2.481E-21	17.9	-16.429									17.917

• THIS REACTION CONTRIBUTES LESS THAN 5. % TO ALL SPECIES THROUGHOUT THE ENTIRE CALCULATION-SO FAR

Figure 45 (continued)

PERCENTAGE CONTRIBUTION OF REACTION K TO DN(I)/DT, EXPRESSED (FOR EACH SPECIES)
AS A PERCENTAGE OF THE MAXIMUM RATE OCCURING FOR ALL REACTIONS INCLUDED

TIME T = 5.000E-07 SEC

K	RATE(K)	MAX %	AR2(·)	KR2(·)	F2	F	F-	AR2*	KR2*	ARKR(·)	ARKR*	AKR*
1	3.021E-21	21.1										
2	4.954E-21	32.8										
3	4.440E-18	.0										
4	5.807E-18	.0										
5	1.427E-22	99.9										
6	3.068E-22	100.0										
7	0.	0.0										
8	2.589E-18	5.8										
9	8.222E-20	5.8										
10	1.877E-21	13.6										
11	9.727E-19	.7										
12	3.901E-20	2.8										
13	5.560E-19	.5										
14	3.419E-21	24.0	-.483	-24.046								
15	2.085E-22	100.0			-100.000	100.000						
16	1.508E-20	8.6				100.000		-8.765				
17	2.673E-21	79.6							-79.632			
18	1.718E-22	100.0										
19	4.909E-21	34.4										
20	2.671E-21	19.3										
21	7.642E-20	5.1										
22	1.151E-22	100.0	100.000									
23	1.208E-21	8.5		19.613								
24	2.789E-21	24.1								8.495		
25	1.384E-22	100.0								97.363		
26	1.488E-21	25.2										
27	1.093E-22	100.0	-94.911									
28	1.422E-22	100.0		100.000				100.000		-100.000		
29	1.812E-21	100.0						100.000				
30	1.521E-20	4.3									4.275	
31	1.642E-21	48.9							48.919			
32	3.557E-21	100.0							100.000		100.000	
33	3.357E-21	100.0									-94.367	
34	1.337E-20	4.8	-1.161				-.641					
35	1.337E-20	4.9	-1.161				-.641					
36	2.134E-21	76.8					-10.233					4.810
37	5.482E-21	38.6		-38.555			-26.288					
38	5.482E-21	84.2		-38.555			-26.288					76.767
39	5.133E-21	37.1					-24.611					
40	4.078E-20	2.9					-1.956			-2.868		
41	4.078E-20	20.9					-1.956			-2.868		
42	5.240E-21	34.7			-25.124	25.124						
43	2.780E-21	100.0			-13.330	13.330						100.000
44	2.269E-21	15.9										
45	1.890E-21	96.7										
46	1.322E-21	20.3										
47	2.712E-21	100.0										
48	5.691E-19	2.9										
49	1.522E-21	84.0	.000					-83.991				-97.556
50	1.051E-16	.0						-.001				-2.047

* THIS REACTION CONTRIBUTES LESS THAN 5. % TO ALL SPECIES THROUGHOUT THE ENTIRE CALCULATION SO FAR
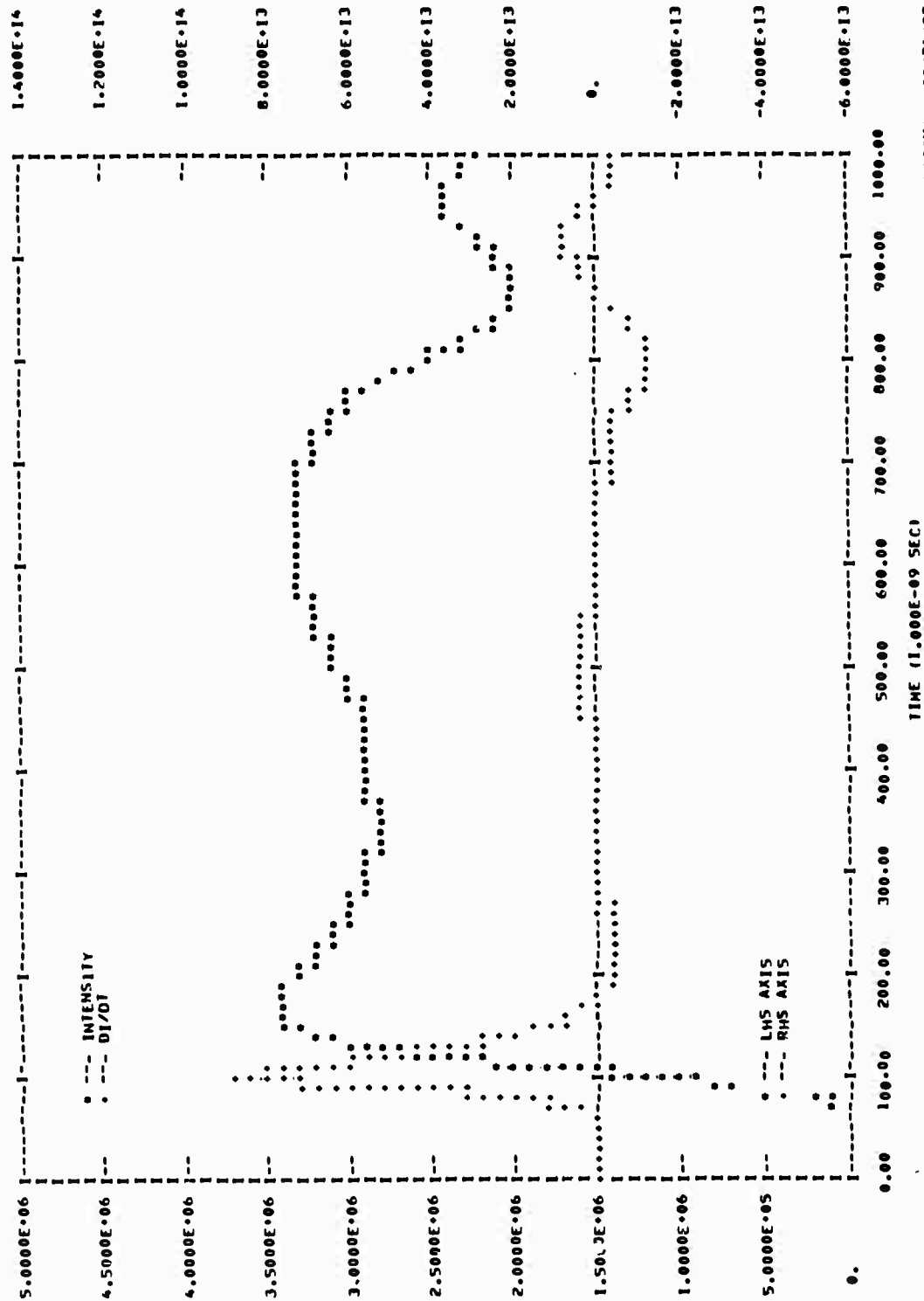
Figure 45 (continued)

109

PERCENTAGE CONTRIBUTION OF REACTION K TO DN(I)/DT, EXPRESSED (FOR EACH SPECIES)
AS A PERCENTAGE OF THE MAXIMUM RATE OCCURING FOR ALL REACTIONS INCLUDED

TIME T = 5.000E-07 SEC

K	RATE(K)	MAX %	AR2(*)	KR2(*)	F2	F	F-	AR2*	KR2*	ARKR(*)	ARKR*	ARF*
1	3.021E-21	21.1										
2	4.954E-21	32.8										
3	4.440E-18	.0										
4	5.807E-18	99.9										
5	1.427E-22	100.0										
6	3.068E-22	0.0										
7	0.	0.0										
8	2.589E-18	.0										
9	8.222E-20	5.8										
10	1.877E-21	13.6										
11	9.727E-19	.7										
12	3.901E-20	2.0										
13	5.560E-19	.5										
14	3.419E-21	24.0	-.483									
15	2.085E-22	100.0		-24.046	-100.000	100.000						
16	1.588E-20	8.8					100.000		-79.632			
17	2.673E-21	79.6						-8.765				
18	1.718E-22	100.0										
19	4.909E-21	34.4										
20	2.671E-21	19.3										
21	7.642E-20	5.1										
22	1.151E-22	100.0	100.000									
23	1.208E-21	8.5		19.613						0.495		
24	2.789E-21	20.1								97.363		
25	1.384E-22	100.0										
26	3.408E-21	25.2										
27	1.093E-22	100.0										
28	1.422E-22	100.0	-94.911	100.000						-100.000		
29	1.812E-21	100.0						100.000				
30	1.521E-20	4.3									4.275	
31	1.642E-20	48.9							48.919			
32	3.557E-21	100.0							100.000		100.000	
33	3.357E-21	100.0									-94.367	
34	1.337E-20	4.0	-1.161				-.641					4.010
35	1.337E-20	4.9	-1.161				-.641					76.767
36	2.134E-21	76.8					-10.233					
37	5.402E-21	38.6		-38.555			-26.288					
38	5.402E-21	84.2		-30.555			-26.288					
39	5.133E-21	37.1					-24.611					
40	4.078E-20	2.9					-1.956			-2.068		
41	4.078E-20	20.9					-1.956			-2.860		
42	5.240E-21	34.7			-25.124	25.124						
43	2.780E-21	100.0			-13.330	13.330						100.000
44	2.269E-21	15.9										
45	1.890E-21	96.7										
46	1.322E-21	20.3										
47	2.712E-21	100.0										
48	5.691E-19	2.9	.000									
49	1.522E-21	84.0						-83.991				-97.556
50	1.051E-16	.0						-.001				-2.047

* THIS REACTION CONTRIBUTES LESS THAN 5. % TO ALL SPECIES THROUGHOUT THE ENTIRE CALCULATION SO FAR

Figure 45 (continued)

PERCENTAGE CONTRIBUTION OF REACTION K TO DN(11)/DT, EXPRESSED (FOR EACH SPECIES)
AS A PERCENTAGE OF THE MAXIMUM RATE OCCURING FOR ALL REACTIONS INCLUOED

K	RATE(K)	MAX %	AR2F*	KRF*	KR2F*	ARKRF*
1	3.021E+21	21.1				
2	4.954E+21	32.8				
* 3	4.440E+18	.0				
* 4	5.807E+18	.0				
5	1.427E+22	99.9				
6	3.068E+22	100.0				
* 7	0.	0.0				
* 8	2.5H9E+18	.0				
9	8.222E+20	5.8				
10	1.877E+21	13.6				
* 11	9.727E+19	.7				
* 12	3.901E+20	2.8				
* 13	5.560E+19	.5				
14	3.419E+21	24.0				
15	2.085E+22	100.0				
16	1.588E+20	8.8				
17	2.673E+21	79.6				
18	1.718E+22	100.0				
19	4.909E+21	34.4				
20	2.671E+21	19.3				
21	7.642E+20	5.1				
22	1.151E+22	100.0				
23	1.2C 21	8.5				
24	2.784E+21	20.1				
25	1.384E+22	100.0				
26	3.488E+21	25.2				
27	1.093E+22	100.0				
28	1.422E+22	100.0				
29	1.812E+21	100.0				
* 30	1.521E+20	4.3				
31	1.642E+21	48.9				
32	3.557E+21	100.0				
33	3.357E+21	100.0				
* 34	1.337E+20	4.8				
* 35	1.337E+20	4.9	4.931			
36	2.134E+21	76.8				
37	5.482E+21	38.6		36.310		
38	5.482E+21	84.2			84.152	
39	5.133E+21	37.1		33.993		
* 40	4.078E+20	2.9		2.701		
41	4.078E+20	20.9				20.864
42	5.240E+21	34.7		34.703		
43	2.780E+21	100.0				
44	2.269E+21	15.9				
45	1.890E+21	96.7		-12.519		96.700
46	1.322E+21	20.3		-8.757	20.295	
47	2.712E+21	100.0	100.000			
* 48	5.691E+19	2.9				2.911
49	1.522E+21	84.0				
* 50	1.051E+16	.0				

* THIS REACTION CONTRIBUTES LESS THAN 5. % TO ALL SPECIES THROUGHOUT THE ENTIRE CALCULATION SO FAR

Figure 45 (continued)

TIME T = 5.000E-07 SEC
PERCENTAGE CONTRIBUTION OF REACTION K TO DN(I)/DT, EXPRESSED (FOR EACH SPECIES)
AS A PERCENTAGE OF THE MAXIMUM RATE OCCURING FOR ALL REACTIONS INCLUDED

K	RATE(K)	MAX %	AR2F*	KRF*	KR2F*	ARKRF*
51	2.054E+21	73.9		13.604		
• 52	5.531E+19	3.1				
53	9.310E+20	27.7		6.166		
• 54	4.817E+19	2.7	1.776			
55	2.040E+20	5.7		1.351		
56	1.020E+20	5.2				5.218
57	9.730E+20	29.0			14.936	
58	1.700E+20	6.3	-6.269			
59	1.980E+20	10.1				-10.130
60	3.166E+21	48.6			-48.596	
61	1.955E+21	100.0			30.005	-100.000
• 62	6.445E+20	4.3		-4.269		
• 63	1.387E+20	5.0				
64	1.678E+21	61.9	-61.884	11.116		
65	1.428E+22	100.0				
66	3.048E+22	99.4				
67	1.406E+20	5.1				
• 68	2.249E+19	1.2				
• 69	3.133E+19	.9				
70	3.287E+20	9.8				
71	1.044E+21	38.5	-38.506			
72	3.041E+20	15.6				-15.556
73	6.515E+21	100.0			-100.000	
74	2.177E+21	14.4		-14.421		
75	1.510E+22	100.0		-100.000		
76	1.863E+21	17.9				
77	1.215E+21	8.0				
• 78	3.708E-61	.0			-.000	
• 79	2.593E+20	2.3				
80	2.481E+21	17.9				

• THIS REACTION CONTRIBUTES LESS THAN 5. % TO ALL SPECIES THROUGHOUT THE ENTIRE CALCULATION SO FAR

Figure 45 (continued)

E-BEAM CURRENT DENSITY (AMP/CM2) AS A FUNCTION OF TIME
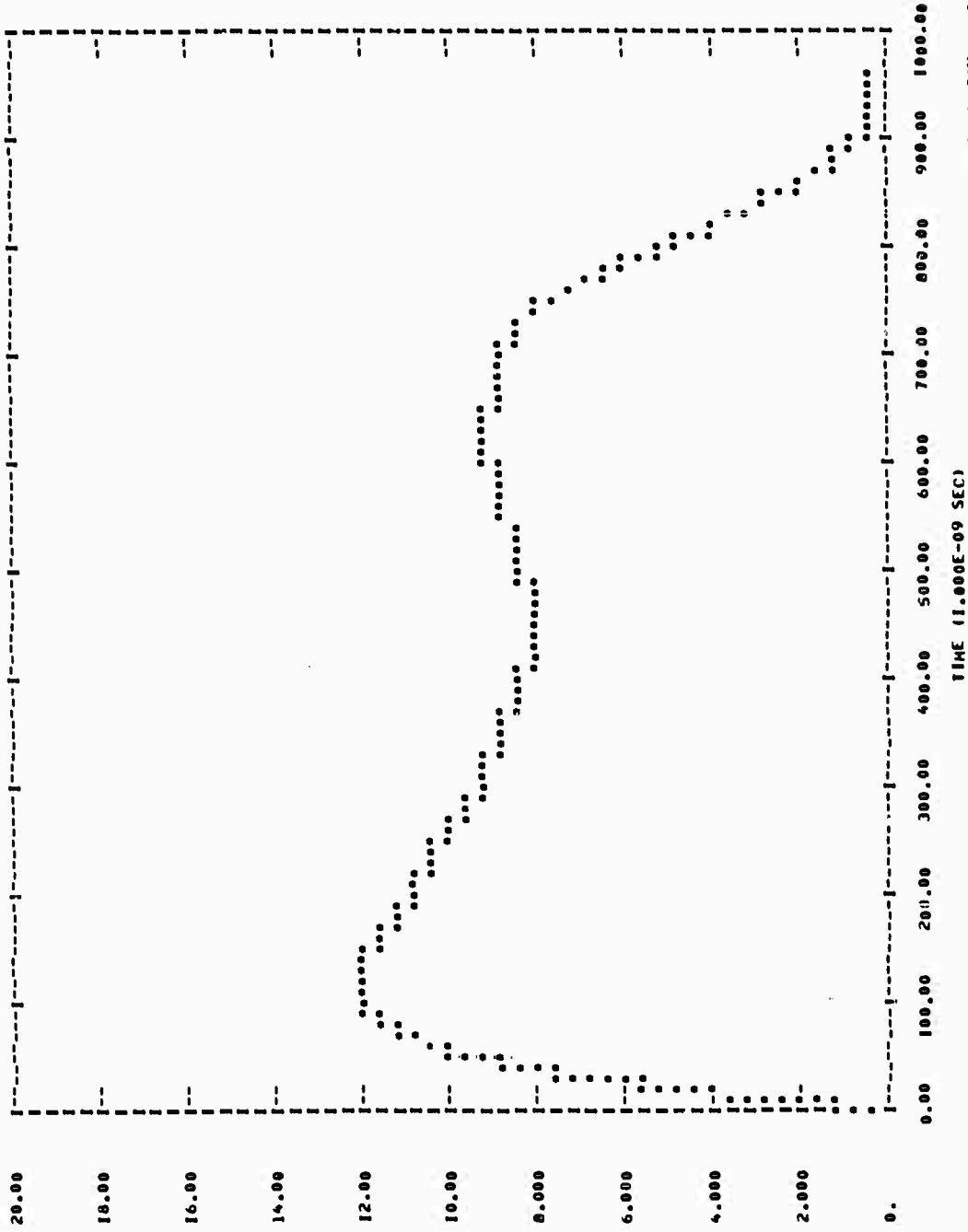
Figure 46. E-Beam Current Density as a Function of Time

DR. WILLIAM B. LACINA, 10/21/77
NORTHROP RESEARCH AND TECHNOLOGY

TIME (1.000E-09 SEC)

Figure 47. Intracavity Radiation Intensity

114
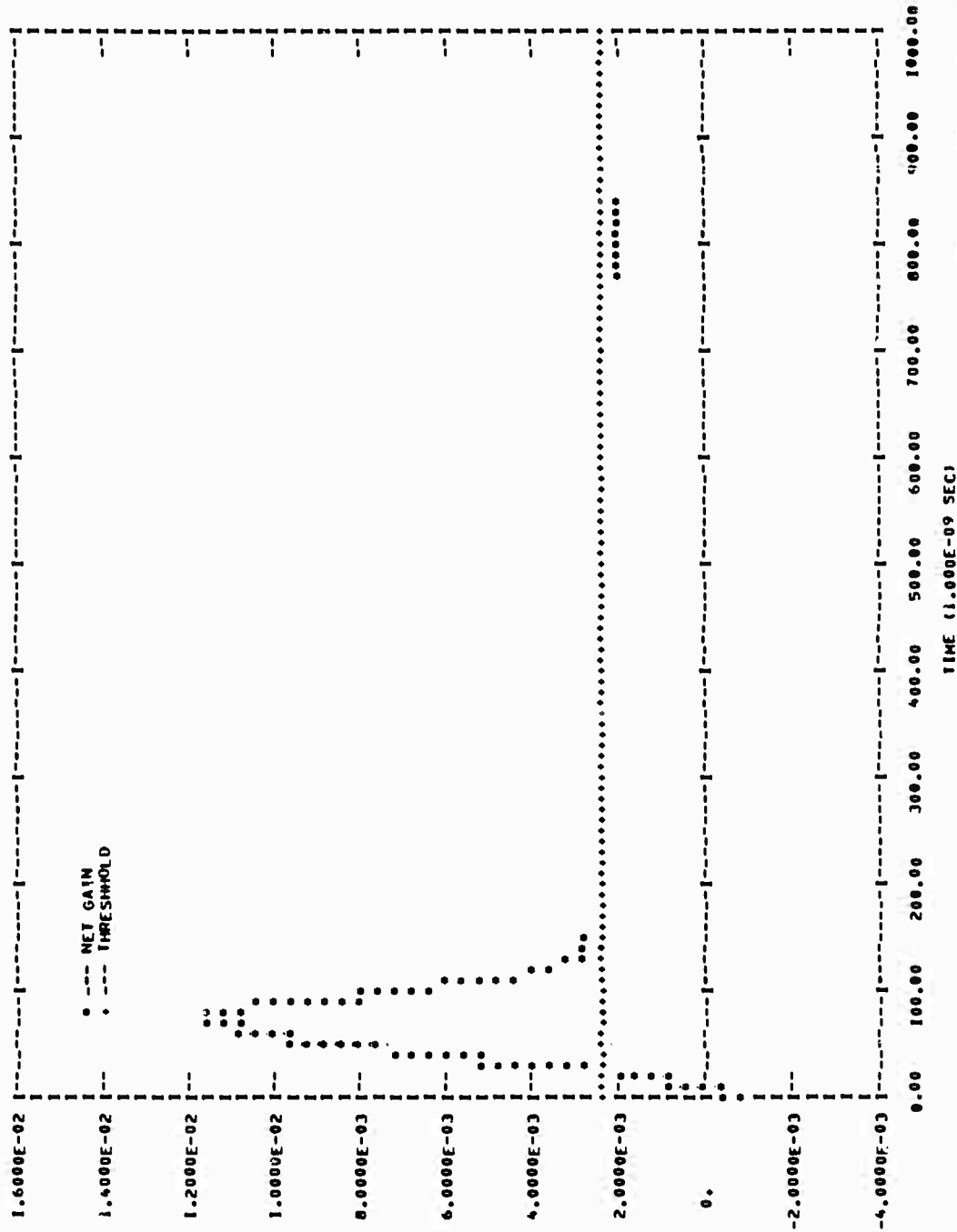
Figure 48. Instantaneous Net Gain Coefficient

115

Figure 49. Laser Gain and Medium Absorption Coefficients

116

POWER DENSITY (WATT/CM3)
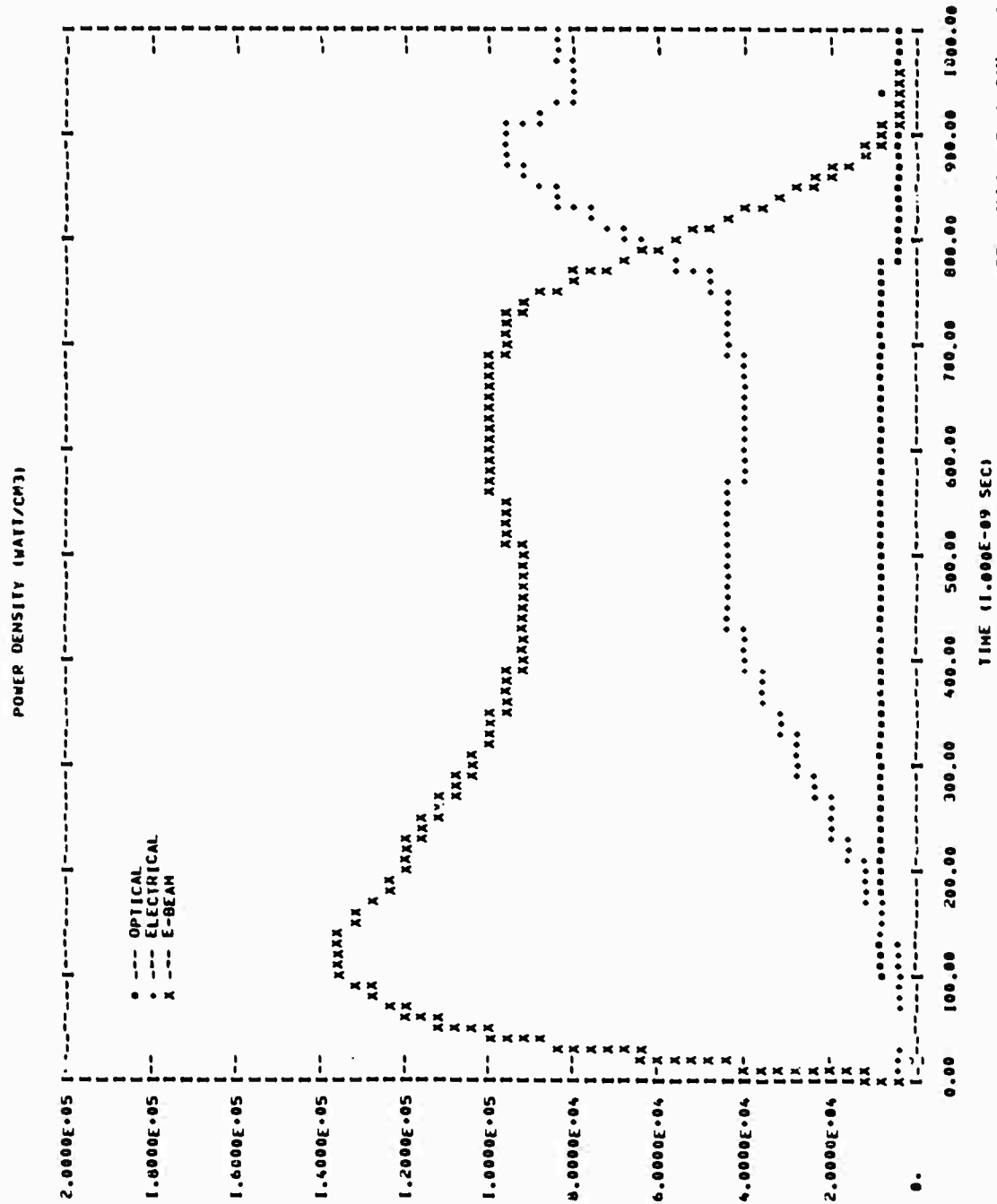
Figure 50. Power Density

DR. WILLIAM B. LACINA. 10/21/77
NORTHROP RESEARCH AND TECHNOLOGY

117
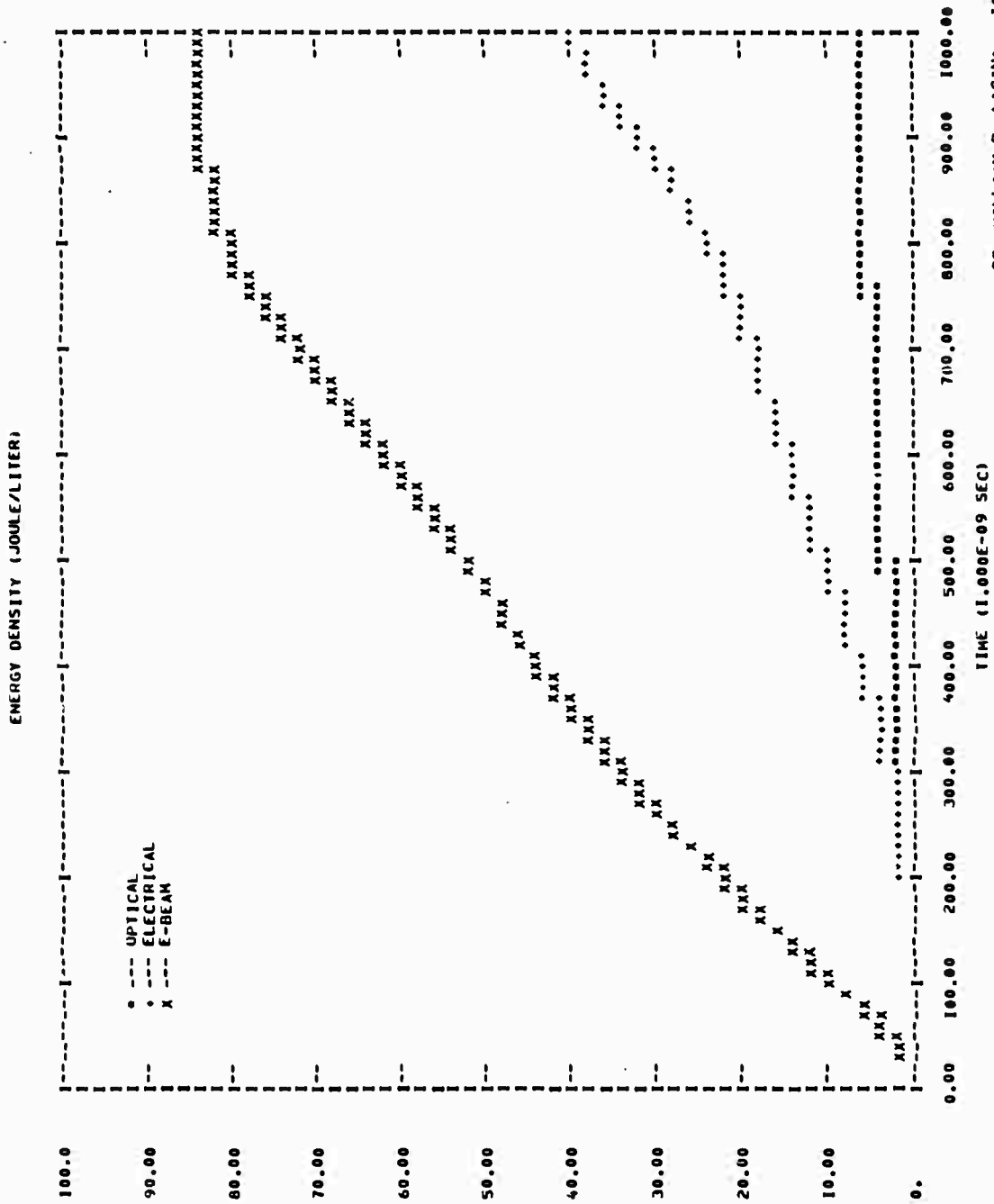
Figure 51. Energy Density

ENERGY DENSITY (JOULE/LITER)

DR. WILLIAM B. LACINA, 10/21/77
NORTHROP RESEARCH AND TECHNOLOGY

118
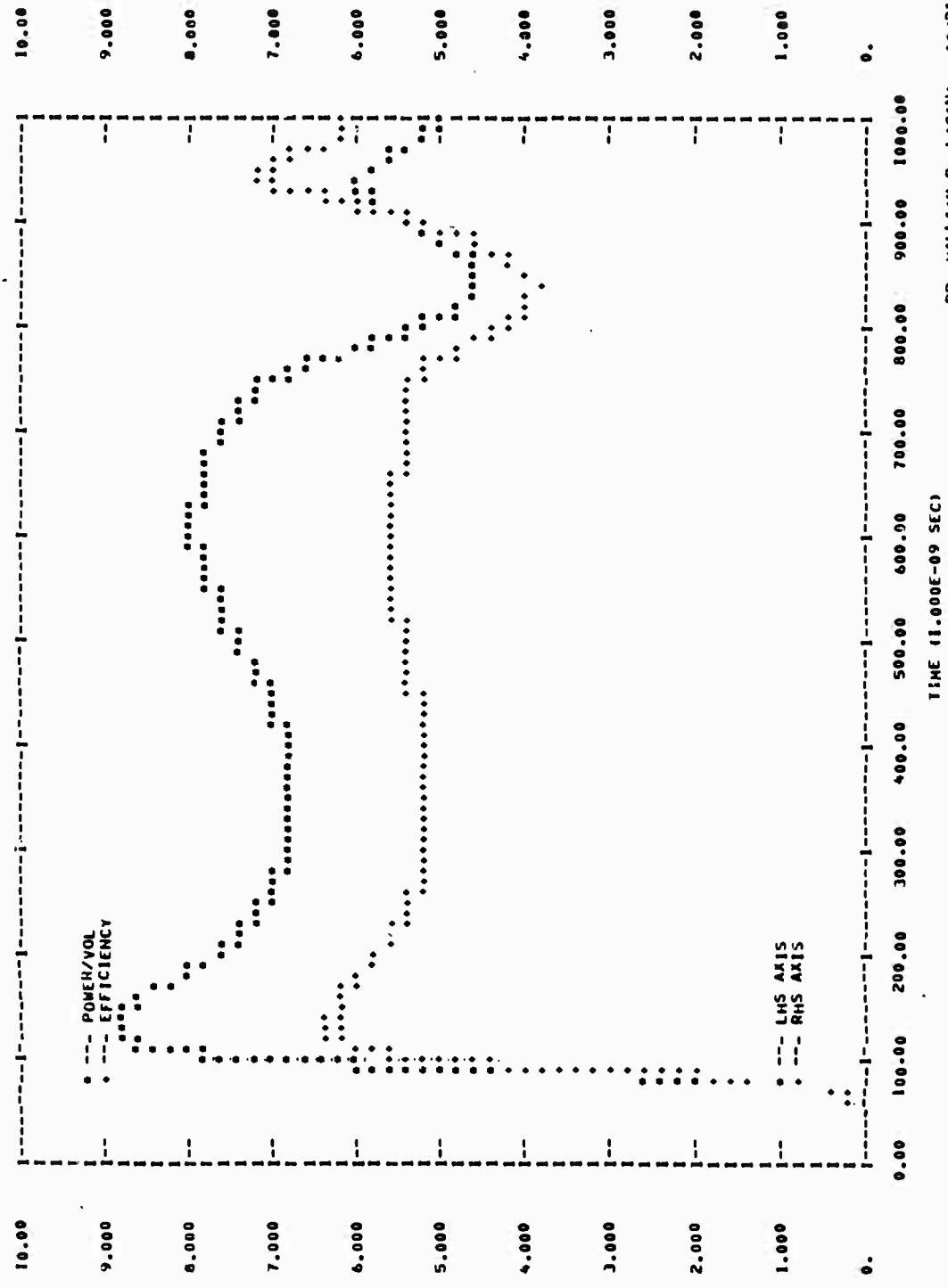
OPTICALLY EXTRACTED POWER DENSITY (KW/CM3) AND EFFICIENCY (%)

Figure 52   Optically Extracted Power Density and Efficiency

119
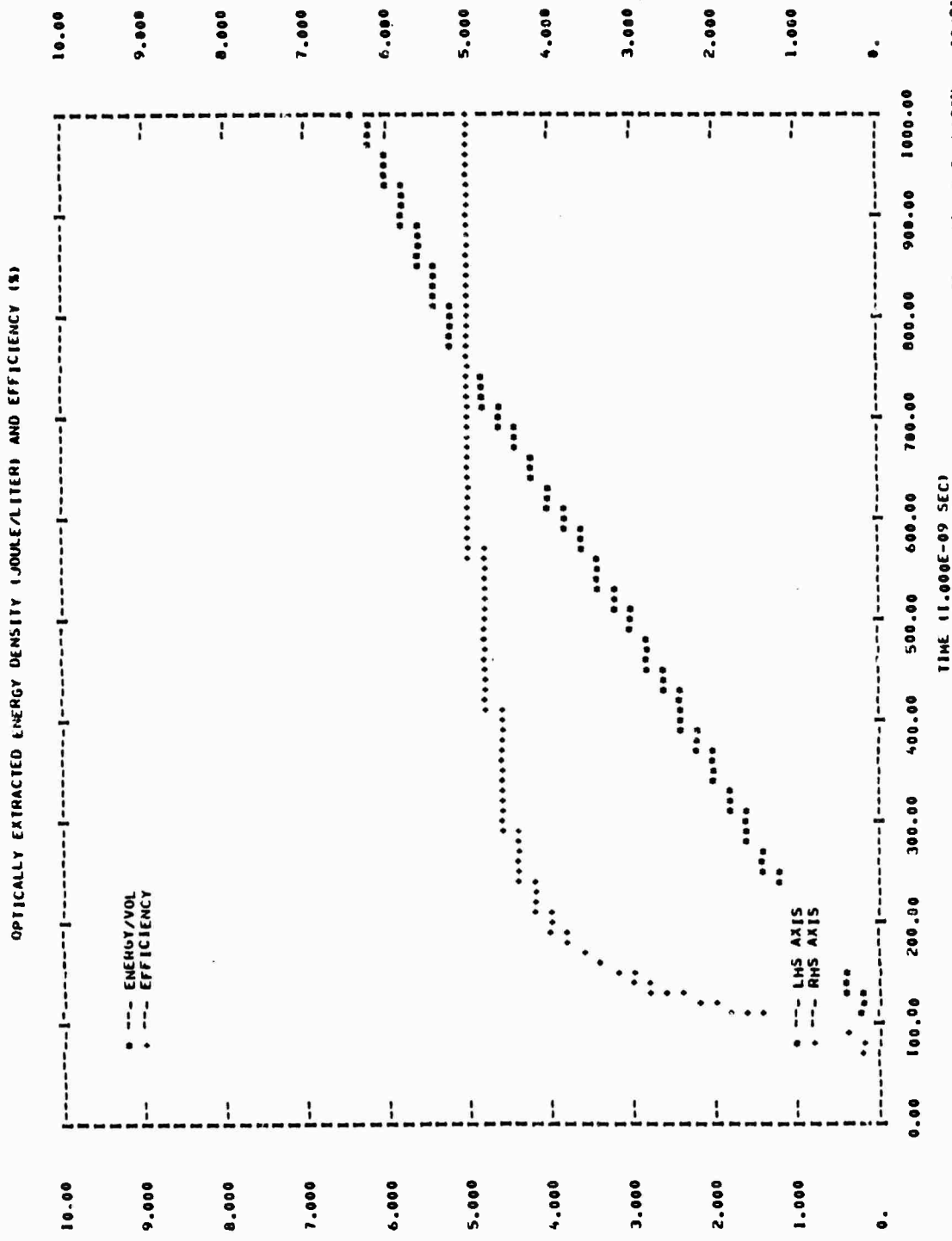
OPTICALLY EXTRACTED ENERGY DENSITY (JOULE/LITER) AND EFFICIENCY (%)

Figure 53. Optically Extracted Energy Density and Efficiency

120
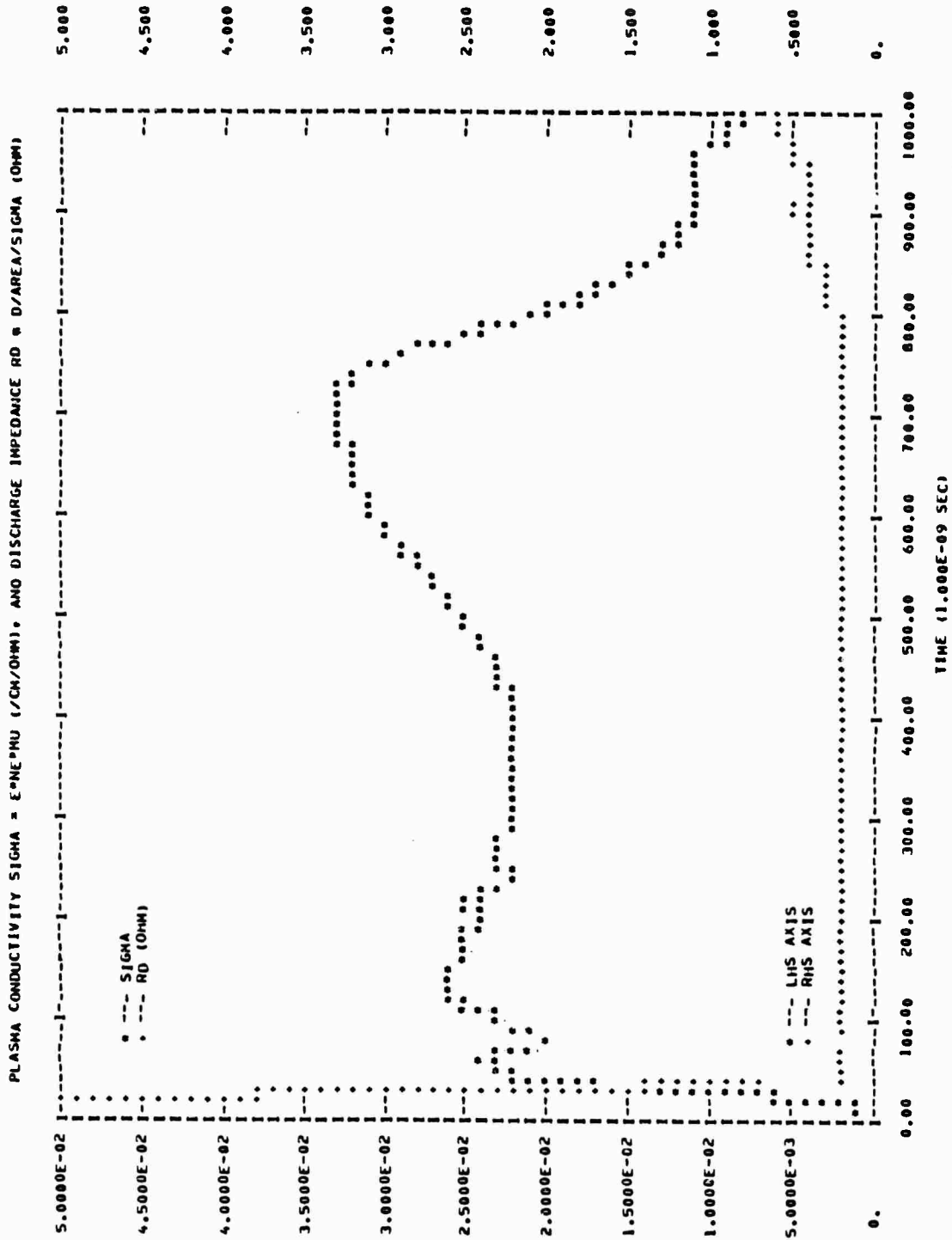
Figure 54. Plasma Conductivity and Discharge Impedance

121
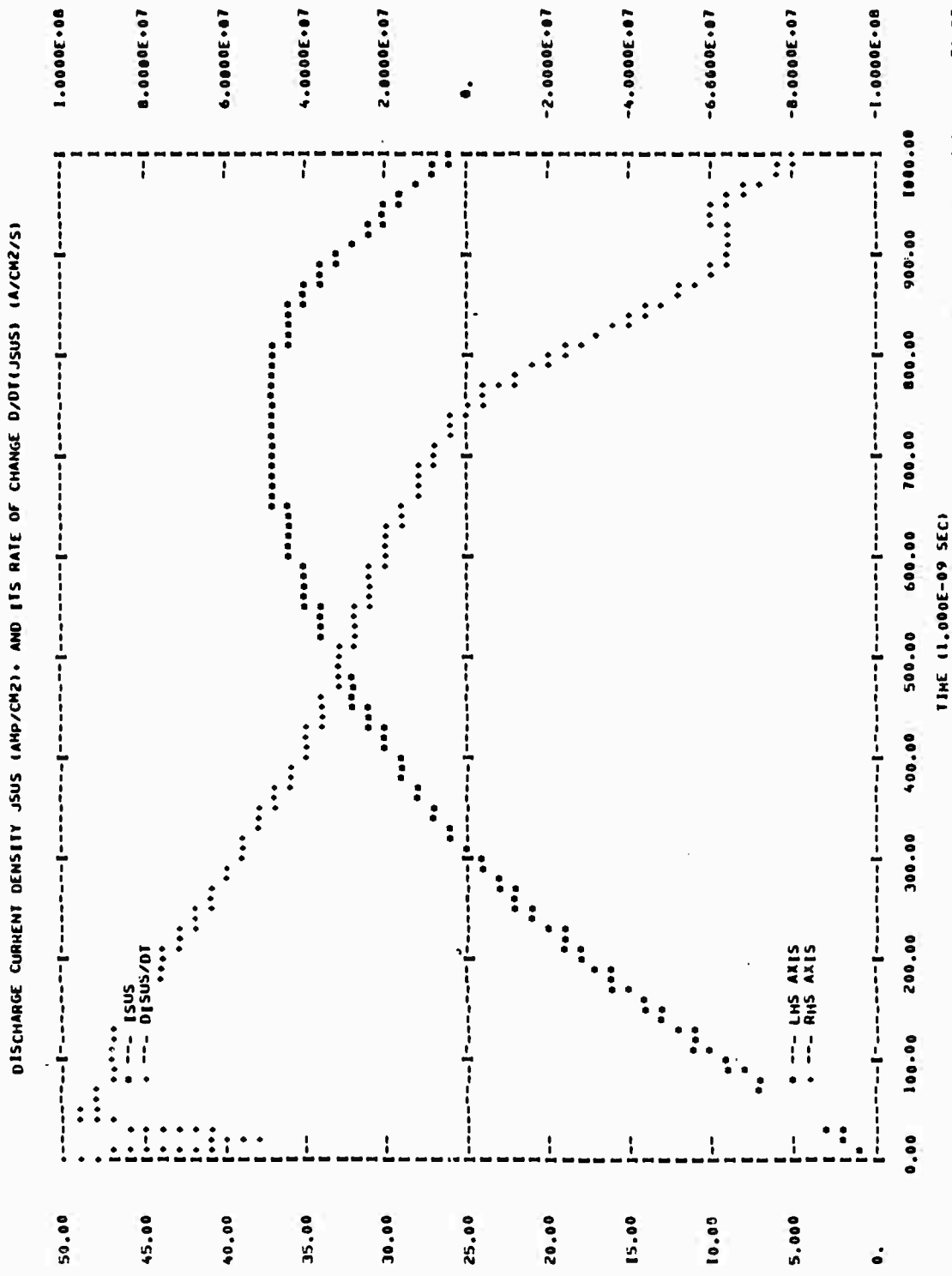
Figure 55. Discharge Current Density and its Rate of Change
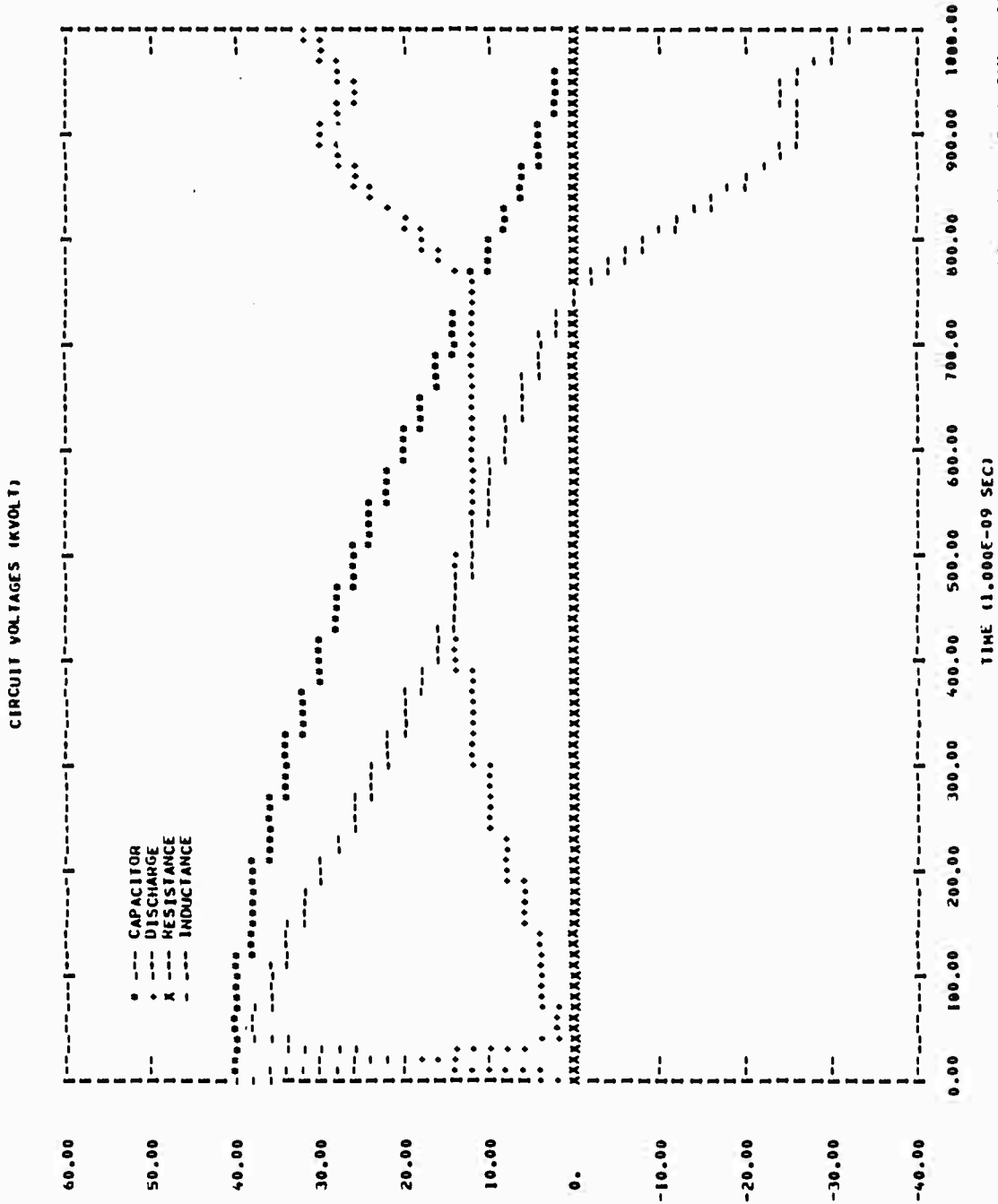
CIRCUIT VOLTAGES (KVOLT)

Figure 56. Circuit Voltages

DR. WILLIAM B. LACINA. 10/21/77
NORTHROP RESEARCH AND TECHNOLOGY

123
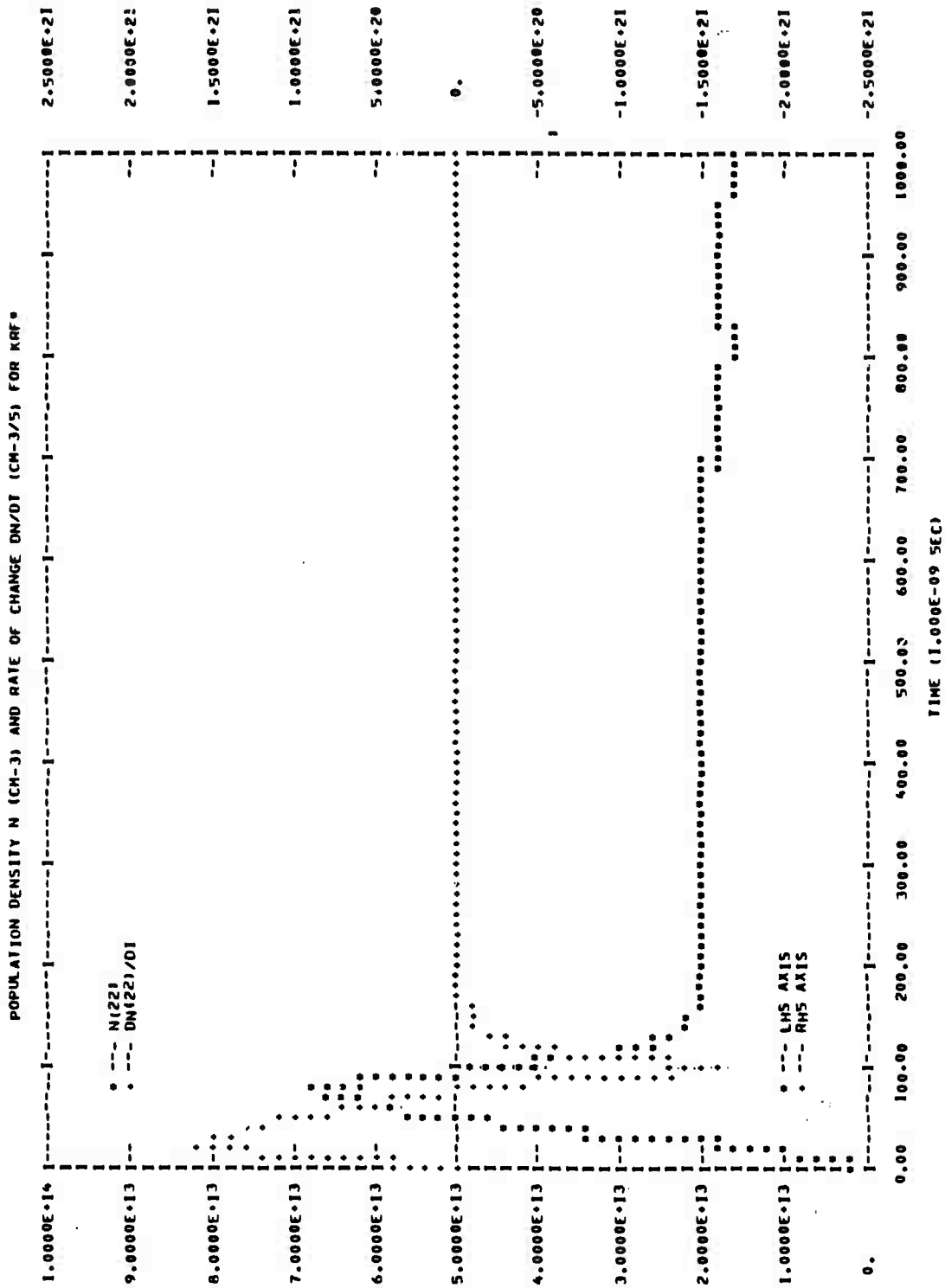
Figure 57. Population Density and Rate of Change for KrF*

124

4. EXPERIMENTAL RESULTS AND THEORETICAL CORRELATION

This section contains a detailed presentation of experimental results and a discussion of device characteristics which limited the accessible range of experimental parameters. Comparisons of these results with the theoretical model has been undertaken and the correlation has been generally good in all essential details. Results of a sample comparison are presented. In addition, an analysis is presented which attempts to explain limitations in the experimental results based on nonuniformity in electron beam energy deposition. Finally, a theoretical extrapolation is presented assuming optimistic device characteristics.

The experimental results fall basically into two classes dictated by the electron beam deposition uniformity. The first class deals with laser extraction over small volumes with the discharge anode placed 3-5 cm from the ground plane screen. In this case, total energy output was sacrificed in an attempt to determine discharge stability limits and enhancement with reasonable beam deposition uniformity over short distances. In the second case, the discharge anode-cathode separation was set at its extreme value of 10 cm with the intent of extracting maximum energy at the expense of discharge enhancement. In both instances of small and large anode-cathode separations, for e^--beam pumping alone, the total energy output was found to be proportional to electron beam current density, whereas energy enhancement with the addition of a discharge was found to be roughly inversely proportional to this parameter. Here, enhancement is defined as the ratio of laser energy output with electron beam plus discharge excitation to laser energy output with electron beam excitation only. Under optimum operating conditions with a 900 ns electron gun pulse length, the maximum extracted specific energy was 22 J/liter for a 3 liter volume with an enhancement of 1.22 and beam current of 18 A/cm^2. Total extracted energy at this current level was 90 J over 10 liters. For a reduced beam current density of 10 A/cm^2,

125

specific extraction was likewise reduced to 8 J/liter with, however, a corresponding increase in enhancement to 1.8. The relatively low enhancement factors are shown below to be a direct result of discharge instability induced by nonuniform beam deposition in the direction of propagation.

4.1 Experimental Results. The experimental results are presented sequentially in four basic groups: a qualitative description of beam uniformity, resulting laser output patterns and discharge profiles; an analysis of typical waveforms for the KrF and XeF systems; a detailed outline of parametric studies to determine nominal operating conditions; and a summary of results under optimum conditions.

The question of electron beam deposition was fundamental to the experimental results and has been detailed in Section 2.1. However, a graphic representation would be helpful here and is shown in Figure 58. The photograph is an end view of the device looking down the optical axis and shows simply total fluorescence generated by the electron beam propagating from left to right into 2 atm of Argon. The anode was drawn back 15 cm and can be distinguished by the slight line reflection at the right side of the photograph. The gun cathode in this case was of the high current density variety with a 20 cm width. The extent of maximum beam fluorescence is about 17 cm in the transverse direction and about 10 cm in the direction of propagation.

A typical laser output burn pattern on polaroid film is shown in Figure 59 for electron beam excitation only, and correspondence with the previous measurement of energy deposition uniformity is apparent. Energy density decreases from the center outward with the dark, oval center section containing the highest density and the surrounding light halo about 1/3 as much. At the border of this second area is a third, faintly discernible in the photograph,

126
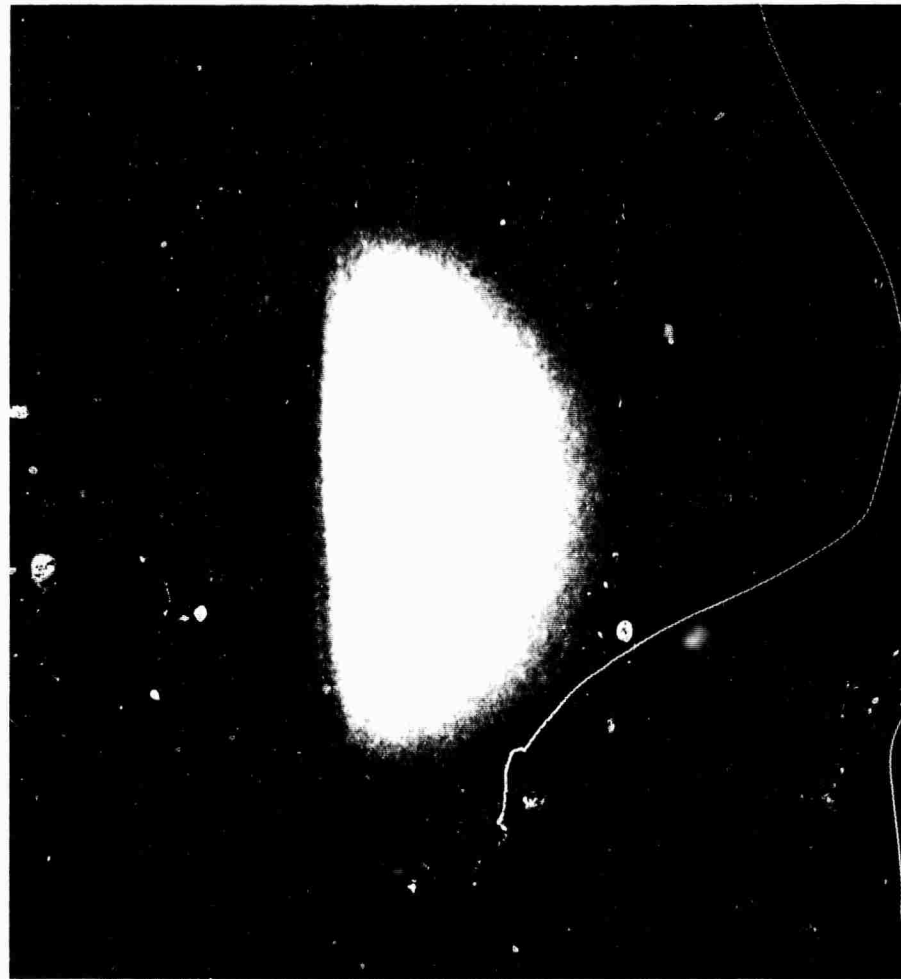
15 cm

Figure 58.   Electron Beam Fluorescence-End View
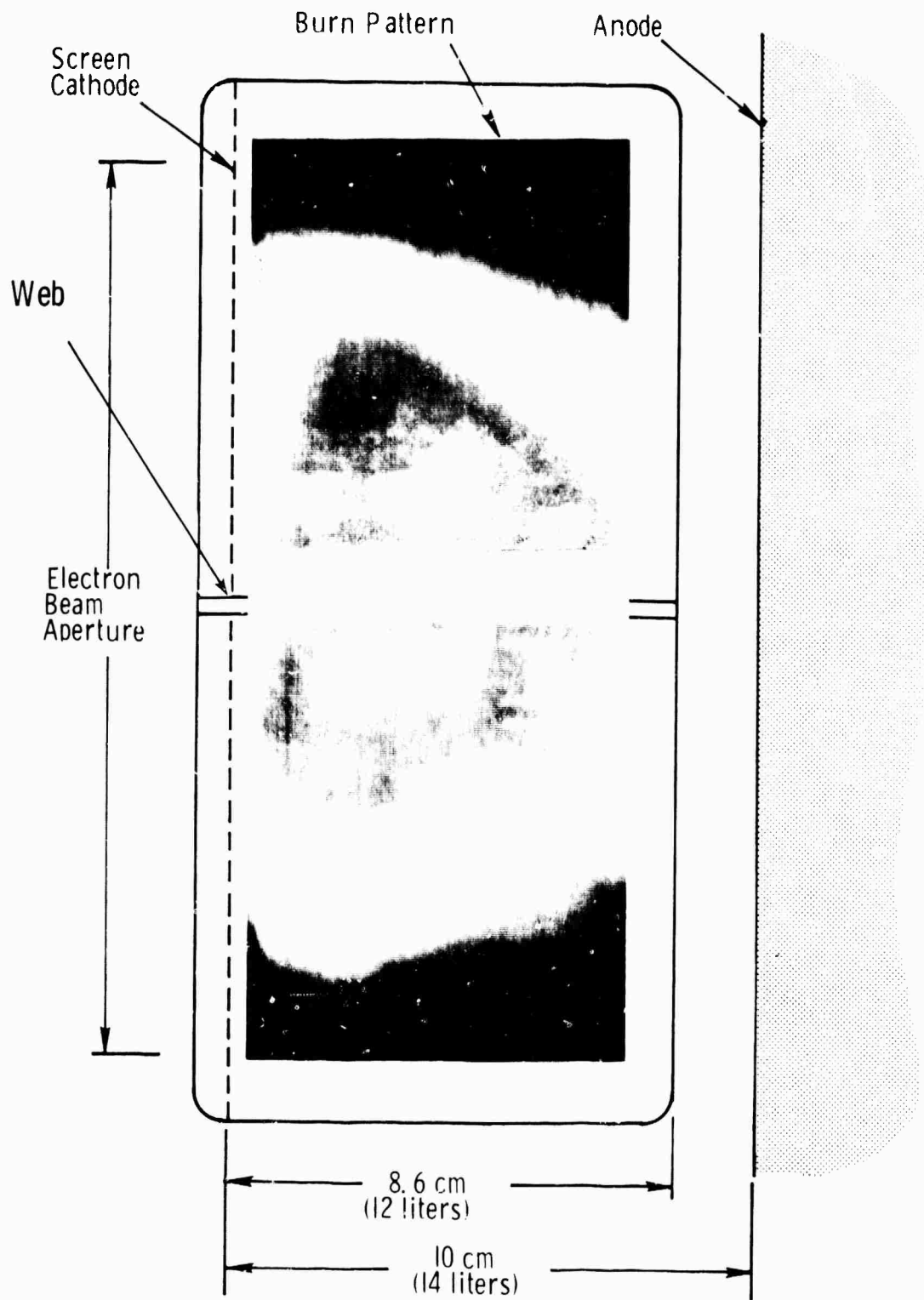
Figure 59. Laser Output Pattern

which contributes very little to total energy. The rectangular border
indicates the position of the optic holder which extends into the laser plenum
providing for an optical cavity length of 1.5 M. A support web, shown at the
center of the optic holder and burn pattern, obscures about 0.2 liters of gain
volume. The burn pattern corresponds approximately to a 10 liter gain
volume, and the 12 and 14 liter designations below their respective lineal
dimensions indicate the available extraction volume.

As mentioned in Section 2.1 wherein the foil support geometry was
detailed, major support web obscuration was appreciable. Under discharge
current avalanche conditions, the discharge was found to collapse into
multiple, fairly diffuse channels coincident with the inter-web open spaces
with little or no current drawn at the web areas themselves. This phenomenon
is shown in the photographs of Figure 60. As indicated in Figure 60a, the
camera was tilted to observe the discharge down the full extent of the anode.
Figure 60b shows the discharge collapse for applied fields just below full
breakdown values. The central image is the one of interest; the images to
either side of this are reflections from the optic extension. The discharge
anode is to the left and gun foil to the right. For much higher applied fields,
the discharge breaks down fully as shown in Figure 60c, and the most intense
luminosity is associated with the region of initially highest beam deposition.
Since no sign of discharge activity larger than these dimensions was observed
on the anode surface, it was difficult to estimate the distribution of discharge
current in the more expanded, stable regime. Most likely, discharge current
followed the electron beam deposition profile in which case it would closely
match the beam fluorescence or output burn patterns.

The areas of current concentration caused blemishes on the anode as
shown in Figure 61. The dark spots, roughly 2.5 cm wide by 6 cm long,
coincided exactly with the inter-web open areas and the luminous channels
of Figure 60.

Plenum Front View

a)

Camera

Optic

Anode

b)

c)
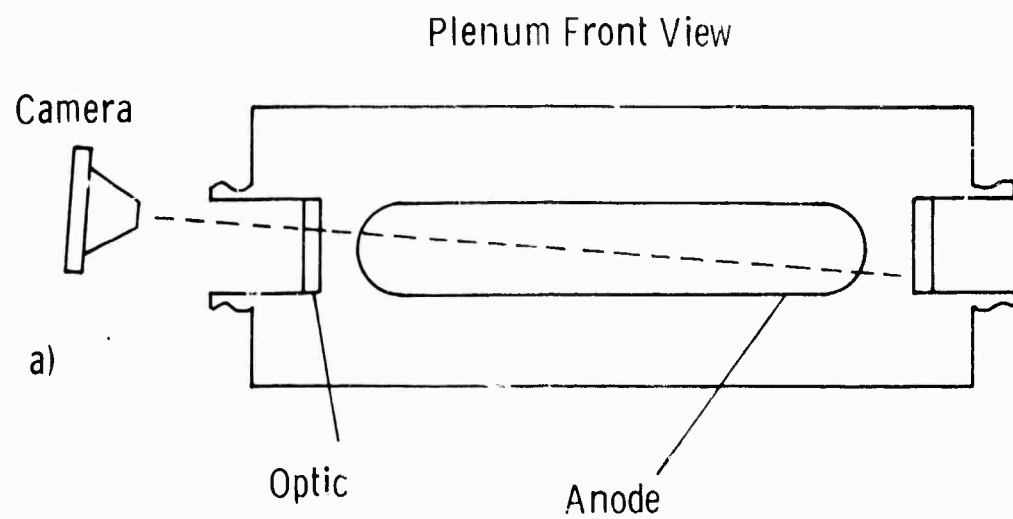
Figure 60. Discharge Collapse-End View
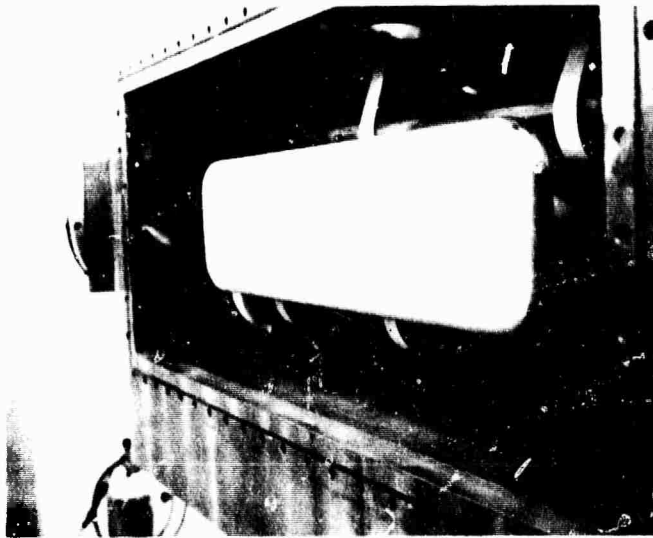
Figure 61. Arc Blemishes on Anode

The action of the discharge channels on the anode surface and the bright arcs in the photographs were a result of long term oscillatory currents, since after electron beam turnoff the discharge was found to ring for times on the order of 20 µs as shown in Figure 62. The period of interest was in the first microsecond, a small fraction of the total waveform. Therefore, the effects of discharge collapse pr ented above correlate strongly with the period after termination of the electron gun pulse when discharge collapse would be expected in any case without the stabilizing influence of the electron beam. These arc effects were not observable during the gun pulse owing to their small contribution to the temporal averaging measurements employed here. However, the long term current spatial behavior is useful since it is most likely indicative of that occurring during the gun pulse if discharge collapse occurs. It is reasonable to assume that the avalanche distribution resulting from discharge collapse during the gun pulse would carry over to later times as well. At no time was a distribution other than that outlined above observed, suggesting that the arc geometry during electron beam operation was as indicated by the long term measurements.

Figure 62 also gives an indication of the inherent circuit inductance in the case of discharge collapse. From the usual relationship relating capacitance and inductance to ringing frequency, the inductance is determined to be about 225 nH. When compared to the crowbar inductance of 175 nH it is clear that the arc channels are capable of competing favorably with the crowbar circuit for energy. Indeed, it was found that the crowbar did not alter the waveforms obtained without it.

Typical Waveforms. The discharge and laser output were characterized with the two basic circuit types reviewed previously. These consisted of a simple capacitive discharge and a pulse charged, two stage capacitive discharge. In the former case, it was found that significant energy was delivered only in the latter half of the excitation pulse, limited by discharge ing. With the

132

A–K=3 cm
C_1=1. 33 μF
F_2/Kr/Ar=2/100/2280
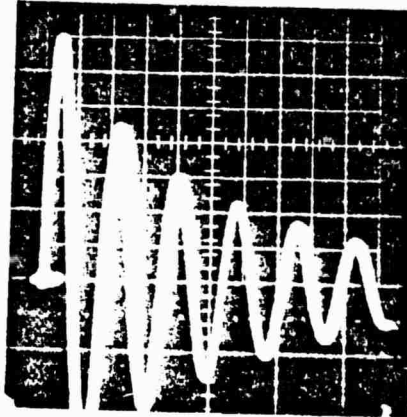
9 KA/Div
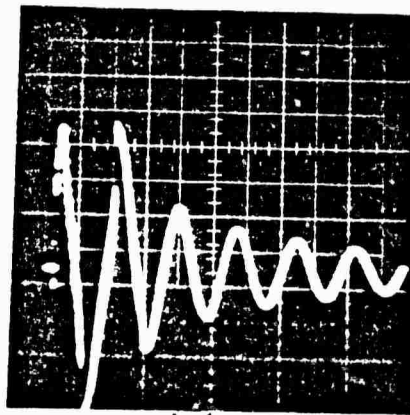
I. 0 KV/Div

2 μs

Figure 62 Long Term Discharge Voltage and Current

pulse charged discharge, it was observed that energy was delivered significantly earlier in time, but that discharge arcing also occurred earlier, with the net result that the two circuits were equivalent as far as total energy loading was concerned. By varying storage capacitance, attempts were made to reduce discharge voltage late in the excitation pulse in order to prevent arcing at these times. It was observed that total energy input did not vary significantly for capacitive storage in the range 1.33-2.33 μF. Above these values, arcing was not observed to occur sooner, but the excess stored energy, channeled into several columns, would often lead to gun foil rupture. The relevant discharge and laser output waveforms are presented in the following eight figures for both the KrF and XeF systems.

Figure 63 shows typical traces for the capacitive discharge with an anode-cathode separation of 10 cm and central beam current density of 10 A/cm^2. A nominal gas mixture of 2 Torr F_2, 100 Torr Kr and 1.7 atm Ar was used. Voltage values along the top of each column indicate initial capacitor bank voltage and are included for labeling purposes. Relative energy output is indicated along the bottom of each column. Laser output with beam only excitation is shown in the far left column and relative output in this case is 67% of the maximum obtained with discharge excitation. The upper trace displays gun voltage, which closely approximates the current waveform, and the lower trace indicates laser intensity measured with a photodiode. The second column, indicated by an initial charge voltage of 30 KV, shows discharge voltage in the fairly erratic upper trace and discharge current in the smooth, monotonically increasing lower trace. The discharge was triggered on at the same time as the electron gun; therefore, the initial discharge voltage greatly exceeds the nominal trace values since the discharge impedance is high at early times before appreciable gun current is established. The possibility that high discharge field strengths prior to gun turn on could set up incipient arc channels which would lead to arcing during the pulse was

A-K = 10 cm
C_L = 2.33 μF
F_2/Kr/Ar = 2/100/1267 Torr

Beam Only (10·A/cm²)   30 kV   40 kV   50 kV

9 KA/Div.

2.5 kV/Div.

Laser Intensity

Relative = 0.67   0.87   1.0   1.0
Output

time 200 ns/Div.
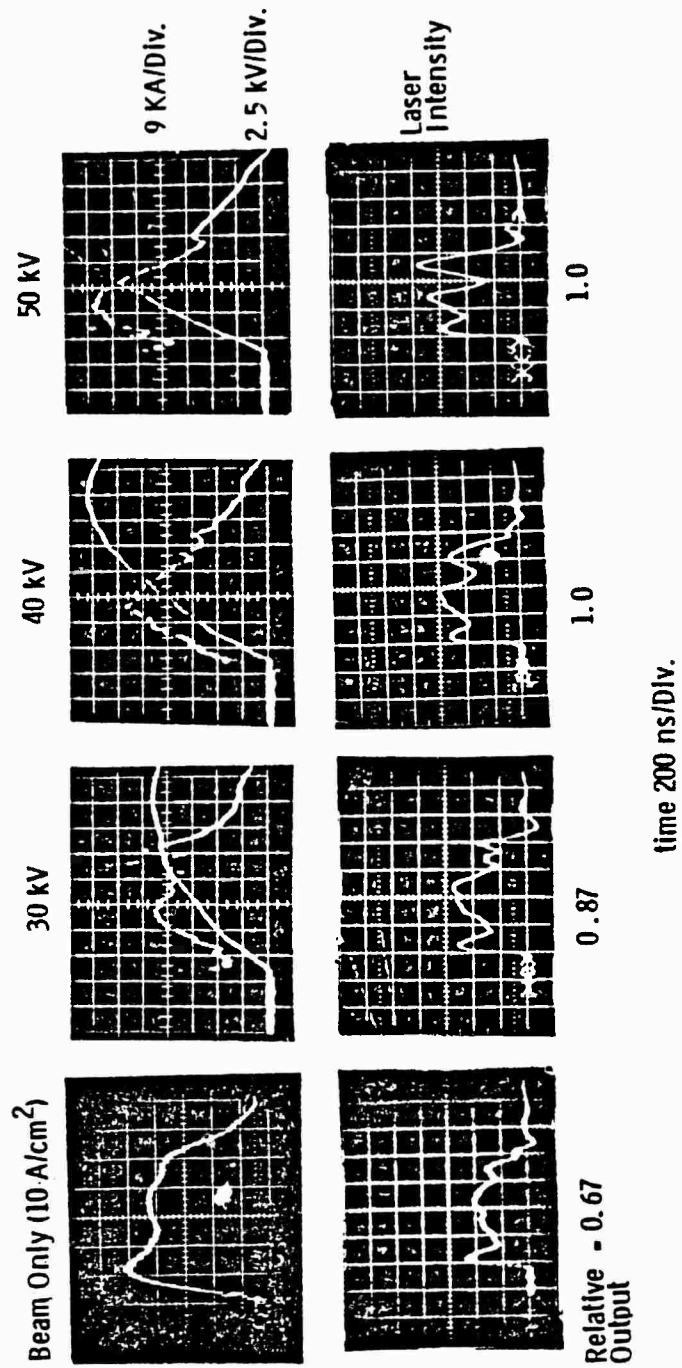
Figure 63.   Capacitive Discharge

135

tested by delaying the discharge with respect to gun turn on. Identical results were obtained for all discharge delays indicating that this possibility was not realised. After full beam current is established the discharge impedance drops and the applied discharge voltage is likewise lowered at which point discharge current begins to flow. As the rate of rise of discharge current decreases, the inductive voltage drop lessens and discharge voltage begins to rise. However, voltage begins to fall off roughly 500 ns into the pulse as the capacitor bank is depleted until finally at about 900 ns the electron gun turns off and the discharge impedance rises once more. This results in a second sharp peak in discharge voltage due to residual energy in the capacitor bank. After this point, voltage drops drastically and current continues to rise indicating the onset of arcing. As the discharge waveforms show, discharge energy is pumped in primarily late in the pulse and this is reflected in the late enhancement of laser output. These trends are apparent in the other traces for 40 and 50 KV initial charge voltages as well. At higher charge voltages, however, discharge voltage drop is experienced earlier in the pulse, whereas current continues to rise indicating that arcing occurs earlier also. The fact that the laser pulse is also terminated at earlier times supports this observation. Unfortunately, the onset of arcing cannot be more firmly established. The usual sign in higher impedance discharges of an inflection in discharge current is lacking here due to the low discharge impedance which does not change appreciably under discharge collapse. Attempts at observation of increases in discharge fluorescence with a photodiode at the time of arcing failed, since fluorescence levels were not noticeably different before and after the indicated time of discharge collapse during the pulse.

Typical traces obtained with the pulse charged, two stage discharge are shown in Figure 64; and the various parametric values were identical to the previous case. With reference to the 20 KV initial charge case, the discontinuous upper trace indicates discharge voltage and the lower, almost flat curve, indicates capacitor bank current. The initial steep rise in discharge
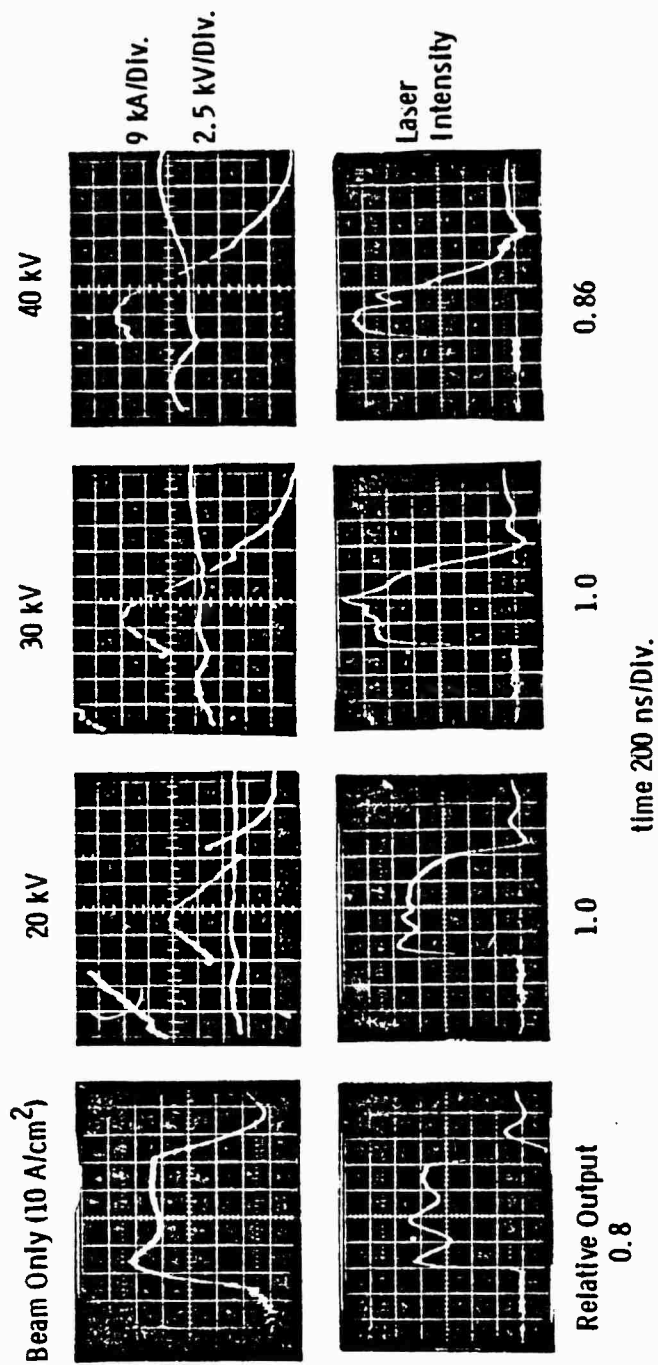
Figure 64. Pulse Charged-Two Stage Discharge

voltage results from charging of C_2, originally at ground potential. Coincident with this is a slight rise and fall in current from C_1, more easily discerned in the higher voltage traces. At 600 ns into the charge cycle, the electron beam is switched on and the discharge impedance collapses resulting in a corresponding drop in discharge voltage. After this point, the current traces do not reflect true discharge current and should be ignored. Subsequent to beam turn on, the discharge voltage behavior is identical to the previous case. It is observed that laser intensity is enhanced at earlier times compared to the simple capacitive case, but that termination of the pulse occurs earlier at the higher voltages. This effect is most likely due to the fact that arcing field strengths are approached more quickly.

As shown in Figures 63 and 64, the enhancement ratio for the simple capacitive discharge was about 1.5 whereas that for the pulse charged, two stage discharge was 1.25. The difference is within the experimental variability over a period of time for a number of such experimental runs. These previous results were obtained for a non-optimized system and are meant to represent typical discharge behavior. In both cases cited above, maximum extracted energy density was 7 J/liter at about 10% efficiency.

One of the more important experimental parameters was F_2 partial pressure, and results of variation in this quantity over the range 1.5-3.0 Torr are shown in Figures 65, 66 and 67. In this series, anode-cathode spacing was reduced to 5 cm, capacitive storage reduced to 1.33 μF, and beam current density increased to 15 A/cm^2. For the 1.5 Torr case of Figure 65, almost no enhancement was obtained, whereas at the higher partial pressures, enhancement was about 1.23. Also for increasing partial pressure, discharge impedance is observed to increase as a result of increasing F_2 attachment. Highest energy extraction was obtained for 2 Torr F_2 which was considered the nominal value, and output for the 1.5 Torr and 3 Torr cases was down by 10 and 20% respectively from this maximum.

138

A-K-5 cm, V-1.6 liter
C_I-1.33 μF
F_2/Kr/Ar-1.5/100/1267 Torr

Beam Only (15 A/cm²)   30 KV   40 KV   50 KV

18 KA/Div

2.5 KV/Div

Laser Intensity

Relative - 0.97   1.0   1.0   0.97
Output

Time   200 ns/Div
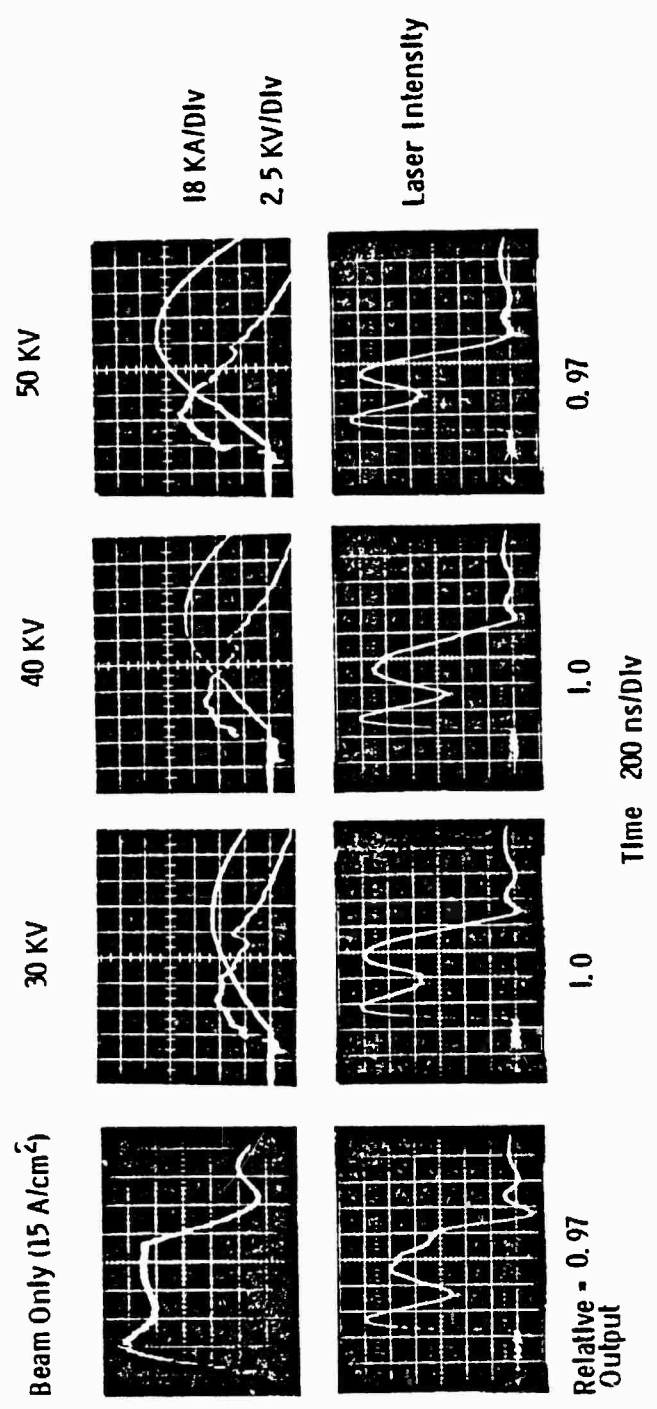
Figure 65.   Typical Waveforms-1.5 Torr F_2

139

A–K=5 cm, V=1.6 liter
C_1=1.33 μF
F_2/Kr/Ar=2.0/100/1267 Torr

18 KA/Div

2.5 KV/Div

Laser Intensity

Beam Only (15 A/cm^2)

30 KV   40 KV   50 KV

Relative 0.82   1.0   0.85   0.94
Output
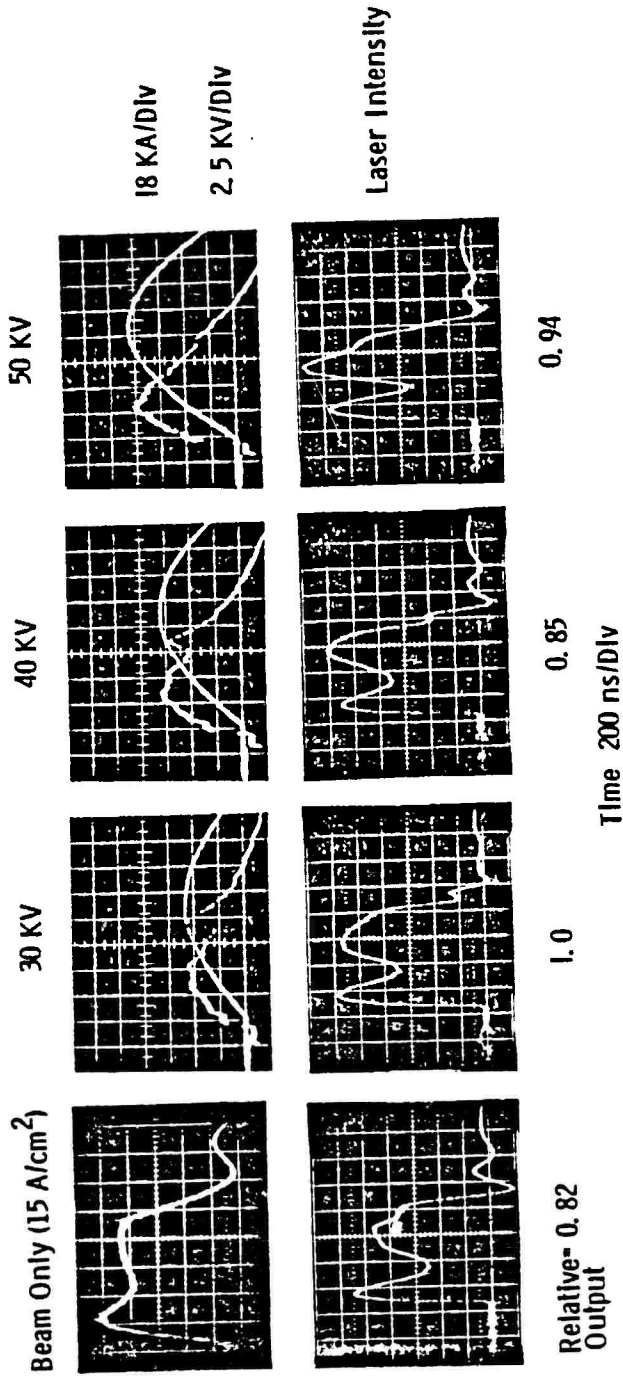
Time 200 ns/Div

Figure 66.   Typical Waveforms–2.0 Torr F_2

140

A-K=5 cm, V=1.6 liter
C_1=1.33 μF
F_2/Kr/Ar=3/100/1267 Torr

Beam Only (15 A/cm.^{2})   30 KV   40 KV
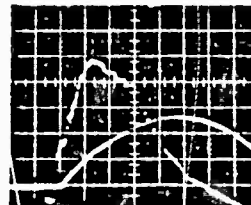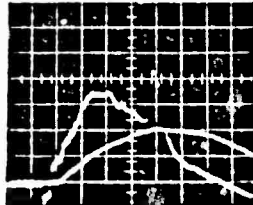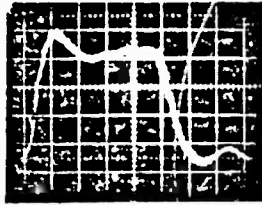
18 KA/Div

2.5 KV/Div
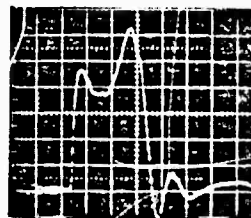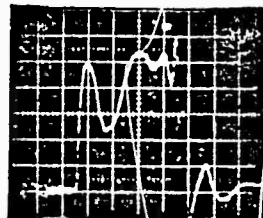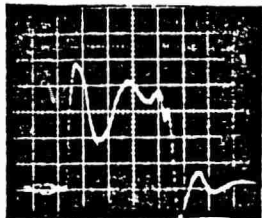
Laser Intensity

Relative = 0.81   1.0   0.87
Output

Time   200 ns/Div

Figure 67.   Typical Waveforms-3.0 Torr F_2

141

Experiments were performed for 3 atm total pressure and reduced anode-cathode spacing in order to ensure beam deposition uniformity. Typical results are shown in Figure 68. Characteristic of this regime is the spiked laser output waveform which was exhibited for a range of gas mixtures.

XeF Extraction Results. Lasing with the XeF system was attempted for gas mixtures of current interest[57] involving $NF_3/Xe/Ne$ in the ratios 1.67/5.0/1267 Torr and 2.5/7.5/2280 Torr and the results are shown in Figures 69 and 70, respectively. Electron beam current density was 15 A/cm^2 for about a 600 ns pulse. For the data of Figure 69, a capacitive discharge was used resulting in a specific extraction of 1.85 J/liter at about 1.0% efficiency and an enhancement of 2.2.

Operation at higher pressure, as indicated in Figure 70, resulted in an increase of specific extraction to 2.5 J/liter at an enhancement of 1.5. In this latter case, the pulse charged, two stage discharge was used at an anode-cathode separation of 3 cm. These results compare favorably with those of others, where maximum extraction energies of 2.8 J/liter at 1.8% efficiency have been obtained for 1 μ s pulse lengths[57].

Parametric Curves. Device parameterization for gas mixture, total pressure and discharge voltage are presented in the following series of curves. In order to guarantee reliable electron gun operation for the complete set of data, current density was reduced to 10-12 A/cm^2 for an 800 ns pulse length. Since comparison of results at high and low pressure was of interest, the discharge anode-cathode separation was reduced to 6 cm in order to provide for uniform deposition over the pressures of interest. Discharge energy was supplied by the simple capacitive circuit with C_1 = 2.33 μ F; and

---

[57] L. F. Champagne and N. W. Harris, Appl. Phys. Lett. 31, 513 (1977).

A-K=3 cm
$F_2/Kr/Ar=2/100/2280$ Torr
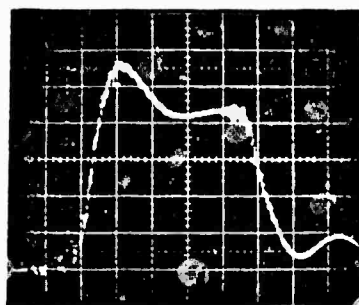
Beam Voltage
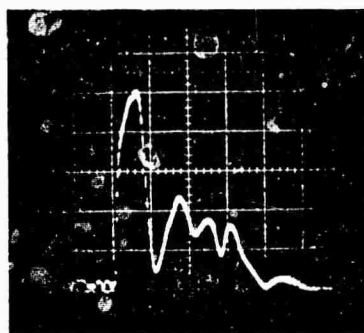
Laser Intensity

200 ns

Figure 68. Typical Waveforms at High Pressure

143

A-K=10 cm, V=2 liter
C_1=1.33 μF
NF_3/Xe/Ne=1.67/5.0/1267 Torr
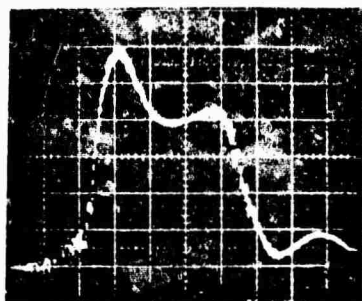
Gun Voltage
(J = 15 A/cm^2)

9 KA/Div

2 KV/Div
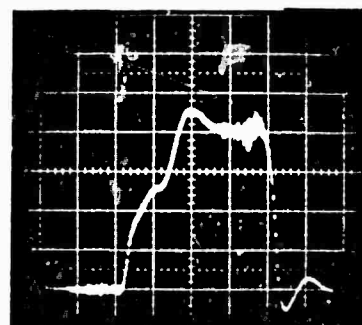
Laser Intensity
1.85 J/liter

Enhancement=2.2

200 ns

Figure 69. Typical Waveforms-XeF at Low Pressure

144

A-K=3 cm, V=1.0 liter
C_1=1.33 μF, C_2=0.7 μF
NF_3/Xe/Ne= 2.5/7.5/2280 Torr
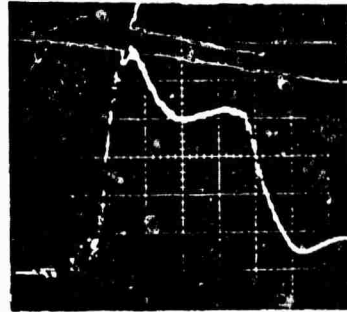
Gun Voltage
(J = 15 A/cm^2)
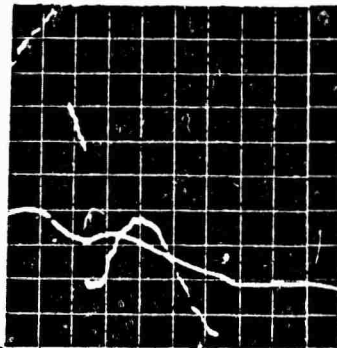
2 KV/Div

4.5 KA/Div

0 —
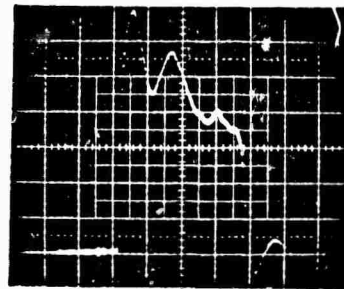
Laser Intensity
2.5 J/liter

Enhancement=1.5

| |
200 ns

Figure 70. Typical Waveforms-XeF at High Pressure

145

an optical cavity composed of 100% and 70% reflectors, separated by 1.5 M was used over the entire parametric range.

Variation of output energy with F_2 partial pressure is summarized in Figures 71 and 72 for total pressures of 1.7 and 2.3 atm., respectively. The variation in output energy was 20-30% due to shot-to-shot repeatability. The abscissa in each plot is in terms of capacitor bank charge voltage in order to provide a consistent means of comparison. The relationship of this parameter to actual discharge conditions is presented in a subsequent graph. For both sets of data, the Kr partial pressure was 100 Torr, considered to be optimum. Variation of the Kr content from 50-200 Torr for all F_2 partial pressures and the total pressures indicated, resulted in only small variations of the output energy on the order of the experimental variability.

The data of Figures 71 and 72 indicate a general trend to higher output energies with increasing charge voltage for all F_2 partial pressures. Singular inconsistencies, for example the datum at 40 KV for 1.5 Torr F_2 in Figure 71, were not representative of average values and should be ignored. It was found that the consistently highest outputs were obtained at 2 Torr F_2 (indicated by the solid lines) and a total pressure of 1.7 atm. As indicated earlier, laser output waveforms at higher pressures showed erratic, spiking behavior therefore experimentation in this regime was not extensive.

To indicate general discharge behavior for the 1.7 atm case, peak discharge voltage and current at laser output termination are shown as a function of charge voltage in Figure 73. The lower, solid lines indicate discharge voltage related to the left ordinate, and the dotted lines represent terminal current related to the right ordinate. For increasing F_2 partial pressure, discharge voltage is seen to increase whereas current decreases, indicating higher impedance as expected.
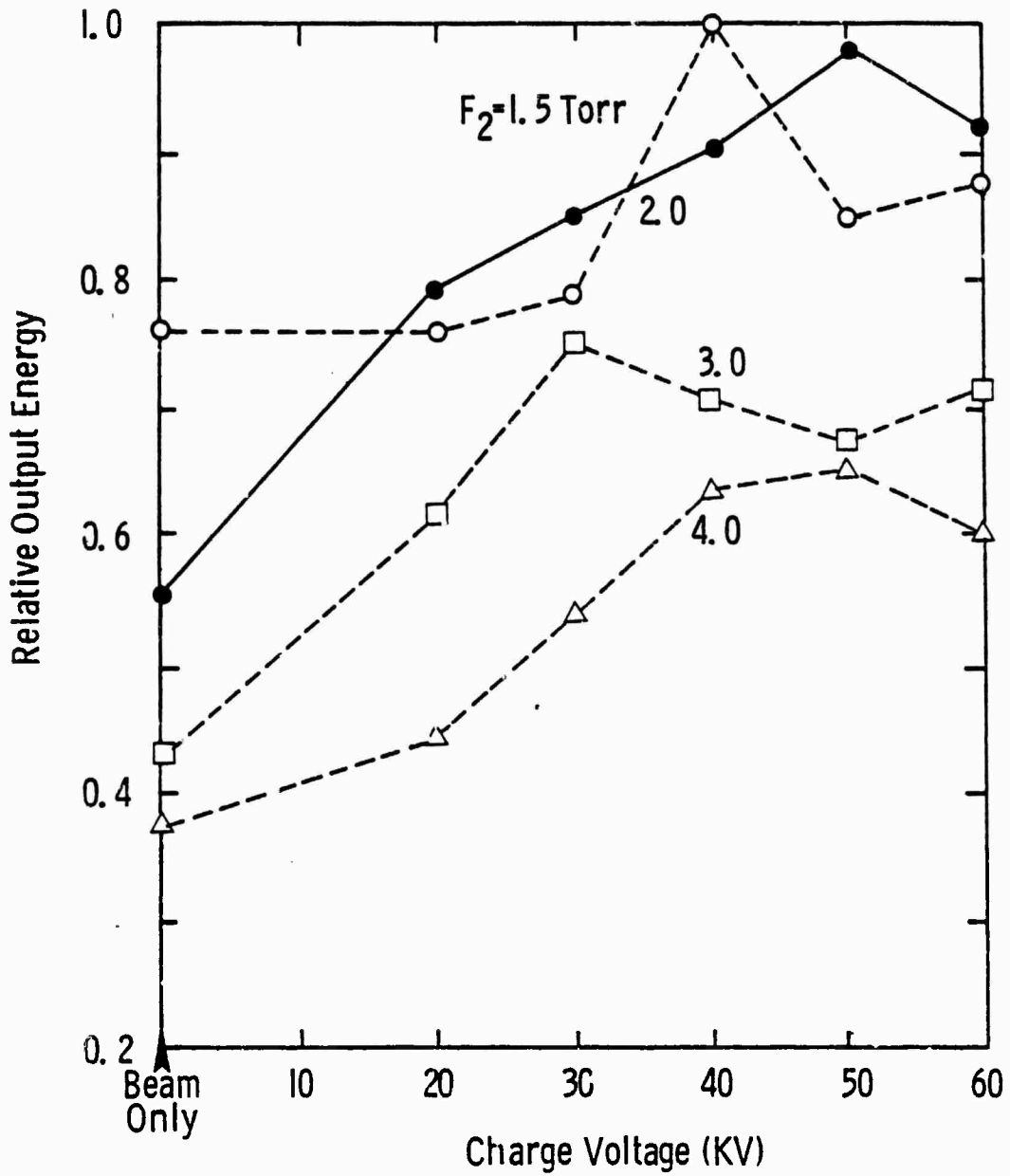
Figure 71. Relative Output Energy as Function of F_2 Partial Pressure

147
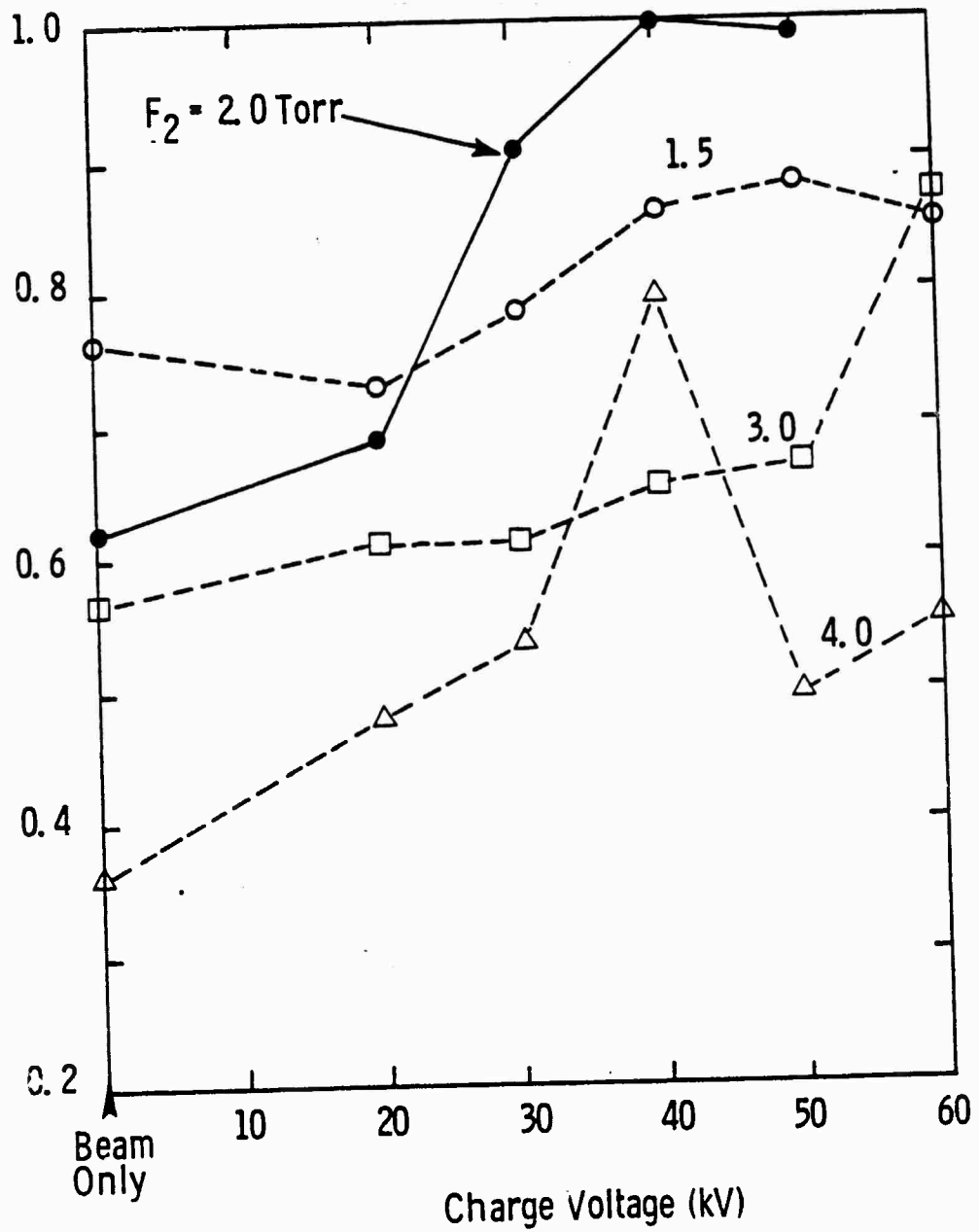
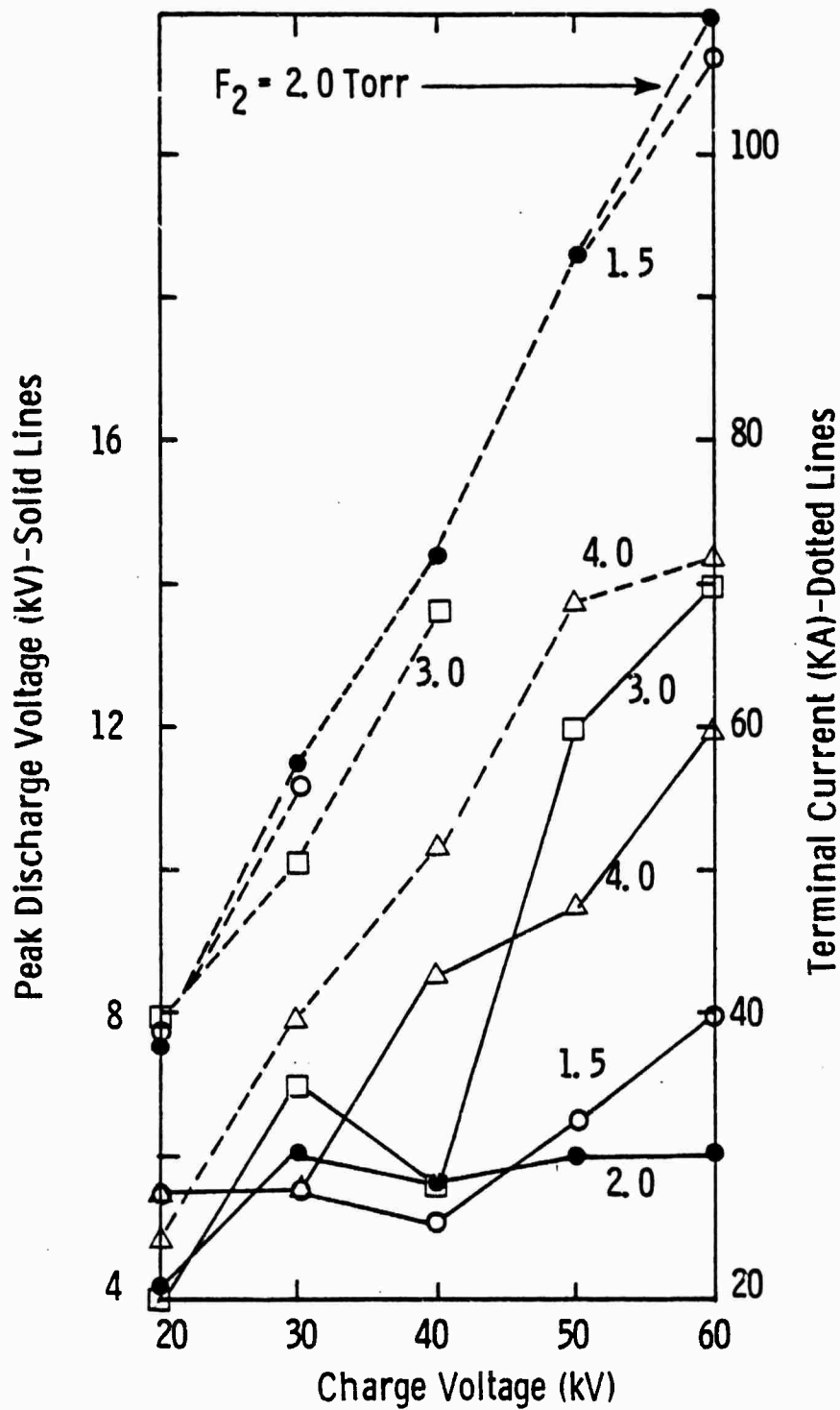Figure 72. Relative Output as Function of F_2 Partial Pressure

148

Figure 73. Peak Voltage and Terminal Current as Function of F_2 Partial Pressure

149

As previously suggested, a general criterion for premature discharge collapse during the electron gun pulse was early termination of the laser output. It was indicated that, above a certain critical field, higher voltages would lead to earlier termination. This effect is shown graphically in Figure 74. The nominal pulse length, with electron beam excitation only was 800 ns as indicated at the abscissa zero point. For all F_2 partial pressures, pulse length is not seriously degraded up to a charge voltage of 30 KV. Above this value, however, shortening occurs which becomes serious for higher F_2 partial pressures. For 2.0 Torr of F_2 this corresponds to a peak E/N of 2.2×10^{-17} V-cm^2. Of course, this is the peak experienced during the discharge and does not necessarily correspond to the undetermined arcing value which occurs later in the pulse.

Optimum Results. Laser energy extraction was optimized for both small and large anode-cathode separations. In the first case, spacings of 3-5 cm were considered in the hope of establishing the beam deposition uniformity required for high enhancements. As will be shown below, discharge stability is crucially dependent on deposition uniformity in the direction of propagation. Unfortunately, the results in this instance were limited by constraints related to electrode geometry. In the second case, an anode-cathode spacing of 10 cm was used in the interest of increased energy output.

In order to maximize laser output, it was considered important to maximize electron beam current density. In this regard, the 70% transmissive ground plane screen, adjacent to the gun pressure foil was removed. At large anode-cathode spacings, this had no effect on discharge stability, but did enhance output by roughly 60%, slightly greater than would be expected by the simple removal of a 30% obscuration. For small anode-cathode spacings, however, discharge stability was greatly impaired as a result of arcing to the raised foil edges coincident with the support webs which become prominent under gas pressure loading. In order to provide a smooth ground
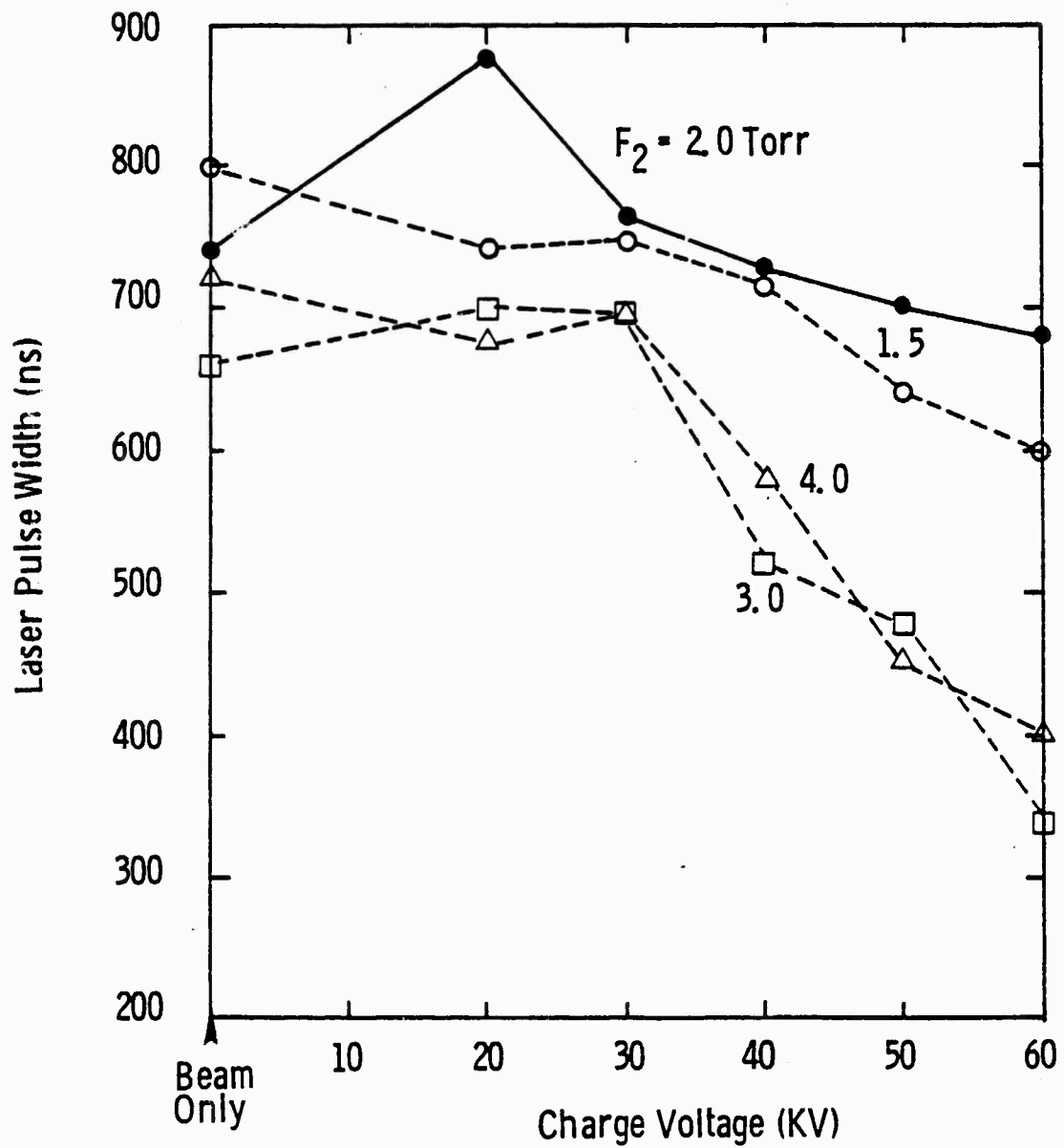
Figure 74. Laser Pulse Width as Function of F_2 Partial Pressure

plane without reintroduction of the 70% transmissive screen, a second unloaded 5×10^{-3} cm aluminum foil was placed directly over the pressure foil. Measurements with a Faraday cup indicated that current densities immediately beyond the second foil were identical to those without it. Results with this configuration, however, were not significantly different from those in the previous arrangement with the ground plane screen. Possibly increased beam scattering from the second foil was responsible for reducing the laser output below expected levels. Alternatively, attempts at maximizing enhancement were made with short pulse operation at an anode-cathode separation of 10 cm. In this instance, although discharge collapse was experienced, harder discharge pumping could be achieved over a brief initial period. Therefore, optimum results were obtained for large volume, short and long pulse excitation as outlined below.

Table 1 summarizes the results for long pulse operation with central beam current densities on the order of 15-18 A/cm^2. As suggested by previous remarks concerning deposition uniformity, maximum specific energy was deposited roughly in the central three liters. Therefore, in order to obtain an indication of maximum specific extraction, the laser output was masked off allowing for transmission of only the central three liters of gain volume. The three liter volume was calculated assuming an effective gain length of 75 cm as indicated by the longitudinal deposition profiles. These results are tabulated in the first column in Table 1. Specific extraction in this case was relatively high at 18-22 J/liter. The span indicates extraction with beam only for the lower value and beam plus discharge excitation at the maximum. Enhancement was therefore 1.2. For the full, unmasked 10 liter extraction volume where the current gradient was estimated at 10-18 A/cm^2, specific extraction was 7.5-9.0 J/liter.

152

TABLE 1. LARGE SCALE EXTRACTION RESULTS - LONG PULSE

	3 liters	10 liters
• Beam Current	$15 \rightarrow 18$ A/cm^2	$10 \rightarrow 18$ A/cm^2
• Output Energy	54-65 J	75-90 J
• Specific Output	18-22 J/ℓ	7.5-9.0 J/ℓ
• Specific Input	167-200 J/ℓ	100-120 J/ℓ
• Efficiency	11%	7.5%
• Theoretical	15 J/ℓ ($\eta = 9\%$)	Enhancement= 1.2

• Conditions

Beam Voltage: 320 kV

Pulse Length: 900 ns

Optics: R = 50%, 100%

Gas: Ar/kr/F$_2$ = 1290/100/2, 1.7 atm

Enhancement in the long pulse case was clearly limited by premature discharge collapse. Therefore, in an effort to increase enhancement, harder discharge pumping over shorter time was attempted. The relevant waveforms are shown in Figure 75 and the results are summarized in Table 2. For the nominal 400 ns pulse length, enhancement was increased to 1.8 with a specific energy output of 7.2 J/liter. As indicated in the second column of Table 2, theoretical predictions, based on the extensive code described earlier, correlate quite well.

Discharge Power Loading Analysis. As indicated above, electron beam deposition uniformity in the direction of propagation was the limiting factor in achieving high discharge enhancements. A summary of a comprehensive analysis is presented below which attempts to explain these limitations in terms of detailed system parameters[58]. In essence, maximum discharge energy loading is limited by a local stability criterion and the requirement for current continuity from anode to cathode.

The stability criterion is derived assuming that electron production and loss are a result of electron beam and metastable ionization and F_2 attachment, respectively. An upper bound on discharge energy loading is developed from a limitation on discharge E/N, which if beyond certain critical values leads to runaway metastable ionization and arcing. The criterion reflects the requirement that ionization from the electron beam must dominate that from the discharge to maintain a stable discharge for times on the order of a microsecond. Or, in more definite terms, for the parametric range of interest,

---

[58] W. H. Long, Jr. "Discharge Stability and Scaling of the KrF Laser", Presented at 30th Gaseous Electronics Conference, Palo Alto, Calif., 18-21 October 77, (To be submitted to J. Appl. Phys. (1977)).
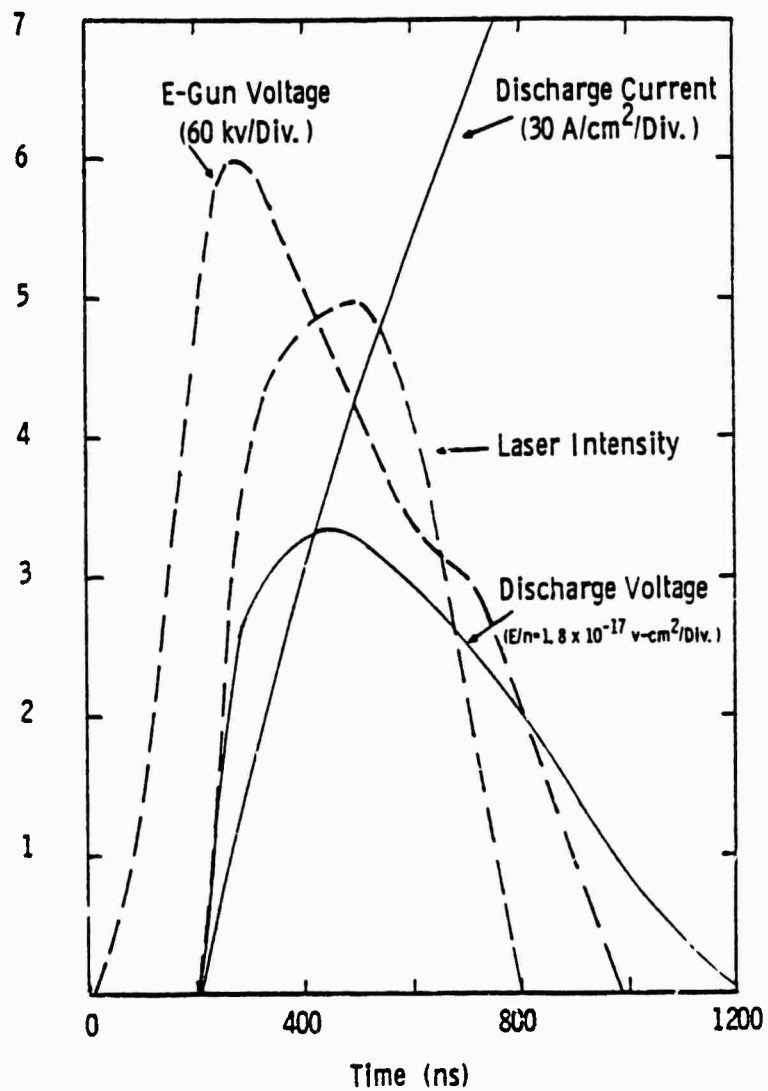
Large Scale Extraction - Short Pulse

Figure 75. Waveforms for Short Pulse Case

155

TABLE 2. LARGE SCALE EXTRACTION RESULTS - SHORT PULSE

	Experimental	Theoretical
E-Beam Only	E(In) = 83 J/ℓ	83 J/ℓ
	E(Out) = 4 J/ℓ	5.0 J/ℓ
	η = 5%	6%
E-Beam and Discharge	E(In) = 103 J/ℓ	167 J/ℓ
	E(Out) = 7.2 J/ℓ	10 J/ℓ
	η = 7%	6%
	Enhancement = 7.2/4 = 1.8	2
Conditions	E-Beam: J = 18 A/cm^2, V = 300 keV, T = 400 ns	
	Discharge: E/n = 6 x 10^{-17} V-cm^2	
	Optics: R = 50%, 100%	
	Gas: Ar/kr/F$_2$ = 1290/100/2, 1.7 atm	

$$P_d < \gamma \, P_e^{1/2}, \tag{36}$$

where, P_d and P_e are discharge and electron beam power density, respectively and the quantity γ depends on only the fluorine partial pressure (F_2) and total pressure (P) according to

$$\gamma \cong 0.23 \, (F_2)^{1.1} \, (P)^{0.2}. \tag{37}$$

where F_2 is in Torr and P in atm.

It is required that the current be continuous across the discharge. That is,

$$J_d = e \, n \, v_e = Const. \tag{38}$$

Within the range 1Td $< E/N < 10$ Td and $10^{-6} < n/N < 10^{-5}$, v_e can be approximated by

$$v_e = b(n/N)^{0.2} \, (E/N)^{0.4}. \tag{39}$$

The current density is therefore,

$$J_d = enb \, (n/N)^{0.2} \, (E/N)^{0.4} \tag{40}$$

The requirement (38) therefore dictates that E/N vary as $(n/N)^{-3}$; and since P_d is directly proportional to E/N,

$$P_d \propto (n/N)^{-3}. \tag{41}$$

The principal loss of electrons is by F_2 attachment. If metostable ionization is neglected, the electron density can be expressed as,

157

$$n = P_e / \beta \, F_2 W_i \tag{42}$$

where β is the attachment rate and W_i is the energy required to form an electron-ion pair.

Combining (41) and (42),

$$P_d \propto P_e^{-3} \tag{43}$$

For the purposes of calculation, it is assumed that the electron energy deposition fall-off is linear from the foil to some distance, d, from the foil. If r is the ratio of power density at d to that at the foil, then

$$P_e(x) = P_{eo} \, (1 + (r-1) \, x/d)$$

Therefore, from (43),

$$P_d(x) = c \, (1 + (r-1) \, x/d)^{-3} \tag{44}$$

By invoking the stability criterion (36) and choosing the constant c to satisfy this at the point d, which guarantees it for $x < d$, the average discharge power loading can be calculated by integrating over $0 \leq x \leq d$. Additionally, if a discharge circuit is chosen which approximated that used experimentally, then the resulting power loading must be divided by 2, due to the approximately sinusoidal waveform.

Finally,

$$\overline{P}_e = P_{eo} \, (1+r)/2 \tag{45}$$

and

$$\overline{P}_d = \gamma \, P_{eo}^{1/2} r^{3/2} \, (1+r)/2 \tag{46}$$

The enhancement, ϵ, defined by

$$\epsilon = \frac{\overline{P}_d + \overline{P}_e}{\overline{P}_e}$$

is therefore given by,

$$\epsilon = 1 + \gamma r^{3/2}/P_{eo}^{1/2} . \tag{47}$$

This relationship is graphed in Figure 76 for a beam power density of 0.4 MW/cm^3, corresponding to a current density of 15 A/cm^2, and a nominal mixture of F_2/Kr/Ar = 2/100/1267 Torr. For the range of enhancements obtained experimentally, (1.2-1.4), the indicated value of r is about 1/3 and this is well within the values of beam deposition determined experimentally as outlined in Section 2. Also, by (47), enhancement decreases as beam current is raised, and this was observed experimentally. In this case, the theoretical maximum enhancement is only 1.9. Of course, for fixed r, enhancement can be increased by increasing F_2 partial pressure and total pressure or by reducing electron beam power density. However, these procedures are limited due to kinetic processes. As beam current density is reduced, total power drops and absorption begins to become important. For an increase in F_2, quenching of KrF^* and absorption by F_2 increases; and an increase in total pressure accentuates beam nonuniformity and leads to the formation of timers which provide additional energy loss channels. Determination of the optimum set of parameters is very complex and cannot be obtained simply from the above formulation.

4.2 <u>Typical Theoretical Correlation.</u> The details of an extensive theoretical kinetic model for description of the physics of an electrically excited laser, as well as its numerical implementation by a comprehensive

159

$$P_{eo} = 0.4 \text{ MW/cm}^3$$
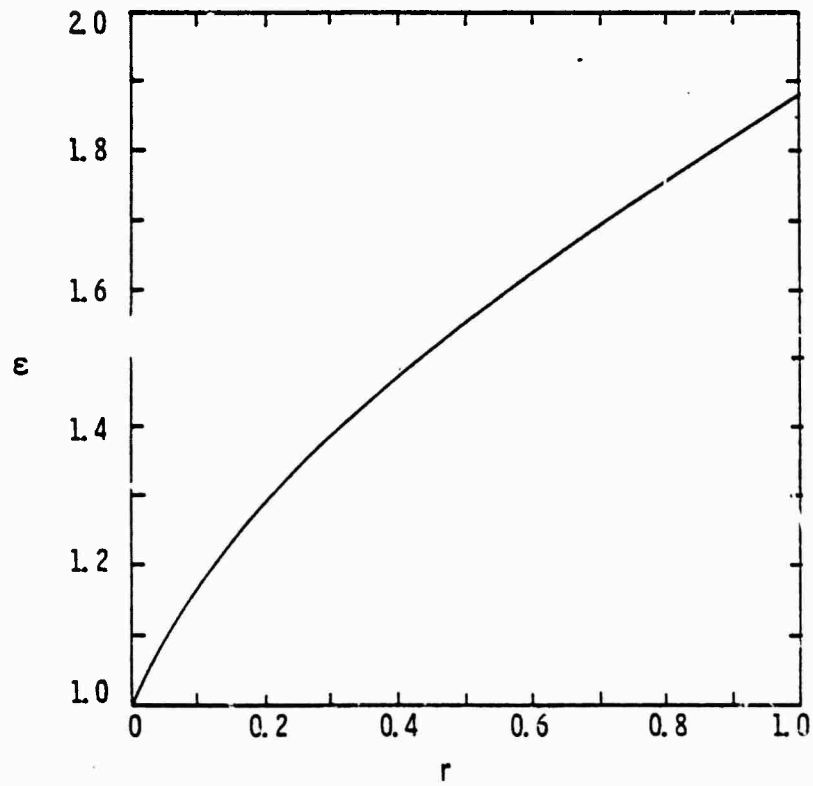$$F_2/Kr/Ar = 2/100/1207 \text{ Torr}$$

Figure 76.   Enhancement versus Beam Gradient

and general computer code, have been described in Section 3. In Section 3.4, results of a typical analysis were presented in order to illustrate the flexibility and generality of this code; in addition, the figures presented in that Section have been selected to summarize the physics of the molecular kinetic reaction scheme currently assumed for the KrF laser system, as well as to correspond to parameters for which a comparison with experimental data from the scale-up device can be made. Correlations of the theory with experimental data have been made for a variety of conditions, and reasonably good agreement has been obtained.

The nominal operating parameters for the calculations presented in Section 3.4 correspond to conditions typical of the scale-up device described earlier. This device consists of an electron-beam-stabilized, low inductance, capacitive discharge, defined by a 20 x 100 cm^2 anode, separated by (its maximum value) of 10 cm from a grounded cathode screen through which a ($\sim$ 320 keV) e^--beam is passed. The maximum gain volume is nominally 20 liter, with optical extraction along the major axis. However, for the present experiment, the optical resonator used a 6 cm diameter (R = 70%, not optimized) extraction area located just adjacent to the screen cathode with L_c (cavity spacing) = 130 cm, and γ (the intracavity loss/pass) = 0. The e^--beam-excited gain length was estimated (by cinemoid) to be $L_g \sim$ 75 cm, giving an extraction volume $\sim$ 2 liter. The laser plenum can be operated up to 10 atm, although the typical conditions for the present results consisted of $Ar/Kr/F_2$ = 1190/100/1.5 at a total pressure of 1.7 atm. Electrical pumping was provided by direct e^--beam excition, or enhanced by an electrical discharge with energy supplied by a 1.33 μF capacitor bank, initially charged to 40 kV. Measured circuit inductance was 200 nH. Electron beam current density was $\sim$ 10-12 A/cm^2 for a pulse duration of $\lesssim$ 1.0 μs. Available circuit diagnostics included discharge voltage, measured directly at the anode, and total discharge current, measured at the capacitor bank ground connection. Optical output was diagnosed with a photodiode for temporal behavior, and a

calorimeter for measurement of total output energy. Predictions of the analytical model have been compared with experimental results from this device. Figure 77a shows an oscilloscope trace of the e^--beam voltage V_b, and Figure 77b displays the temporal output power obtained with e^--beam excitation only. Figure 78a shows traces for the discharge voltage and current, and Figure 78b the laser output enhanced with discharge pumping. These data are to be compared with theoretical predictions shown in Figure 79. The e^--beam current density $J_b(t)$, which approximately follows a $V_b^{3/2}$ law, had a maximum value of ~ 12 A/cm^2, and is shown in Figure 79.

Experimentally, the maximum extracted output was ~ 8 J with e^--beam excitation only, and 14 J with an electric discharge, corresponding to specific outputs of 4.0 J/liter and 7.0 J/liter, respectively. Beam uniformity was estimated to be approximately constant, with less than 15% reduction in intensity at the edges of the optical aperture. These values are to be compared with predicted values (integration of power in Figure 79) of 4.7 and 7.0 J/liter, at 5.6% and 5.5% efficiency, respectively.

Note the steep leading edge and the sharp decay at early times on the optical extraction. The origin of this effect is the theoretically predicted strong overshoot of the net gain coefficient (about a factor of 5) over the threshold loss, resulting in superfluorescent extraction for about 100 ns (cavity photon lifetime is $t_c \sim 25$ ns), after which the gain relaxes to threshold. Later in the pulse, for e^--beam excitation only, the output approximately follows the temporal e^--beam current density, since the dominant mechanism is the formation of KrF* by F$^-$ ion recombination. (The F$^-$ population density follows the secondary electron density n_e, whose source term is e^--beam ionization, $J_b(t)\sigma_{eff} N/e$). For the case of electric discharge, the rate of change of sustainer voltage and current is limited by the inductance, and the maximum voltage (~ 12.5 kV) is limited by the low circuit impedance ($\sim 0.2 \, \Omega$). Thus, the effects of enhanced pumping do not

162

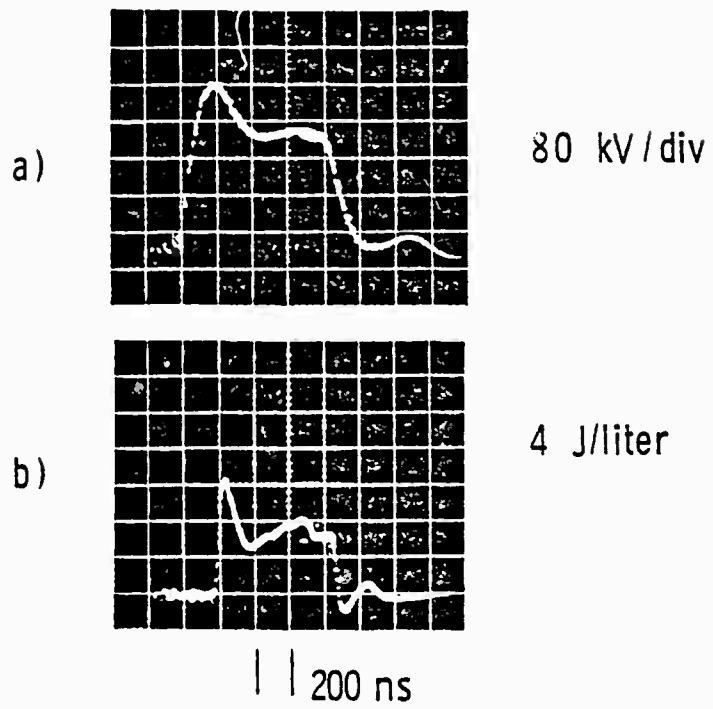a)   80 kV / div

b)   4 J/liter

| | 200 ns

Figure 77.   Electron Beam Voltage and Optical Output Power

a)   2.5 kV / div

18 kA / div
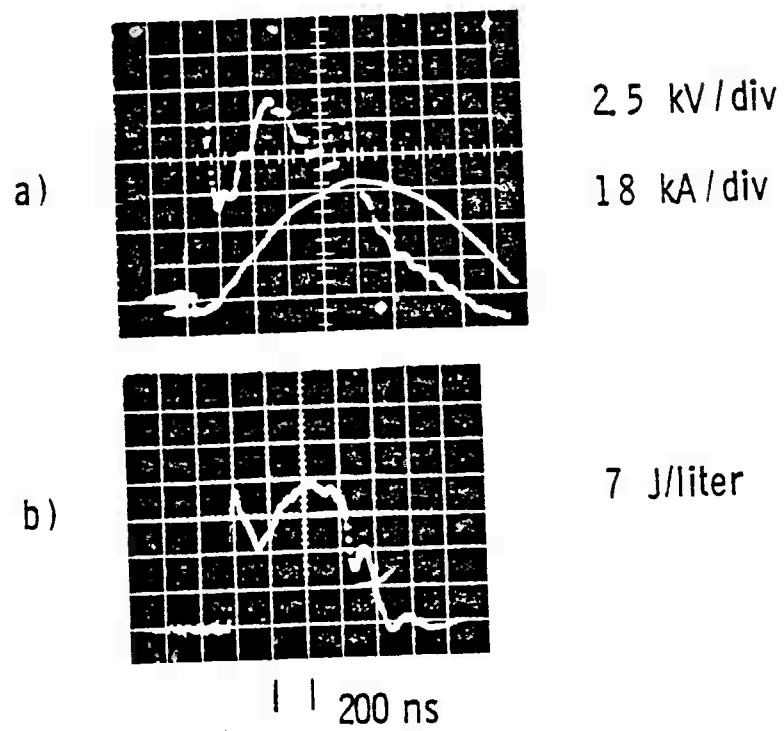
b)   7 J/liter

200 ns

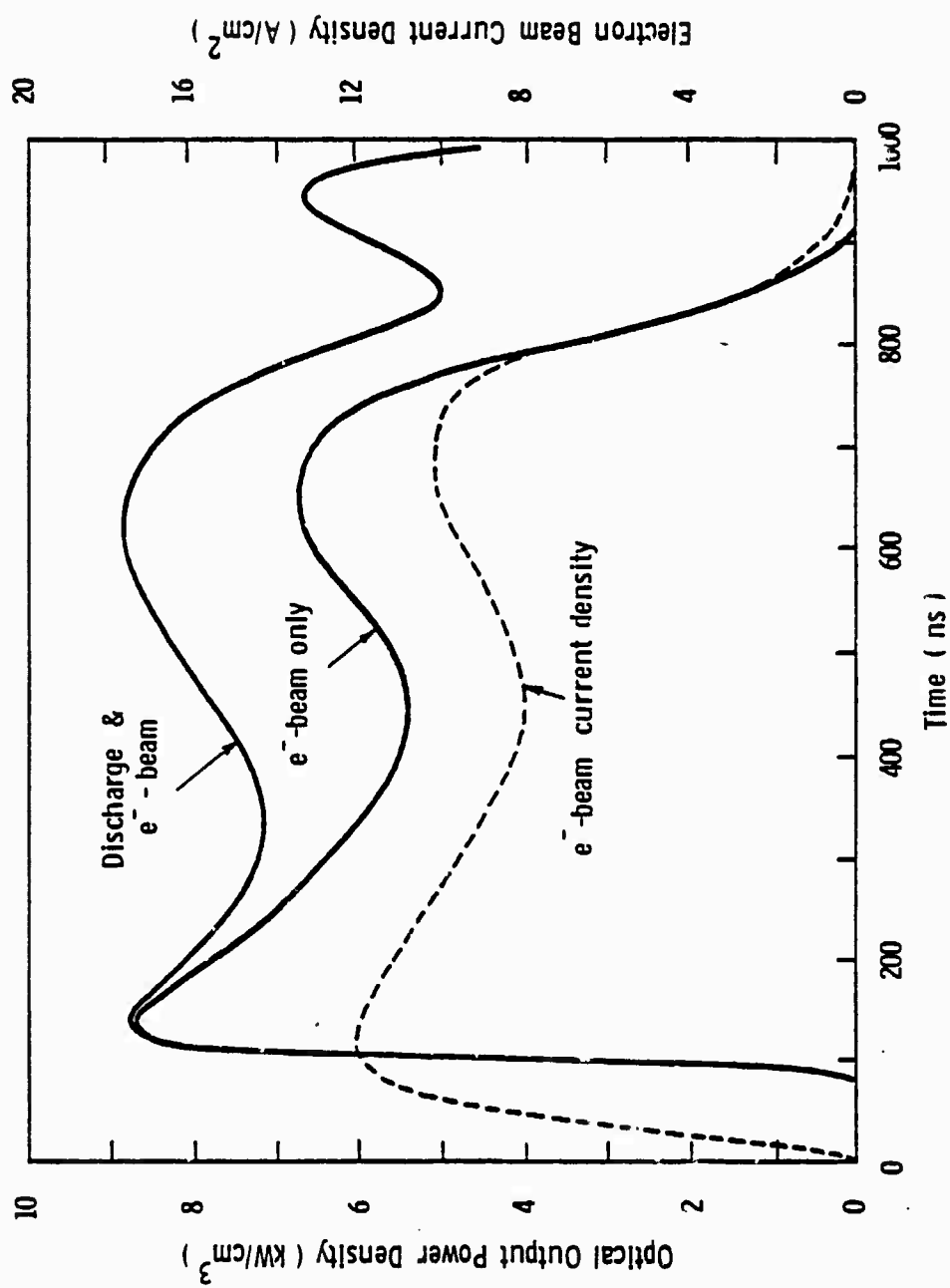Figure 78.   Discharge Characteristics and Optical Output Power

Figure 79. Theoretically Predicted Optical Output Power Density With/Without Discharge

occur until much later in the pulse, after ~ 500 ns. Note the appearance in Figure 78a of a sharp initial voltage spike across the discharge, caused by the initially high impedance. Note also the increase in discharge voltage at the end of the pulse, after the e^--beam current falls off. This is also reflected in Figure 78b and 79 in the small bump on the final edge of the optical extraction for the discharge case (somewhat overpredicted by the analysis). This perturbation occurs because the discharge impedance rises faster than the current decays.

The good agreement which has been obtained in comparisons of predictions of the present model with data from this and other KrF laser devices suggests that the KrF kinetics are reasonably well understood. Results of the present analysis indicate that much higher optical extraction should be possible with the nominal operating parameters of the present device. The extrapolation to higher power will be discussed in the following section.

4.3 Scaling Considerations. Predictions of the present laser kinetic model indicate that high optical extraction ($\gtrsim 35$ J/liter) at ~ 6.5% efficiency should be possible with the nominal operating parameters of the present device. To achieve this extraction, enhancement by means of an electric discharge is required. At present, the optimistic performance calculations to be discussed here have not been realized experimentally; and the reason for this can be explained in terms of discharge nonuniformity and stability. If uniform e^--beam energy deposition and uniform electrical excitation over large volumes can be achieved, the realization of efficient high energy KrF laser performance should be possible.

Consider the following experimental parameters (optimistic, but not necessarily optimized) which should be attainable from the present scale-up

· 166

device. Assume an Ar/Kr/F_2 = 89.8/10.0/0.2 mixture at 3.0 atm, pumped for 1.0 μs with an external RLC circuit with L = 200 nH and C = 4.0 μF (initially charged to 100 kV) driving a discharge of area 2000 cm^2 and A-K separation of 10 cm, sustained by an external e^--beam of (constant) current density 15 A/cm^2. Let the optical resonator be formed by (100, 30)% reflecting mirrors with a gain length L_g = 100 cm. Results of the analysis are shown in Figure 80, where optical output power density and electrical input power densities from the e-beam and discharge are shown plotted as a function of time. For a 1.0 μs pulse, integration of the curves gives an output energy extraction of $\gtrsim$ 35 J/liter at ~ 6.5% efficiency.

4.4 Conclusions. Results of the present investigation have indicated that high optical energy extraction at high efficiencies is possible from the KrF system. As a result of the present program, an extremely flexible and versatile experimental device, as well as a comprehensive theoretical analysis with a broad range of applicability were developed for the investigation of electrically excited laser systems. Although certain experimental limitations prevented the realization of initial program goals for the KrF laser system, significant results were achieved and understanding of fundamental physical mechanisms was obtained.
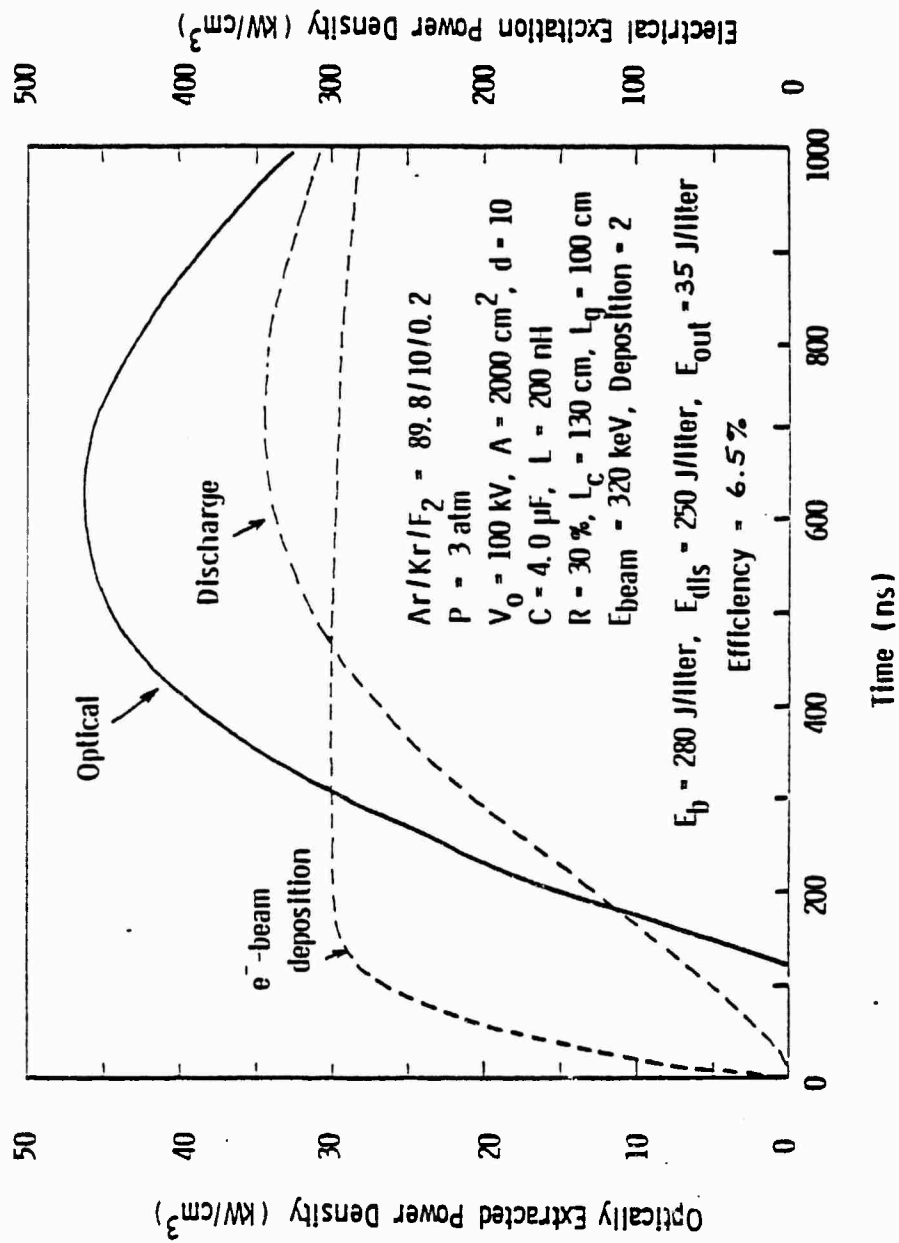
Figure 80. Optical and Electrical Power Density